

Measuring Mechanical Properties of the Tectorial Membrane with a Magnetizable Bead

by

Charles Cameron Abnet

Submitted to the Department of
Mechanical Engineering

in partial fulfillment of the requirements for the degree of

Doctor of Philosophy

at the

MASSACHUSETTS INSTITUTE OF TECHNOLOGY

February 1998

© Massachusetts Institute of Technology 1998. All rights reserved.

Author

Department of Mechanical Engineering
November 4, 1997

Certified by

Dennis M. Freeman
W.M. Keck Career Development
Assistant Professor in Biomedical Engineering
Thesis Supervisor

Accepted by

Ain Sonin
Chairman, Departmental Committee on Graduate Students

APR 27 1998

Measuring Mechanical Properties of the Tectorial Membrane with a Magnetizable Bead

by

Charles Cameron Abnet

Submitted to the Department of Mechanical Engineering
on November 4, 1997, in partial fulfillment of the requirements for the degree of
Doctor of Philosophy

Abstract

An instrument for applying time-varying forces to microscopic tissue samples was developed and used to measure mechanical properties of the isolated mouse tectorial membrane (TM). The TM is a gelatinous acellular tissue that is believed to play an important role in producing the stimulus for mechanically sensitive hair cells in the inner ear of vertebrates. However, the mechanical properties of the TM are unknown.

Forces are applied to the TM with a magnetizable, silicon-iron bead (typically 10 micrometers in radius) attached to the surface of the tissue. A computer-controlled current source powers electromagnets which generate a time-varying magnetic field. The field produces a force on the bead, which exerts a tangential force on the surface of the TM. Resulting motions of the bead and adjacent tissue are measured using a video microscopy system with a resolution of 20 nanometers.

Measurements have been obtained for TMs from 12 mice. The magnitude of the magnetic bead's displacement at 10 Hz was nearly proportional to the magnitude of the applied force for forces from 0.0001 to 0.1 micronewton. However, displacements were smaller for forces applied in the direction of maximum sensitivity of hair cells (radial direction) than for forces in the orthogonal in-plane direction (longitudinal direction). The magnitude of the bead displacement decreased as the frequency of the applied force increased from 10 to 100 Hz — at 10 dB/decade for longitudinal forces and 8 dB/decade for radial forces. The angle of the displacement lagged that of the stimulus current by approximately 45 degrees across frequencies. Displacement of the adjacent tissue decreased as the distance from the magnetic bead increased, typically decreasing by $1/e$ over distances on the order of 12 micrometers.

These results suggest that mechanical properties of the TM are anisotropic: stiffness in the radial direction is greater than stiffness in the longitudinal direction. This mechanical anisotropy correlates with anatomical anisotropies, especially the radially oriented micro-structure of the TM.

Thesis Supervisor: Dennis M. Freeman
Title: W.M. Keck Career Development
Assistant Professor in Biomedical Engineering

Acknowledgments

Thanks to my wife Holly and my family.

Thanks to my friends, Sean, Anton, Quentin, A.J., Zoher.

Thanks to my committee, Prof. Grodzinsky, Prof. Hunter, and Prof. Weiss. I appreciate the helpful comments.

Thanks to my advisor and friend Denny.

Contents

1	Introduction	11
1.1	Cochlear anatomy	11
1.2	Cochlear function	13
1.3	The tectorial membrane	14
1.3.1	Cochlear mechanical models and TM mechanical properties . .	14
1.3.2	Biochemical composition and molecular structure	16
1.3.3	Previous measurements of mechanical properties of the TM . .	18
2	Magnetic Bead Method	21
2.1	Background	21
2.2	Producing a magnetic force: Theory	23
2.3	Producing a magnetic force: Ring magnets	26
2.3.1	Magnetic and material properties of core	26
2.3.2	Geometry of core	29
2.3.3	Karlquist model	29
2.3.4	Measuring the relation between gap width and force	31
2.4	Producing a magnetic force: The magnetic field	34
2.5	Producing a magnetic force: Magnetizable beads	38
2.5.1	Bead material	39
2.5.2	Bead size	40
2.6	Measuring Motion: Computer microvision	40
2.6.1	Image acquisition	41
2.6.2	Motion analysis	42

2.7	Implementing the magnetic bead method	43
3	Calibration and Performance of Magnetic Bead Method	49
3.1	Magnetic bead method: Range of forces	49
3.1.1	Force calibration using Stokes' Law	50
3.1.2	Force calibration using a micro-fabricated cantilever	54
3.1.3	General calibration relation	61
3.2	Magnetic bead method: Range of measurable motions	65
3.3	Conclusions	68
4	Preparation of the Tectorial Membrane	69
4.1	Isolating the TM	69
4.2	Preparing and placing magnetizable bead	70
4.3	TM deformation measurements	71
5	Response of the Isolated Mouse Tectorial Membrane to Applied Forces	75
5.1	Tectorial membranes	75
5.2	Amplitude dependence of bead displacements	77
5.2.1	Linearity	77
5.2.2	Point stiffness	79
5.3	Frequency dependence	80
5.4	Longitudinal and radial stiffness	81
5.5	TM deformations	82
5.5.1	Relation between tissue motion and marker bead motion	82
5.5.2	Spatial extent of deformation: Space constant	83
5.5.3	Propagation of deformations	85
6	A Discussion of the Magnetic Bead Method and TM Measurements	101
6.1	Magnetic bead method	101
6.1.1	Effect of bead size	101
6.1.2	Point stiffness	103

6.1.3	Conclusions	106
6.2	Isolated TM preparation	106
6.3	Application of the magnetic bead method to the isolated TM	107
6.3.1	Variation among TM preparations	107
6.3.2	Influence of the surrounding fluid	107
6.3.3	Frequency dependent displacements	110
6.3.4	Anisotropy	110
6.4	Summary	111
A	Amplitude dependence for 12 TM experiments	113
B	Frequency dependence for 6 TM experiments	119

Chapter 1

Introduction

Sensory hair cells in the inner ear of humans are remarkable mechanical transducers which, at the threshold of hearing, are capable of sensing motions on the order of picometers, roughly the diameter of a hydrogen atom, at frequencies from 10 Hz to 20 kHz. The hair cells however, do not work in isolation, accessory structures play a critical role in producing the mechanical stimuli.

The tectorial membrane is a structure in the inner ear which is thought to play an important role in hearing. However, measuring its mechanical properties has been challenging. The membrane is microscopic, transparent, and delicate. This paper describes a new method to measure mechanical properties of the tectorial membrane.

1.1 Cochlear anatomy

Embedded in the skull in a boney casing, the cochlea is a spiral shaped, fluid filled duct. The cochlea transforms acoustic stimuli to nerve impulses which the brain perceives as sound. The illustration in Figure 1-1 shows a cross-section of the cochlear duct and highlights major structures. The cochlea is divided into three scali or chambers. Reissner's membrane separates the scala vestibuli and the scala media, while the basilar membrane and organ of Corti separates the scala media and the scala tympani. The fluid is an important means of transmitting acoustic signals and determines the ionic environment for the tissues. The scala vestibuli and scala

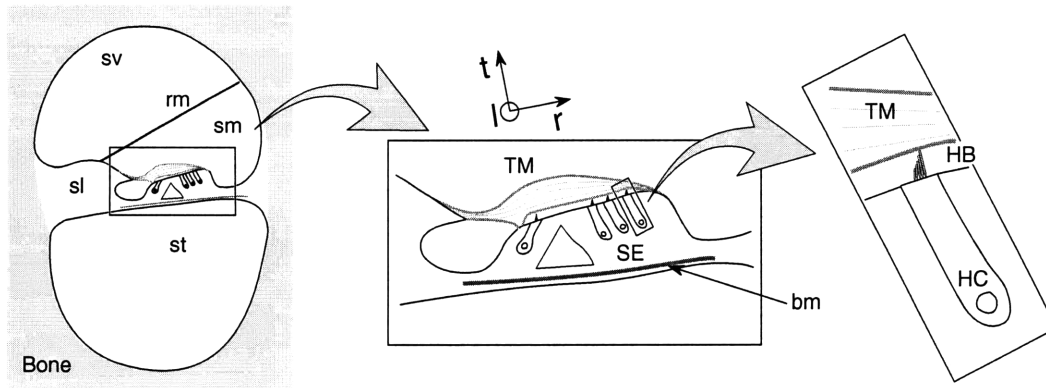


Figure 1-1: Schematic representation of mammalian cochlear anatomy. A cross-section of the mammalian cochlear duct (left panel) shows Reissner's membrane (rm), the three chambers, scala vestibuli (sv), scala media (sm), and scala tympani (st) and the spiral limbus (sl). The sensory receptor organ (center panel) is positioned on the basilar membrane (bm) and spans the duct in the radial direction (r), separating the scala media and scala tympani. The hair bundles (HB) of the outer hair cells (HC) (right panel) are attached at their bases to the sensory epithelium (SE) and at the top to the overlying tectorial membrane (TM). The structures shown in the cross-section extend along the entire length of the cochlea in the longitudinal direction (l). The transverse direction (t) is nearly vertical in the illustration.

tympani are filled with perilymph, a high sodium saline, while the scala media is filled with endolymph, a high potassium saline. Attached to the basilar membrane, is the organ of Corti which is where the sensory receptor cells or hair cells are located. Positioned above the hair cells is the tectorial membrane (TM). Reissner's membrane, the basilar membrane, the organ of Corti and the TM extend longitudinally along the entire length of the cochlea, from the cochlear base to the apex.

Each hair cell has a hair bundle made of several dozen stereocilia which protrude from the sensory epithelium into the surrounding fluid and the bottom surface of the TM. A mechanical connection exists between the TM and hair bundles of the outer hair cells (dallos, 1996; Kimura, 1966; Lim, 1972; Lim, 1980). The location of the TM and the evidence of mechanical interaction with hair bundles has important implications for cochlear function.

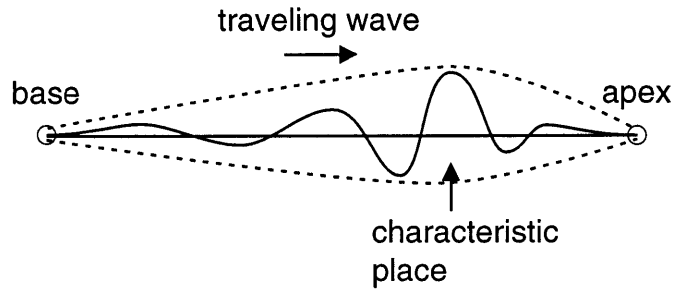


Figure 1-2: A traveling wave for a pure tone. The basilar membrane is represented, at rest, as a thin, straight, solid line. A traveling wave of transverse displacements of the basilar membrane is represented by the curved solid line. The dotted lines mark the envelope of the propagating wave. The wave is generated by fluid pressures across the membrane and travels from base to apex. Each frequency has a characteristic place along the basilar membrane where the traveling wave stalls and the amplitude of transverse displacements reaches a maximum. The amplitude of the transverse displacements is greatly exaggerated in the illustration.

1.2 Cochlear function

Sounds generate motions of the tympanic membrane which are transformed by the middle ear bones into a piston like motion of the stapes. The footplate of the stapes acts like a plunger, modulating the fluid pressure in the cochlea. Differences in fluid pressure between the scala vestibuli and scala tympani produce transverse motions of the basilar membrane. Bekesy (1953) observed that a pressure difference across the basilar membrane and organ of Corti set in motion a traveling wave which moved from the base of the cochlear spiral to the apex. The idea is illustrated in Figure 1-2. For a pure tone, a wave proceeds until it reaches a characteristic place along the cochlea. At this place, the traveling wave amplitude reaches a maximum and decays rapidly afterward. Each frequency has a characteristic place along the cochlea. The characteristic place for the highest audible frequencies are near the base and those for the lowest frequencies are near the apex. Properties of the basilar membrane such as geometry, mass, stiffness, and damping are important in determining the characteristics of the wave (Dallos et al., 1996; Pickles, 1988; Lighthill, 1991; Mammano and Nobili, 1993).

The transverse motions of the traveling wave generate the mechanical stimulus for the hair bundles. As depicted in Figure 1-3, when the tectorial membrane and basilar

membrane undergo transverse motions, they rotate about their connections to the spiral limbus. The hair bundles, which span the gap between the TM and the surface of the sensory epithelium, are deflected. These deflections of the stereocilia in the radial direction generate a sequence of mechanical, electrical, and chemical processes which result in nerve impulses being sent to the brain.

1.3 The tectorial membrane

1.3.1 Cochlear mechanical models and TM mechanical properties

Although it is widely agreed that there is an important mechanical interaction between the hair bundles and the TM, in comparison to knowledge of hair cell properties, relatively little is known about the TM. Efforts to model cochlear mechanics have attributed a wide range of properties to the TM and in doing so reflect the paucity of knowledge regarding its mechanical properties.

Historically, the TM has been modeled as a stiff bar. This condition is illustrated on the left in Figure 1-4. It is free to rotate about its attachment to the spiral limbus and is characterized by an infinite radial stiffness, infinite bending stiffness, and insignificant mass and damping (Davis, 1958; Bekesy, 1953; Bekesy, 1960; Steel, 1983b). However, simple models such as this could not explain the discrepancy between mechanical measurements of basilar membrane motion and corresponding measurements of responses from the auditory nerve (Patuzzi, 1996). Different models have been proposed which increase the complexity of the mechanism. Descriptions have been proposed in which the mass of the TM is important but the radial stiffness and damping are insignificant (Zwislocki and Cefaratti, 1988). In this case, shown on the right in Figure 1-4, the radial stiffness of the TM is much smaller than the stiffness of the hair bundles. The transverse resonance of the basilar membrane could be combined with a radial resonant system composed of the TM mass and hair bundle stiffness. Between these two extremes are descriptions which place importance on both radial

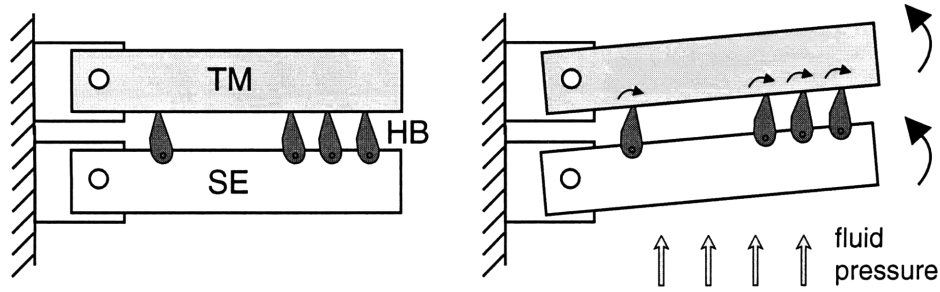


Figure 1-3: Schematic representation of the lever-model. Fluid pressures generate transverse motions of the sensory epithelium (SE) and the TM. As these structures rotate about their respective attachments along the spiral limbus (SL), they generate a shearing action on the hair bundles (HB) which causes the hair bundles to rotate about their base (right panel).

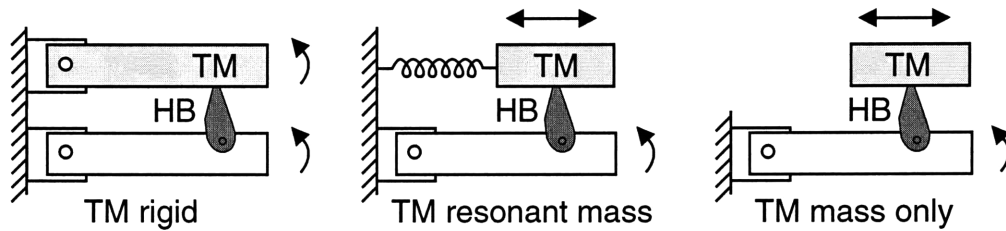


Figure 1-4: Mechanical models of the tectorial membrane and its interaction with hair bundles. The lever-model (left) assumes the radial stiffness of the TM is very large and that mass and damping are negligible. A resonant TM model (middle) includes both the radial stiffness and mass of the TM. A TM which has insignificant radial stiffness and damping, acts only as an inertial load on the hair bundles (right).

stiffness and mass of the TM (Allen, 1980; Zwislocki and Kletsy, 1979) as depicted in the middle illustration of Figure 1-4. The stiffness and mass of the TM act as a resonant system in the radial direction in addition to the transverse resonance of the basilar membrane.

Although the properties of the TM in the radial direction vary from infinitely stiff to negligible stiffness among the models, there is a common mechanical characteristic. The TM is portrayed as having an important mechanical anisotropy between radial and longitudinal properties. The longitudinal stiffness is negligible. Thus, there is no mechanical coupling in the longitudinal direction which means that transverse and radial movements in each cross-section are independent from neighboring cross-sections. (Mammano and Nobili, 1993; Allen, 1980; Patuzzi, 1996; de Boer, 1996).

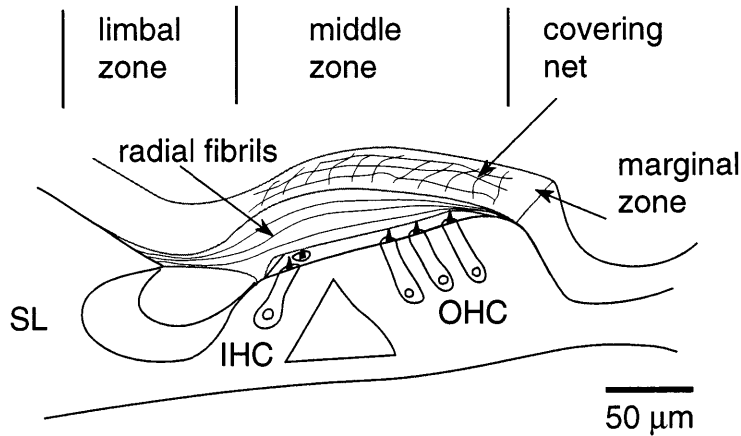


Figure 1-5: Different zones of the TM. The TM is attached to the spiral limbus by the thin limbal zone. The middle zone is thickest portion and marked on the top surface by the covering net. The middle extends over the hair cells and its structure is marked by distinct fibrils. At the outer edge is the marginal zone.

1.3.2 Biochemical composition and molecular structure

Recent biochemical studies of the TM have provided a description of the structure and composition of the TM which suggests a more complicated material than depicted by typical models. The TM is an acellular, polyelectrolyte gel (Kronester-Frei, 1978; Steel, 1983a; Thalmann et al., 1987; Thalmann, 1993; Thalmann et al., 1993; Hasko and Richardson, 1988; Shah et al., 1995; Tsuprun and Santi, 1996). Its composition is similar to other connective tissues, being described as a highly hydrated variant of cartilage. Water makes up 97% of the TM (Thalmann, 1993). Of the solid constituents, protein makes up 58 % of the dry weight of the TM (Thalmann, 1993). Of this protein, collagen type II is most prevalent. The organization of the constituents varies with position in the TM.

Different regions of the TM, illustrated in Figure 1-5, have different structural characteristics (Kronester-Frei, 1978; Hasko and Richardson, 1988; Lim, 1972; Lim, 1980; Slepecky, 1996). The TM is attached to the spiral limbus via the limbal zone which is a thin ($\approx 10 \mu\text{m}$) featureless region. The middle zone is the thickest portion of the TM ($\approx 40 \mu\text{m}$) and this region extends over the outer hair cells. The bottom surface of the middle zone makes a mechanical connection to the hair bundles. An irregular criss-crossing pattern of fibers make up the covering net which is on the

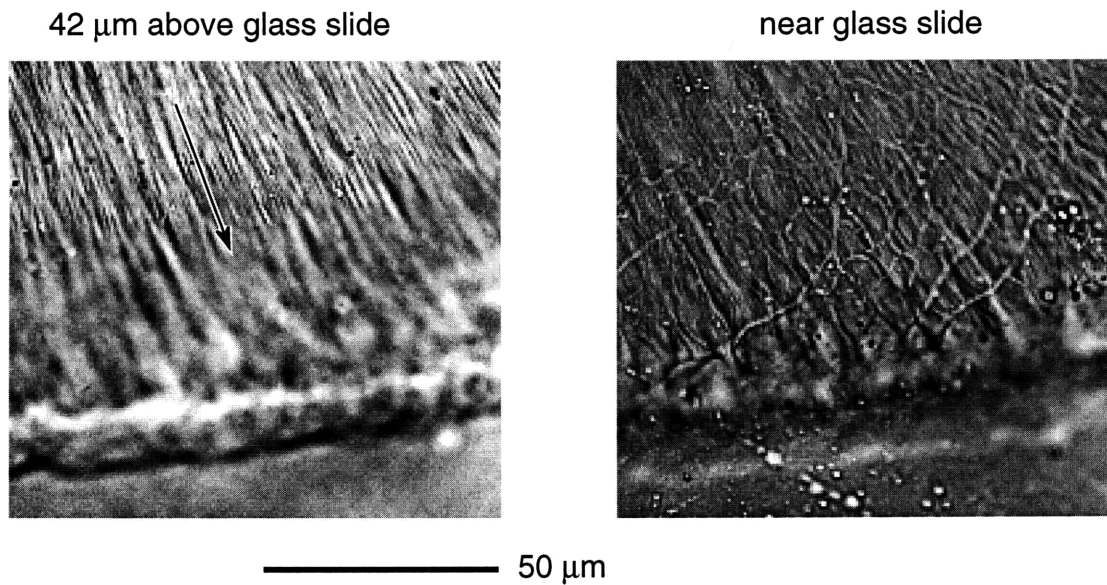


Figure 1-6: Light micrograph of isolated TM. Fibrils are visible as dark striations (left image), similar to those seen by Lim (1972). The arrow marks the direction parallel to the fibrils which is about 25 degrees from vertical. The covering net is a faint web like pattern, criss-crossing the surface of the TM (right image). The ridge at the bottom of the images is the marginal zone of the TM. Both images were taken from the same TM section at different planes of focus. The covering net side of the TM is glued to the surface of a glass slide.

top surface of the middle zone (Lim, 1972). In addition, collagen forms an array of radially oriented fibrils throughout the middle zone. The fibrils have diameters on the order of 7 nm and are separated from one another by 30 nm (Hasko and Richardson, 1988; Lim, 1972). The marginal zone is a region along the outer edge of the TM. The thickest middle zone occurs in the apex of the cochlea (Lim, 1972).

There are several important implications of the TM's composition. The orientation of the fibrils slants toward the apex of the cochlea. The slant is visible in the left micrograph of Figure 1-6 and appears to be correlated with the direction of maximum sensitivity of the outer hair cells as illustrated in Figure 1-7 (Lim, 1972). The direction of maximum sensitivity is parallel to the fibril direction suggesting the fibrils play an important mechanical role. The anisotropy in the TM composition and morphology may contribute to a mechanical anisotropy. Furthermore, the fluid content of the TM suggests that the membrane is not a rigid structure. The mechanical properties of gels are known to change with frequency (Ferry, 1970) and TM

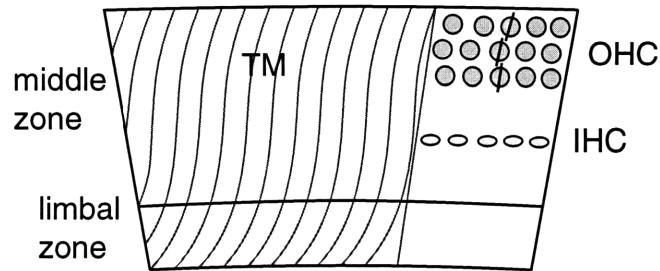


Figure 1-7: Radial fibrillar structure of the TM (adapted from Lim (1972)). The middle zone is marked by fibrils which runs radially at an angle typically 15 to 25 degrees (from vertical in the illustration). Bekesy (1960) noted fibers forming angles as much as 60 degrees near the limbal zone. The direction of maximum sensitivity of outer hair cells (OHC), depicted by the gray circles, is marked by the solid bisecting lines. The direction for each cell is roughly parallel to the fibril slant.

properties may have a similar dependence. Frequency dependent properties could have important implications for mechanical resonance.

1.3.3 Previous measurements of mechanical properties of the TM

Several investigators have observed the response of the TM to applied static forces as a means of determining mechanical properties of the TM. All the investigations used compliant probes to apply forces to the tissue in situ.

The first investigation was done by Bekesy (1953), who probed the mechanical properties of inner ear structures from several species, including human cadavers. By pressing the tip of a small hair onto the surface of the TM, he generated a depression in the tissue. The shape of the depression was long and narrow, running radially across the TM (Bekesy, 1953). This was interpreted as an anisotropy, suggesting that the TM was more mechanically rigid in the radial direction. In addition, quantitative stiffness measurements of various structures were attempted. As depicted in Figure 1-8, small compliant hairs were pressed into the surface of the TM at an angle which produced a force more or less normal to the surface. The hair was used to apply a vertical force. The resulting depth of depression of the tissue was observed. The ratio of the depression depth divided by the pressure applied by the probe served

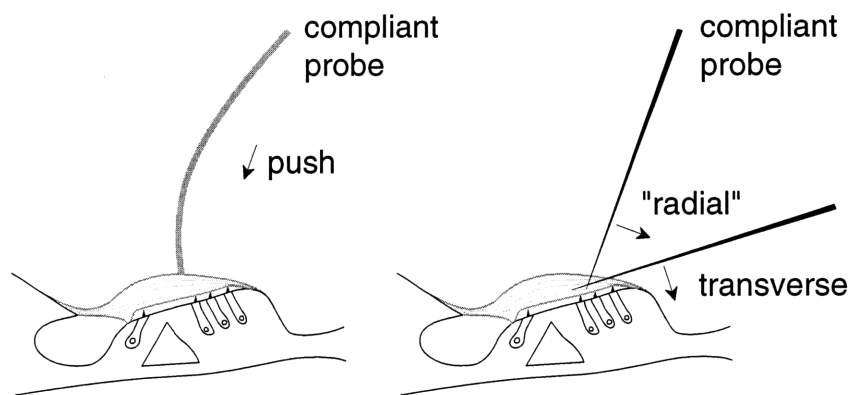


Figure 1-8: Compliant probes used to apply forces to the TM. Previous investigators have used compliant probes to apply forces normal (left panel) and various angles (right panel) to the surface of the TM. Bekesy (1953) pushed the tip of hairs onto the TM surface in situ (left panel). The right illustration depicts the technique used by Zwislocki and Cefaratti (1988) in which a glass pipette was used to apply forces in approximately radial and transverse directions (indicated by arrows).

as a measure of elasticity of the tissue. The elasticity of the TM was estimated to be approximately 0.05 cm/dyne which is equivalent to a stiffness (force divided by depression depth) of 0.02 N/m.

Bekesy (1960) also conducted qualitative investigations using a vibrating needle (200 Hz). The TM appeared stiff with respect to the vibrating needle, but lacked resistive force for slow static displacements. The conclusion was that the TM's elasticity was small compared to frictional or viscous mechanisms in the tissue.

Most recently Zwislocki and Cefaratti (1988) used fine glass pipettes to deflect the TM. The investigation was conducted on anesthetized guinea pigs. The pipette was inserted into the cochlea so that the TM could be deflected in approximately the radial and transverse directions as shown in Figure 1-8 (Zwislocki and Cefaratti, 1988). The deflection of the TM and the bend in the fiber were observed. The fiber was calibrated so that the force produced by a given bend was known. The stiffness reported was on the order of 0.125 N/m in both the radial and transverse directions.

Several issues have been raised regarding the use of compliant probes and in situ preparations to investigate mechanical properties of the TM. First, the TM is

transparent and is very difficult to observe in situ. The use of staining agents can significantly affect the mechanical response of the TM. Stains have been observed to increase the stiffness of the TM (Zwislocki and Cefaratti, 1988). Furthermore, the TM is a polyelectrolyte gel which is known to be sensitive to changes in the ionic composition of the surrounding fluid causing the tissue to shrink or swell (Shah et al., 1995; Freeman et al., 1994; Kronester-Frei, 1978). The geometry change may be accompanied by changes in the stiffness of the tissue. Second, access to the TM in situ is limited. The surface of the TM which is closest to the hair bundles which may be the most important mechanically, is not accessible. Third, the surrounding cochlear structures in situ, which are mechanically coupled with the TM, have their own mechanical properties. Deformations of the TM will include deformations of other structures. As a result, interpreting measurements in terms of intrinsic mechanical properties of the TM is difficult. Fourth, large static deformations ($\approx 20\mu\text{m}$) have been used to probe the TM. These deformations are not representative of in vivo displacements, which are as small as picometers, or auditory frequencies, which range from 10 to 20 kHz.

In response to the need for quantitative measurements of TM mechanical properties, a new experimental method has been developed. The method applies calibrated, dynamic forces to the isolated TM using a magnetizable bead.

Chapter 2

Magnetic Bead Method

This chapter describes the magnetic bead method. Fundamental principles involved in producing a magnetic force are presented and are followed by a discussion of the apparatus used to generate forces and measure motions.

2.1 Background

Investigations of biological fluids using magnetic beads have been conducted since the early 1920s. Early experiments consisted of dragging a nickel or iron sphere through the fluid with a magnet. The speed of the sphere was observed by the experimenter and used to estimate the viscosity of the fluid. Since then investigators have used magnetic bead methods to apply non-oscillatory (Seifriz, 1924; Crick and Hughes, 1950; Hiramoto, 1969; Wang et al., 1993; Valberg and Albertini, 1985; Amblard et al., 1996) and oscillatory (Lutz et al., 1973; King and Macklem, 1977; James and Marriott, 1982; Tran-Son-Tay et al., 1988; Amblard et al., 1996) forces to several biological fluids and cellular structures. Two types of non-oscillatory forces have been used. One type applies a force to a magnetic particle in a single direction and measures the resulting displacement of the particle — which is similar to the first investigations in the 1920's (Crick and Hughes, 1950; Hiramoto, 1969). A second type produces a permanently magnetized particle by applying a large magnetic field and polarizing the particle in a chosen direction (Wang et al., 1993; Valberg and Albertini, 1985). A smaller magnetic

field is then applied in an orthogonal direction which causes the particle to twist and align itself with the smaller field. The degree to which the particle aligns over time is measured. This type of torsional force has been used to study the properties of cytoplasm (Crick and Hughes, 1950; Valberg and Albertini, 1985) and cytoskeletal stiffness of cells (Wang et al., 1993). In addition, a multi-degree-of-freedom system which can produce both controlled translation and rotations was recently described (Amblard et al., 1996).

The use of oscillatory forces did not occur until the 1970s. Measurements using oscillatory forces have been used to investigate viscoelastic properties of biological fluids (Lutz et al., 1973; King and Macklem, 1977; James and Marriott, 1982; Tran-Son-Tay et al., 1988; Amblard et al., 1996) such as mucus and blood. Typically, solenoid electromagnets (iron rod wrapped with current carrying wire) are used to generate a sinusoidal force on a steel sphere. Methods using oscillatory forces have the advantage that frequency dependent properties of a specimen can be probed.

Using either oscillatory or non-oscillatory methods, the motion of the sphere or bead provides information about the mechanical properties of the biological material. By far the most popular motion measurement methods have been optical. Early investigators using bead methods made manual measurements looking through a light microscope. This considerably limited the type of measurements which could be made. The motions had to be large and relatively slow. In the 1970's, investigators began to use other optical methods. The image of the bead was magnified and projected onto an array of photodiodes (Lutz et al., 1973; King and Macklem, 1977; James and Marriott, 1982). This method provided a significant increase in the spatial and temporal resolution of the measurements. More recently, non-optical methods have been used. The torsional experiments conducted by Valberg and Albertini (1985) and Wang et al. (1993) use a galvanometer to measure the strength and orientation of the magnetic field produced by an ensemble of permanently magnetized beads. Oscillatory motions have also been measured acoustically by Tran-Son-Tay et al. (1988). The non-optical methods have particular applications for measuring motions in opaque biological fluids.

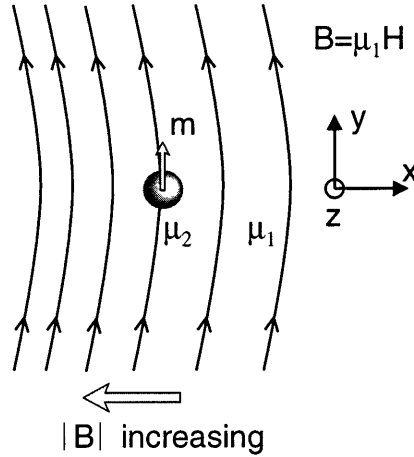


Figure 2-1: Magnetizable bead in a magnetic field with a field gradient. The magnetic field, $\mathbf{H} = \mathbf{B}/\mu_1$, induces a magnetic moment \mathbf{m} in the bead in the direction of the field. The bead is not drawn to scale: it has dimensions that are small compared to the characteristic dimensions of the gradient. The bead and surrounding medium have permeabilities of μ_2 and μ_1 respectively. The magnetic moment interacts with the gradient in the magnetic flux density \mathbf{B} to produce a force on the bead. The force is in the direction of increasing field strength.

The magnetic bead method presented in this thesis applies oscillatory forces to solid tissues. The bead is attached to a small surface region of the tissue (about $10 \mu\text{m}$ in diameter) and computer controlled electromagnets produce a force on the bead which is transmitted to the tissue. The resulting motion of the bead and the deformations of the tissue are measured using a video microscopy system.

2.2 Producing a magnetic force: Theory

When a magnetizable bead is placed in a magnetic field, it will experience a force resulting from the magnitude and gradient of the applied field. The illustration of Figure 2-1 shows the process of generating a force on a bead schematically. A magnetic field \mathbf{H} induces a magnetic dipole moment in the bead. If the radius is small relative to the characteristic dimensions of the field gradient and if the permeability μ_2 of the bead is large, the dipole moment can be approximated by solving Maxwell's equations for an infinitely permeable sphere in a uniform field. In this case, the equations of

interest are

$$\nabla \cdot \mathbf{B} = 0 \quad (2.1)$$

$$\nabla \times \mathbf{B} = 0 \quad (2.2)$$

where $\mathbf{B} = \mu\mathbf{H}$. The induced dipole moment can be written as

$$\mathbf{m} = 4\pi \frac{\mu_2 - \mu_1}{\mu_2 + 2\mu_1} r^3 \mathbf{H} \quad (2.3)$$

where μ_1 is the permeability of the space surrounding the bead, μ_2 is the permeability of the bead, and r is the bead radius (Zahn, 1979). Equation 2.3 shows that the magnetic dipole is proportional to the magnitude of the applied field and is oriented in the direction of the applied field (Figure 2-1).

The induced dipole interacts with the gradient of the applied field to produce a force on the bead. The force on a magnetic dipole can be written as

$$\mathbf{f} = (\mathbf{m} \cdot \nabla) \mathbf{B} \quad (2.4)$$

which using Equation 2.3 provides an expression for the force on a small, highly permeable, spherical bead

$$\mathbf{f} = \left(4\pi \frac{\mu_2 - \mu_1}{\mu_2 + 2\mu_1} r^3 \mathbf{H} \cdot \nabla \right) \mathbf{B}. \quad (2.5)$$

The vector expression in Equation 2.5 can be simplified. For Figure 2-1, \mathbf{H} is in the y direction which means

$$(\mathbf{H} \cdot \nabla) \mathbf{B} = H_y \left(\frac{\partial B_x}{\partial y} + \frac{\partial B_y}{\partial y} + \frac{\partial B_z}{\partial y} \right), \quad (2.6)$$

where the subscripts x , y , and z indicate vector components in the x , y , and z directions. The terms on the right side of Equation 2.6 can be rewritten using Equations 2.1

and 2.2. Following from Equation 2.1,

$$\frac{\partial B_y}{\partial y} = - \left(\frac{\partial B_x}{\partial x} + \frac{\partial B_z}{\partial z} \right)$$

and from Equation 2.2

$$\frac{\partial B_x}{\partial y} = \frac{\partial B_y}{\partial x}$$

and

$$\frac{\partial B_z}{\partial y} = \frac{\partial B_y}{\partial z}.$$

Thus, Equation 2.5 can be written as

$$\mathbf{f} = \left(4\pi \frac{\mu_2 - \mu_1}{\mu_2 + 2\mu_1} r^3 H_y \right) \left(\frac{\partial B_y}{\partial x} \hat{\mathbf{i}}_x - \left(\frac{\partial B_x}{\partial x} + \frac{\partial B_z}{\partial z} \right) \hat{\mathbf{i}}_y + \frac{\partial B_y}{\partial z} \hat{\mathbf{i}}_z \right)$$

in which $\hat{\mathbf{i}}_x$, $\hat{\mathbf{i}}_y$, and $\hat{\mathbf{i}}_z$ are unit vectors in the x , y , and z directions respectively.

However, in Figure 2-1

$$B_x = B_z = \frac{\partial B_y}{\partial z} = 0.$$

As a result, the magnetic force on the bead is

$$\mathbf{f} = \left(4\pi \chi r^3 H_y \right) \frac{\partial B_y}{\partial x} \hat{\mathbf{i}}_x \quad (2.7)$$

where

$$\chi = \frac{\mu_2 - \mu_1}{\mu_2 + 2\mu_1} = \frac{\frac{\mu_2}{\mu_1} - 1}{\frac{\mu_2}{\mu_1} + 2}.$$

There are several important implications of Equation 2.7. Characteristics of the applied field affect the magnitude and direction of the force. In this case, the force is always in the direction of increasing magnetic field strength. The properties of the bead affect the force in two ways. First, the force is proportional to r^3 so that larger beads produce larger forces. Second, the permeability of the bead affects the coefficient χ such that χ increases as the relative permeability increases.

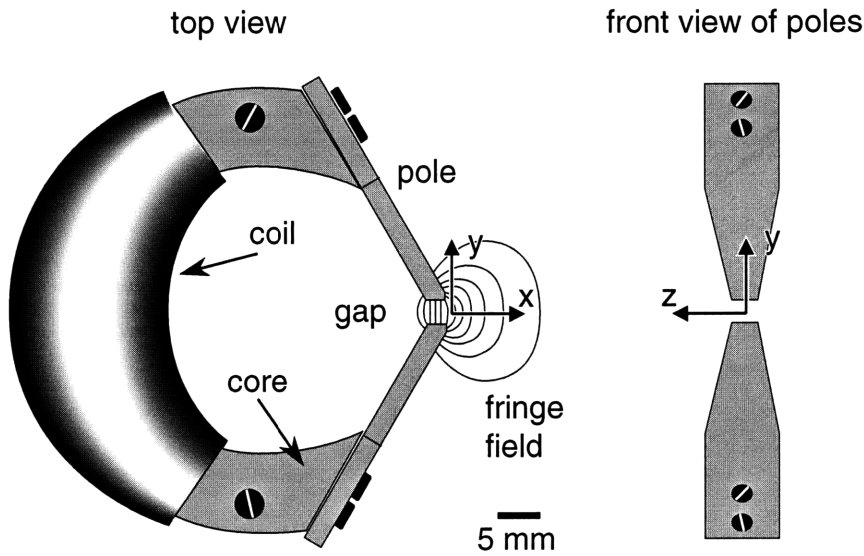


Figure 2-2: Top view of the ring magnet used for the magnetic bead method. The ring magnet has a core and poles made of pure iron. A coil of copper wire is wrapped around one side of the core. There is a gap between the tips of the poles opposite the coil. Magnetic field produced by current in the coil is channeled by the iron core and poles until it reaches the gap where it produces a fringe field. Along the x axis, the fringe field is parallel to the y axis due to symmetry.

2.3 Producing a magnetic force: Ring magnets

An electromagnet provides the field and field gradient used to generate the force on the bead. A typical electromagnet consists of a core surrounded by a coil of wire. When electric current is passed through the coil, magnetic flux is generated. The purpose of the core is to constrain and provide a path for the magnetic flux, similar to how a hose channels water. The degree to which the core channels the flux is dependent on magnetic properties and geometry of the core.

2.3.1 Magnetic and material properties of core

The reluctance and inductance associated with the core, the eddy currents generated in the core and the saturation flux density of the core material are magnetic properties characterizing the effectiveness of the core to channel flux.

Reluctance. The magnetic reluctance R of a material is the magnetic analog to electrical resistance, where the magnetic flux plays the same role as current density.

The reluctance depends on the material properties as well as the geometry of the core. Symbolically, the reluctance is

$$R = \frac{l}{\mu A}$$

where l is the characteristic length of the flux path through the core, μ is the permeability of the material, and A is the cross-sectional area of the core (Zahn, 1979). The permeability of the core is a measure of how readily magnetic flux passes through the material. The core with a high magnetic permeability serves as a low resistance path for the magnetic flux. In order to maximize the channeling of flux by the magnet core, the reluctance should be minimized. For a given length l , a larger permeability and a larger cross-sectional area A improve performance. However, the core cross-section and material introduce other constraints.

Inductance. The inductance of the magnet increases with A as well as with both the number of turns in the wire coil and the permeability of the core. A large inductance degrades the performance of the magnet at high frequencies by increasing the electrical impedance. When the impedance increases, a larger voltage is needed to produce the same magnetic field. The complex electrical impedance of an electromagnet can be written as a resistance in series with an inductance

$$j\omega L + R$$

where L is the inductance, R is the resistance, and ω is the frequency. For a typical inductance and resistance of 0.006 henries and 4 ohms respectively (measured for the magnets used in this thesis), the frequency at which the inductance term ωL becomes important is approximately 1000 Hz.

Eddy currents. In addition to the inductance, high frequency magnetic fields are affected by induced eddy currents in the core. These currents serve to reduce the magnetic flux channeled by the core as well as cause ohmic heating of the core. The

property	pure iron	ferrite
μ	25×10^3	5×10^3
\mathbf{B}_{sat}	2.3 T	0.5 T
δ (@ 1000 Hz)	5 cm	160 m
machineability	easy	difficult

Table 2.1: Comparison of material properties for pure iron and ferrite. The symbols μ , \mathbf{B}_{sat} , and δ are the relative permeability, saturation flux density, and skin depth respectively.

skin depth defines the characteristic penetration of the magnetic field into the core and can be written as

$$\delta = 0.564 \sqrt{\frac{\rho}{\mu f}}$$

where f is the frequency of the time varying field, μ is the permeability of the core, and ρ is the electrical resistivity of the core (Zahn, 1979). For large δ compared to the core cross-section dimensions, eddy currents are not a significant effect.

Saturation flux density. Saturation flux density is a material property which limits both DC and AC fields. It is a measure of how much magnetic flux can be channeled by the core. Most materials have saturation flux densities below 2.4 T.

Machineability. The ability to manufacture a magnet core is an important material characteristic. Typical core materials range from metallic to ceramic and range from soft and easy to machine, to brittle and difficult to machine.

Comparison of pure iron and ferrite. For most core materials, there is a tradeoff among various properties. Pure iron (99.95%) and ferrite are two materials commonly used in magnetic applications and are compared in Table 2.1. Both materials have high relative permeabilities, providing a good path for magnetic flux. In addition, for a core with characteristic dimensions on the order of 12 mm, eddy currents are probably not important up to 1000 Hz for either material. The two most important characteristics of the magnets used in this thesis were the saturation flux density and the machineability of the material. As a result, the magnet cores were manufactured

from pure iron (99.95%, Pure Tech Inc., Carmel, NY).

2.3.2 Geometry of core

The shape of core was not necessarily designed to optimize magnet performance but was intended to channel the flux to a particular location. The ring magnet geometry shown in Figure 2-2 is a geometry typically used in tape recording heads. The magnetic flux is channeled through the core (0.5" or 12 mm square cross-section) to the magnet poles which are separated by a gap. In the gap, the flux spreads out and generates a fringe field. The fringe field provides the field and the gradient which generate the force on the bead. The poles can be adjusted to change the gap width which in turn changes the fringe field magnitude and characteristic dimension of the gradient. Understanding the relation between magnet geometry and the generated field is important for understanding the performance of the magnetic bead method. Although, the actual relationship between the magnet geometry and generated forces is complicated, a simplified model was investigated.

2.3.3 Karlquist model

Several closed form expressions have been developed to describe the field near the gap of a ring magnet. The expressions were the result of work done on magnetic recording heads in the 1950s (Ciureanu and Gavrilă, 1990). The simplest expression was developed by Karlquist for the idealized magnet geometry shown in Figure 2-3. The magnet gap is defined by $-g/2 < y < g/2$ where g is the gap width. The magnet core is modeled as two semi-infinite surfaces, separated by the gap, defined by the region $x < 0$. The gap and surfaces extend to $\pm\infty$ in the z direction. The model involves several assumptions: the magnetic field in the gap H_o is constant and the core is an equipotential surface with infinite permeability. Based on these assumptions, Karlquist derived a solution for the magnetic field in the region $x > 0$ using conformal mapping techniques (Ciureanu and Gavrilă, 1990).

For a bead positioned along the positive x axis, the important field component is

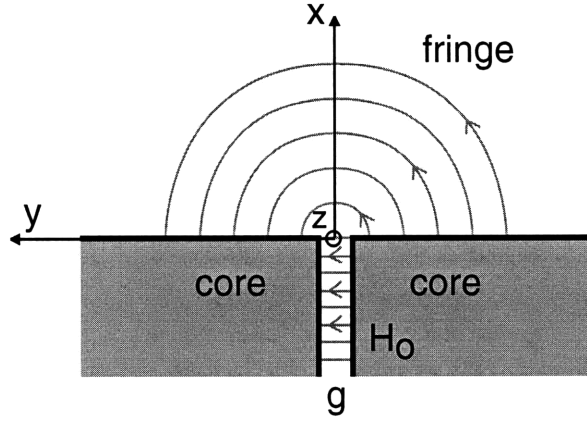


Figure 2-3: The magnet geometry for Karlquist model. The cores (shaded regions) are separated by a gap g and are assumed to be equipotential surfaces, having infinite magnetic permeability. They extend to infinity in the positive and negative y directions and have infinite extent perpendicular to the page in the z direction. The magnetic field in the gap and fringe is schematically represented by the gray lines. The fringe field extends along the positive x axis. The field in the gap H_0 is constant.

the y component H_y , which corresponds to the field shown schematically in Figure 2-1.

This component of the fringe field can be written as

$$H_y(x, 0) = \frac{H_0}{\pi} \left(\arctan \frac{g}{2x} - \arctan \frac{-g}{2x} \right) \quad (2.8)$$

and its gradient in the x direction is

$$\frac{\partial H_y}{\partial x}_{y=0} = -\frac{H_0}{\pi} \frac{g}{x^2 + (g/2)^2}. \quad (2.9)$$

According to Equation 2.7, the force on a bead is proportional to the product of Equation 2.8 and Equation 2.9. In this case, the force is

$$F = C \left(\arctan \frac{g}{2x} - \arctan \frac{-g}{2x} \right) \frac{g}{x^2 + (g/2)^2} \quad (2.10)$$

where the value of the coefficient C is proportional to the square of the gap field and also depends on the radius and material properties of the bead. C does not depend on core geometry.

The field and force expressions based on Karlquist's model have important implications. The force expressed in Equation 2.10 is a function of both the gap width

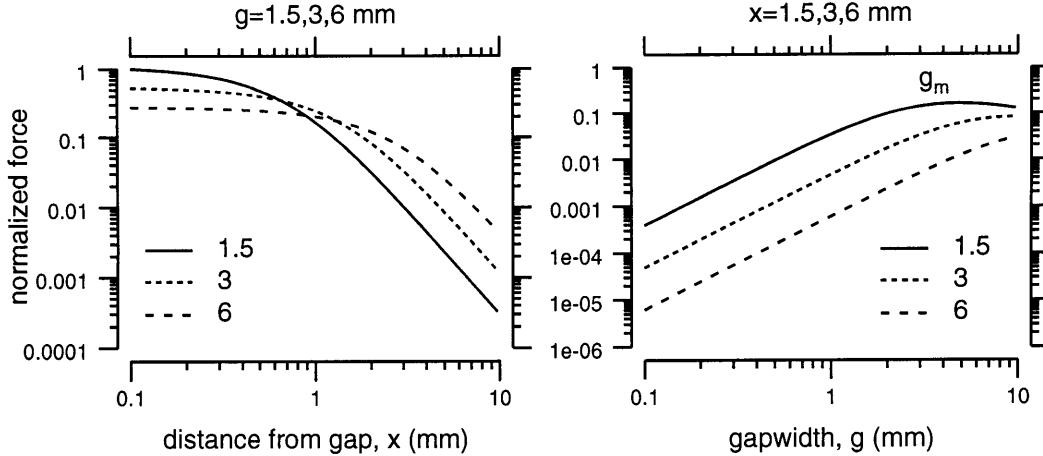


Figure 2-4: Effect of gap width g and distance from the gap x on the magnetic force predicted by the Karlquist model. The left panel shows the force as a function of distance from the gap for $g = 1.5$ mm, 3 mm, and 6 mm. The right panel shows the predicted force as a function of the gap width for $x = 1.5$ mm, 3 mm, and 6 mm. The forces are normalized with respect to the maximum force which occurs at a distance of 1.5 mm and a gap width of 1.5 mm.

g and the bead's distance from the gap x . The effect of variations in g and x are presented in Figure 2-4. When the gap width is fixed and the bead distance is increased, the force on the bead decreases. This trend is present regardless of the gap width. Thus, the closer the bead is placed to the ring magnet, the larger the force. This is not surprising: Equation 2.7 implies that the force increases in the direction of increasing field strength (toward the gap). Alternatively, if the distance from the gap is fixed and the gap width is increased, there is a gap width g_m which produces the largest force. As x increases, the value of g_m increases while the sensitivity of the force near the g_m decreases.

2.3.4 Measuring the relation between gap width and force

The Karlquist model is two dimensional. Although, similar trends are expected for a three dimensional gap and magnet, the details of the force variations will be different. For example, Figure 2-5 shows that the field strength falls off more rapidly in the three dimensional case. In order to characterize the three dimensional trends, we measured the relationship between force and variations in g and x empirically.

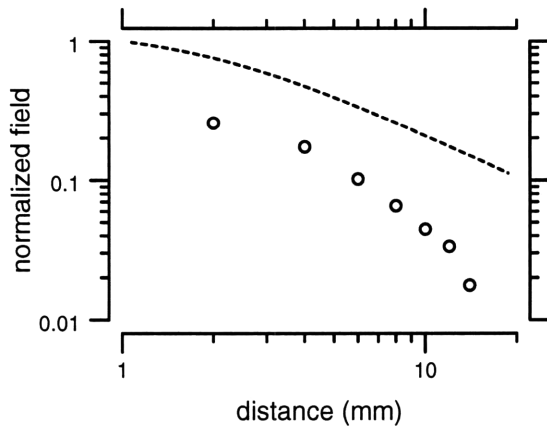


Figure 2-5: The plot compares a measured fringe field with the field predicted by the Karlquist model. The field was measured using a hall effect sensor and each symbol represents the average of 12 independent measurements. The dotted line is the fringe field predicted by the Karlquist model based on the measured field in the gap. The Karlquist field at $x = 1$ mm was used to normalize the data.

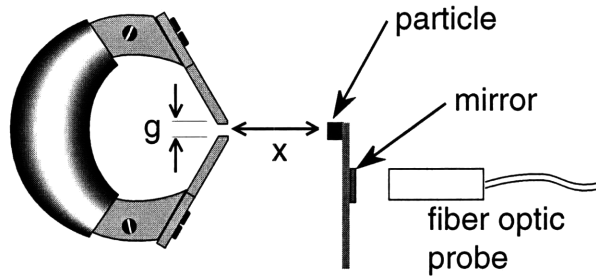


Figure 2-6: Apparatus used for measuring force as a function for gap width. A small magnetizable particle (ferrite) is glued to a tungsten filament. A front surface mirror attached to the filament is used as a target for a fiber optic probe. The probe measures deflections of the filament when current is applied to the magnet for various gap widths g and distances x .

Method. A small magnetizable, ferrite cube ($70 \mu\text{m}/\text{side}$), was attached to the tip of a tungsten filament (0.005 inch diameter filament, 2 cm length). The base of the filament was attached to a micromanipulator, which allowed positioning of the particle relative to the ring magnet. In addition, a small front-surface mirror was glued on the filament near the particle location. The arrangement is shown in Figure 2-6. The poles of a ring magnet were adjusted with digital calipers to create a gap width of 1.5 mm, 3 mm, or 6 mm. The magnetizable particle was positioned along the x axis at distances of 1.5 mm, 3 mm, or 6 mm. Thus, there were 9 different gap width/distance combinations. At each combination, a range of DC currents from 0.3 to 2 amps was applied to the ring magnet coil. The resulting displacement of the

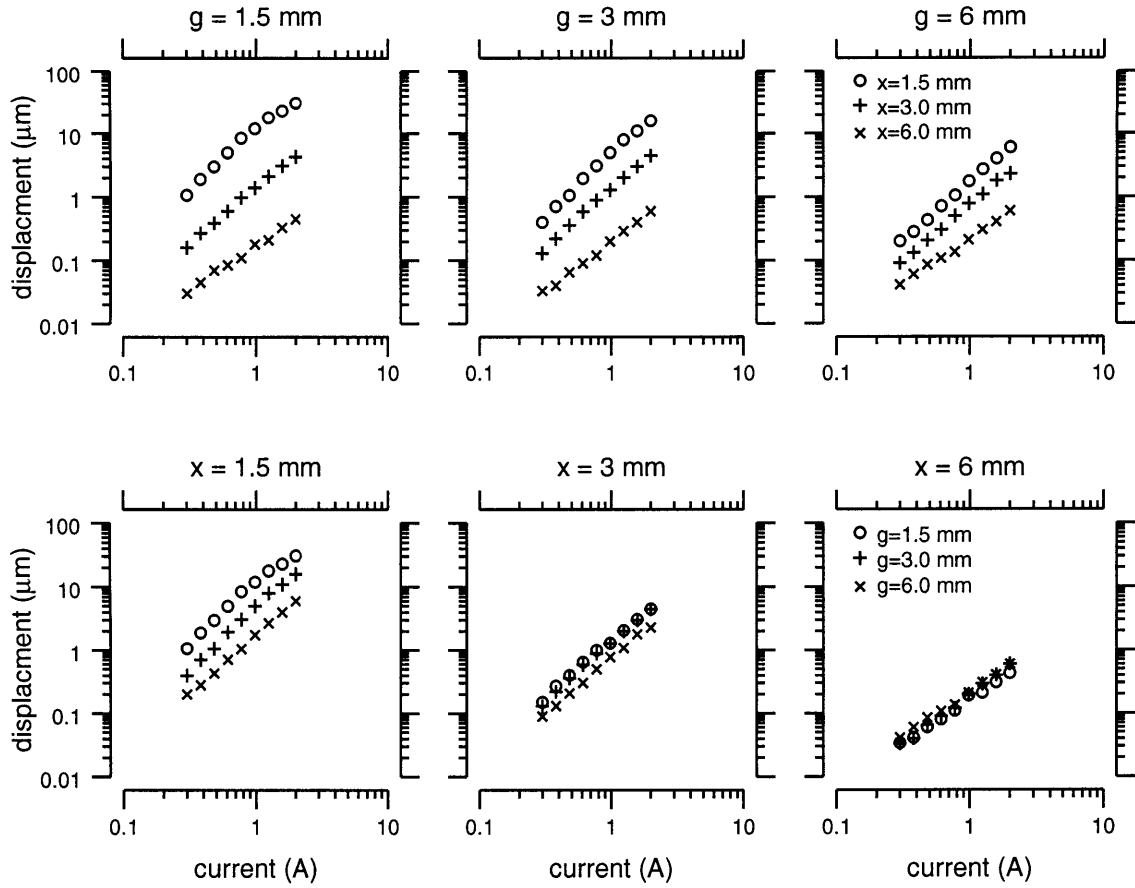


Figure 2-7: Effect of gap width g and distance from gap x on magnetic force. Effects were assessed by measuring the displacement of a ferrite particle attached to a tungsten cantilever as a function of current through the ring magnet coil. Each symbol represents the average of 3000 displacement measurements with a fiber optic probe. The top panels show results for $g = 1.5$ mm (left), 3 mm (middle), and 6 mm (right). The bottom panels show the same results reorganized by distance from the gap: $x = 1.5$ mm (left), 3 mm (middle), and 6 mm (right).

particle is proportional to the magnetic force. In order to estimate the displacement, a fiber optic probe (Angstrom Resolver, Opto Acoustics, Raleigh, NC) was used which measured the distance between the probe tip and the reflecting surface of the mirror. Several thousand displacement estimates were acquired at each current level.

Results. The results for 9 gap width/distance combinations are shown in Figure 2-7. The trends are consistent with the Karlquist model. The top panels in Figure 2-7 indicate that the force on the particle is larger when it is closer to the magnet, regardless of the gap size. In the bottom panels, the measured force is insensitive to

	x = 1.5 mm	x = 3.0 mm	x = 6.0 mm
g = 1.5 mm	10	1.2	0.2
g = 3.0 mm	5	1.1	0.2
g = 6.0 mm	2	0.8	0.2

Table 2.2: Particle displacements for various gap widths (rows) and distances from magnet (columns). The displacements were measured for a coil current of 1 amp.

gap width for distances greater than 3 mm. This is consistent with the increasing insensitivity of the force in Figure 2-4. The results are summarized in Table 2.2. The table values are particle displacements measured at a coil current of 1 amp.

Conclusion. Measurements of TM mechanical properties with the magnetic bead method depend on generating forces large enough to produce measurable motions. To produce the largest forces possible, the TM and bead should be as close to the magnet as is practical and the gap width should be small.

2.4 Producing a magnetic force: The magnetic field

Several properties of the ring magnet fringe field were examined empirically. The dependence of the fringe field magnitude on current magnitude and frequency was measured. Spatial variations in the field were also measured.

Method. A fringe field is produced with a ring magnet by passing current through 500 turns of 22 AWG copper wire. The current is supplied using a current amplifier (Techron #7550, 2 channel, 180 watts minimum power output, Techron, Elkhart, IN) whose output is proportional to an input voltage waveform from a computer. The amplifier can be operated in a controlled current mode (current amplitude constant with frequency) or a constant voltage mode (voltage amplitude constant with frequency). The magnetic field is measured using a hall-effect probe (Walker Scientific Inc., model MF-5D, hall probe HP-145S) with an active area of 1 mm². The active

area defines the spatial resolution of the probe. Probe measurements reflect the magnitude of the flux density \mathbf{B} which passes through the probe orthogonal to the active area. The probe was attached to a micromanipulator which allowed adjustment of the probe position relative to the magnet.

Using the hall-effect probe, the relation between the magnitude of the fringe field and the applied current was measured. Both DC and AC currents were applied to the coil and the resulting field was measured at the location where the TM is typically positioned during an experiment. The coil current was monitored by measuring either the voltage across a 2 ohm, 50 watt resistor in series with the coil or using a current monitor output on the power amplifier.

Results: DC field. DC current magnitudes from 0.25 to 6.6 amps (positive and negative currents) were applied to the magnet coil and the plot in Figure 2-8 shows the measured field versus the applied coil current. The difference between the measured field for positive and negative currents is indicative of residual magnetism in the core. The residual field produces an increase in the measured field of at most 30% for currents of 0.3 amps and less than 5% at 2 amps. The polarity of the current applied to each magnet is not changed during TM experiments. In addition, the solid lines in the plot show the distinct change in slope from a slope of 1 below 2.7 amps to a slope of 0.25 at high current levels. A slope of 1 indicates the field is linearly proportional to the applied current. The change in slope indicates saturation of the core at a fringe field magnitude of 0.1 tesla.

Results: AC field. An AC signal which produces a peak current amplitude of 1.4 amps at 10 Hz was sent to the current amplifier. The frequency of the signal was varied from 1 Hz to 1 kHz and the peak amplitude of the fringe field was measured using the hall effect probe. Results with the amplifier in controlled current mode and in constant voltage mode are shown in Figure 2-9. The controlled current mode helps reduce the effects of magnet losses. Without controlled current, the fringe field falls off rapidly above 10 Hz.

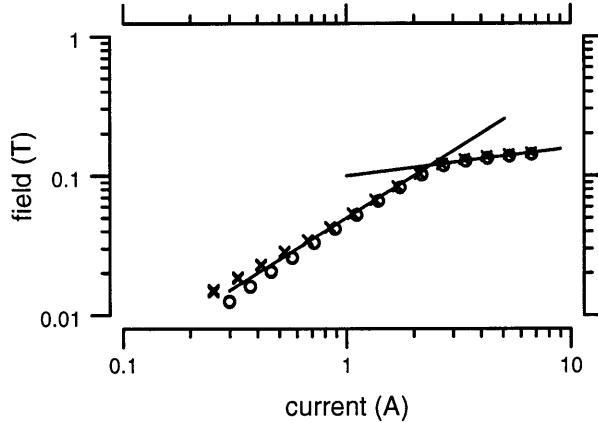


Figure 2-8: DC magnetic field of ring magnet. DC measurements of the magnetic flux density \mathbf{B} are plotted for a range of currents applied to the magnet coil. The solid lines represent slopes for currents below and above 2.7 amps. For currents below 2.7 amps the measured field follows a slope of 1. The slope for currents above 2.7 amps is 0.25. Each point represents the average of 3000 field measurements. The circles correspond to positive currents and the x's correspond to negative currents.

Results: Spatial dependence of field. As shown in the Karlquist magnet model, the magnitude of the fringe field decreases with increasing distance from the gap. This spatial dependence is essential for producing a force on the bead. However, it can also produce spatial variations in the magnetic force. The plots in Figure 2-10 show the variation in \mathbf{B} with position. The probe was held in a 3 axis micromanipulator and was moved to traverse a straight path from the magnet gap outward along the x axis (shown in Figure 2-2) in 1 mm increments. Similar measurements were done in the y and z directions. The plots shown in Figure 2-10 show the magnetic flux density as a function of distance from the ring magnet gap for a DC current of 2 amps. Notice that the measured field in the x direction is not symmetric about the origin, indicating a gradient $\partial H/\partial x$ of approximately 0.03 T/mm. The measured field in the y and z directions are nearly symmetric about the origin which indicates that the corresponding gradients at this point are zero and therefore, from Equation 2.7, the forces are zero in the y and z directions. Thus, the force is predominantly x directed.

Discussion. The results of the field measurements have important implications for the implementation of the magnetic bead method. The saturation of the magnet core at 2.7 amps constrains the magnitude of the fringe field. Current waveforms with

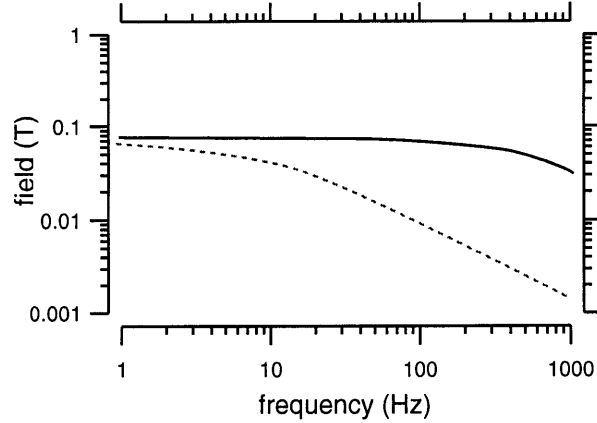


Figure 2-9: Fringe field measured as a function of frequency. The dotted line shows the frequency response of the field with a constant voltage amplitude applied to the coil (constant voltage mode). The break frequency in this case is around 10 Hz. The solid line shows the frequency response with a constant coil current amplitude (controlled current mode).

amplitudes greater than 2.7 amps will produce temporally distorted fringe field waveforms. In addition, the measurements of the spatial variation of the field show that a single magnet can only produce a force in the direction of the gap. Consequently, in order to produce oscillations of a bead, in which forces are applied alternately in opposite directions, two ring magnets are required. The combination of these two results require that a rather complicated current waveform must be applied to each magnet to generate sinusoidal forces on a bead.

Equation 2.7 shows the force is proportional to $|B_y|^2$ (given that $B_y = \mu_1 H_y$). Furthermore, the plot in Figure 2-8 indicates a linear relationship between the applied current and B_y . Thus, the force is proportional to the square of the applied current. As a result, in order to produce a sinusoidal force, the current waveform applied to the magnets, as depicted in Figure 2-11, must be the square root of a sine wave. This wave form must then be split between two ring magnets to generate a sinusoidal force on a bead.

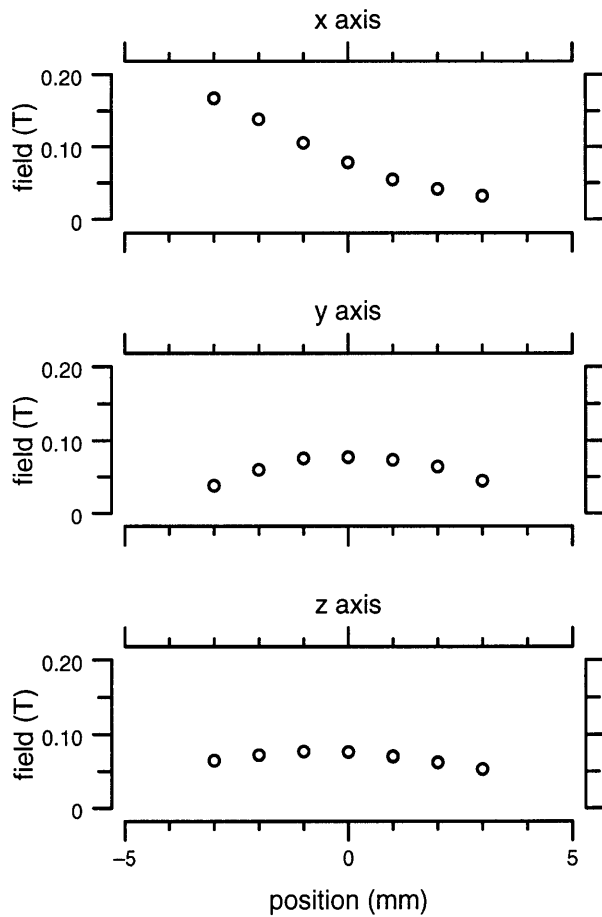


Figure 2-10: The spatial variation in \mathbf{B} . Measured values of \mathbf{B} along the x , y , and z axes are shown in the top, middle and bottom plots respectively. The origin of the axis is at the location typically occupied by the TM chamber. Each symbol is an independent field measurement using a hall-effect probe.

2.5 Producing a magnetic force: Magnetizable beads

As with the core, the material properties and dimensions of the bead are important parameters. The material affects the bead's magnetic properties and the size affects both the magnitude of the force and the area over which the force is transmitted to the TM.

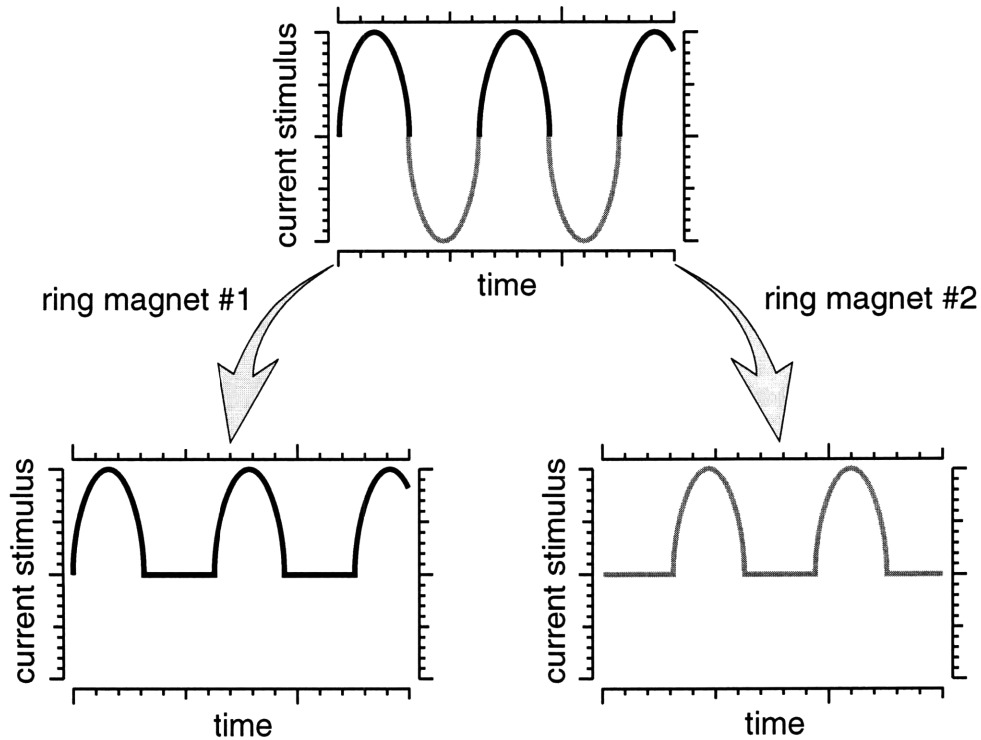


Figure 2-11: The current stimulus for the ring magnets. The force is proportional to the square of the current. Therefore, the current waveform $\sqrt{\sin t}$ is used to produce sinusoidal forces. The force on the bead is always directed toward the magnet gap, regardless of the direction of the current in the magnet coil. Thus, to produce oscillatory forces the waveform is split between two magnets.

2.5.1 Bead material

The permeability of the bead μ_2 plays a role in the coefficient χ but is typically not a strong influence on the magnetic force expressed in Equation 2.7. The plot in Figure 2-12 shows the value of χ for various values of μ_2/μ_1 (relative permeability) where μ_1 is the permeability of free space. The value of χ approaches 1 rapidly, reaching 0.9 for $\mu_2/\mu_1 = 20$. Bead materials having relative permeabilities greater than 1000 are widely available (Lide, 1997). As a result, differences in bead permeability are not typically important.

A more important parameter is the remanance of the bead. A bead with a high remanance will remain permanently magnetized when the external field is turned off. A permanently magnetic bead will always try to align itself with the polarity of the external field, like a compass needle trying to point north. The result is the bead

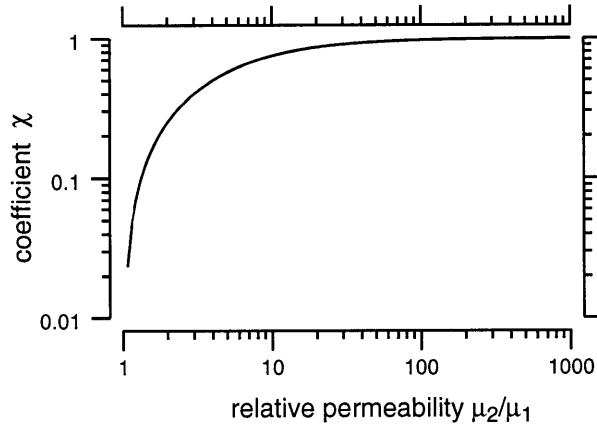


Figure 2-12: The sensitivity of the coefficient χ of Equation 2.7 to relative permeability μ_1/μ_2 of the bead. For relative permeabilities above 20, χ is larger than 0.9.

twists rather than displacing, which is a technique used by Valberg and Albertini (1985) and Wang et al. (1993). Twisting motion is not a desired motion in this case. Beads made from 6%SiFe (Ultrafine Powder Technology Inc., Woonsocket, RI) have a low remenance and a relative permeability near 5000.

2.5.2 Bead size

The size of the bead is determined from a rather practical point of view. A bead is required which is large enough to produce measurable deformations of the TM but not so large that the area of interaction between the bead and the TM is many times greater than the area of interaction which might be occurring in situ between a hair bundle and the TM (a region on the order of $10 \mu\text{m}$ in radius). Bead radii from 6 to $18 \mu\text{m}$ are used in TM experiments.

2.6 Measuring Motion: Computer microvision

The measurement of bead motion and TM deformation is done using a computer microvision system (Davis, 1997). As shown in Figure 2-13, the computer microvision system has several components. Generally speaking, there are two operations carried out by the system: video images of the specimen are acquired and quantitative motion estimates are determined from the images.

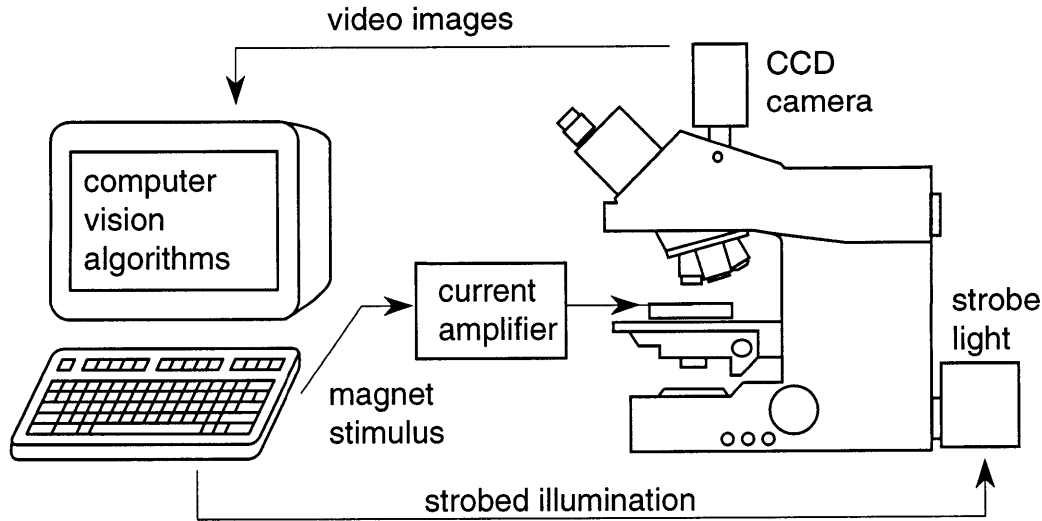


Figure 2-13: Schematic representation of the system used to measure the motions of the magnetizable bead and TM. A computer generates a voltage stimulus which is sent via a controlled current amplifier to the magnets. Magnified, strobe illuminated images of the bead and TM are acquired with a light microscope equipped with a CCD camera. Computer vision algorithms determine displacement estimates from the images.

2.6.1 Image acquisition

The system used to acquire images is composed of a computer controlled stimulus, a light microscope (Zeiss, Axioplan), a scientific grade CCD camera (Photometrics, #200 series with a Thompson 7883 CCD, Tucson, AZ), and a strobe light (model #8440 Chadwick and Helmuth, CA) or high intensity LED (1 candela diffused red LED with 60° viewing angle, #CMD53SRD/G, Chicago Miniature Lamp, IL).

The computer generates two voltage signals; one is sent to the magnet via the current amplifier and a second signal is sent to a strobed light source. The motions of the bead which are typically 10 to 100Hz, are too fast to visualize in real time. Thus, the strobe light or LED is used to illuminate the specimen at specific phases in the stimulus waveform. The average brightness of an image can be increased by using more than one strobe flash at each phase. The process is depicted in Figure 2-14. Strobe illuminated images of the TM and magnetizable bead are magnified by the light microscope and projected onto the CCD camera. The result is a stop-action sequence of images which can be used to recreate the motions and make quantitative estimates of displacements.

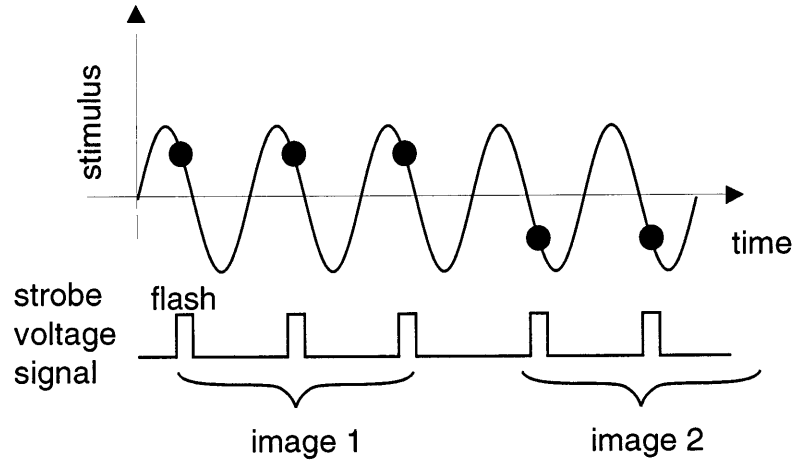


Figure 2-14: Strobe illuminated images. The computer generates a stimulus waveform for the magnets and strobe flashes which occur at specific phases in the stimulus. As illustrated, several strobe flashes can be used to illuminate each image.

2.6.2 Motion analysis

A gradient based method is used to estimate motions of regions in the sequence of strobe illuminated images (Davis, 1997; Davis, 1991). Each image is an array of integer values representing the brightness of light collected by each camera pixel during the illumination. The gradient based method relies on contrast or variations in brightness in the image to track motion. A magnetizable bead is opaque and provides a high contrast target. Spatial gradients ($\Delta E/\Delta x$) are determined by comparing the brightnesses of nearby pixels within an image (Figure 2-15). Temporal gradients ($\Delta E/\Delta t$) are determined by comparing brightnesses of corresponding pixels in successive images. The ratio of temporal to spatial gradients provides an estimate of velocity

$$\frac{\frac{\Delta E}{\Delta t}}{\frac{\Delta E}{\Delta x}} = \frac{\Delta x}{\Delta t} \approx \frac{\partial x}{\partial t}$$

which is combined across pixels in a least squares fashion.

Displacement estimates between successive images are used to generate a displacement waveform for an object. Fourier analysis of the waveform provides magnitude and phase information for the fundamental frequency and higher harmonics. Figure 2-16 shows results for a typical analysis of an 8 image sequence. In addition, the magnitude of the harmonics can be used to calculate a measure of the total har-

monic distortion (THD) for the sequence. The THD is a quantitative measure of how well the displacement waveform is represented by a pure sinusoid or how much the waveform is affected by disturbances such as magnet saturation. The THD is defined by

$$\frac{M_2^2 + M_3^2 + M_4^2}{M_1^2}$$

where M_i is the magnitude of the i th harmonic. In the example in Figure 2-16, the THD for y motion is approximately 0.003. The displacement is represented well by a sinusoid.

An important advantage of image based motion measurement over motion measurements used in previous bead methods is that each sequence contains information about the motion of every location in the field of view. Thus, the displacements of the bead and deformations of the surrounding tissue can be tracked simultaneously.

2.7 Implementing the magnetic bead method

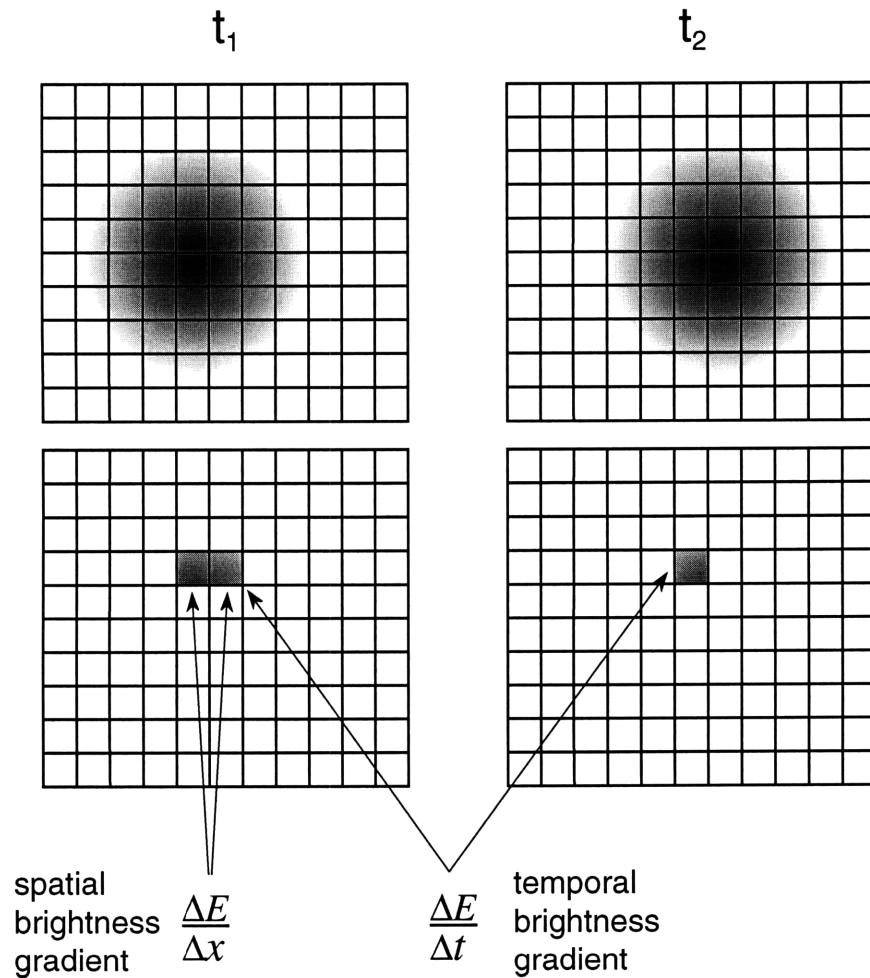
Several pieces of hardware were designed and constructed to allow positioning of the bead and TM in the fringe field of the magnets and simultaneously in the light path of the microscope.

A chamber was constructed to bath the TM and bead in an endolymph-like saline solution in an attempt to provide an appropriate ionic environment for the tissue (Shah et al., 1995). The chamber is a glass bottomed cylinder with an outside diameter of 5 mm and inner diameter of 3 mm (F.J. Gray and Co., Jamaica, NY). The chamber has a thin plastic (Delrin) collar at the top. The size of the chamber was made as small as possible but which still allowed the investigator to manipulate the TM and place a magnetizable bead on its surface. As a result, the distance from the bead to the magnet was determined by the chamber radius. For the 5 mm glass cylinder, the distance to the magnet is 3 mm. As seen in Figure 2-7, the force on a bead under these conditions is relatively insensitive to gap width. Thus, the gap width was set at approximately 5 mm and the chamber is positioned as close as possible.

To position the chamber relative to the magnets and the microscope, it rests on

an aluminum bridge. The chamber and bridge are illustrated in Figure 2-17. The bridge is screwed to an aluminum plate which allows adjustment of its position. The magnets are similarly fixed to an aluminum frame. As a result, both the magnets and the bridge can be adjusted independently. The mounting of the bridge and magnets fit together as shown in Figure 2-18. The three piece stage is attached to a computer-controlled stage on the microscope which provides positioning of the specimen along the optical axis of the microscope with $1/11 \mu\text{m}$ steps.

The hardware and concepts developed in this chapter provide essential foundation information for calibrating the forces produced by a magnetizable bead.



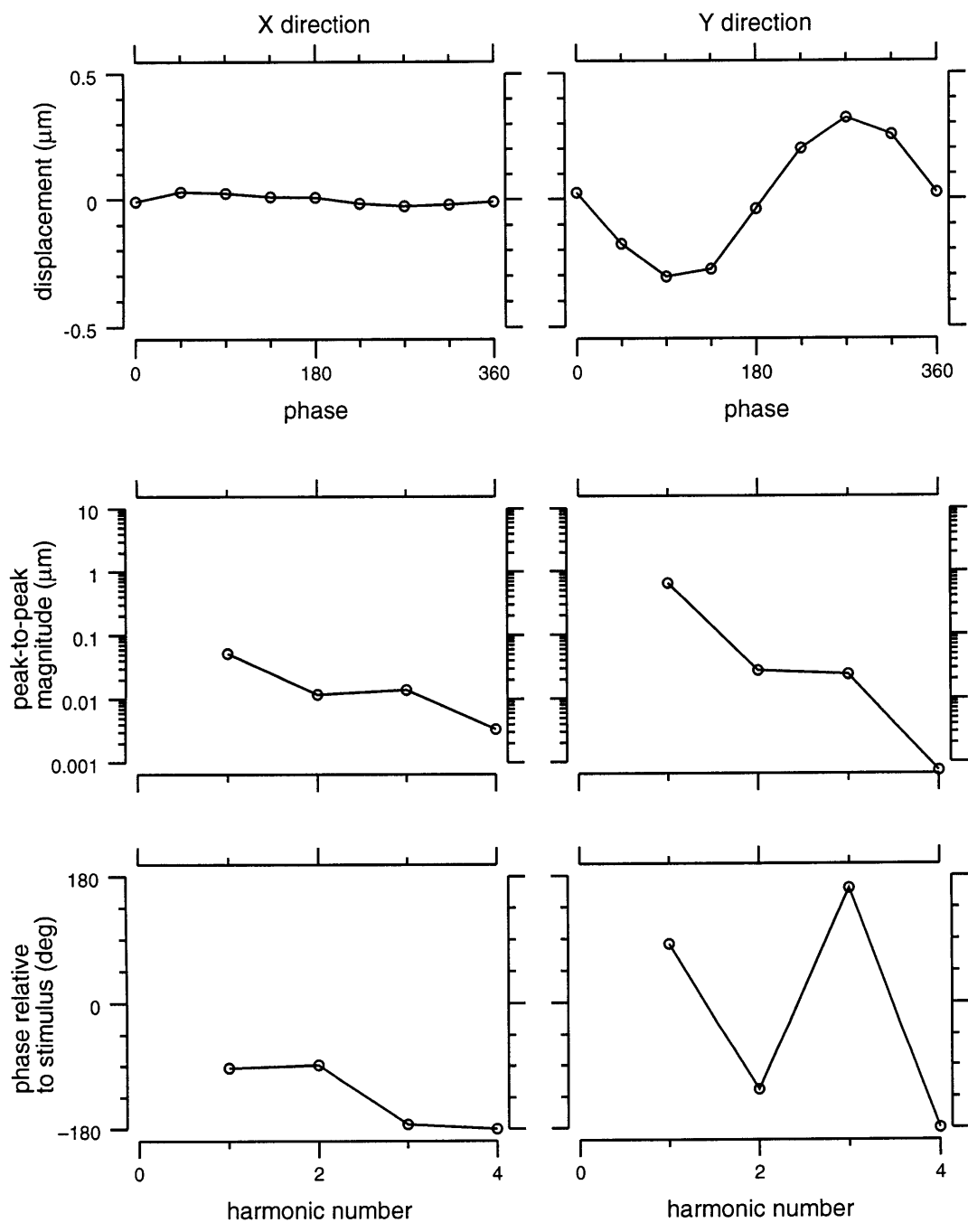


Figure 2-16: Measured displacement waveform and frequency analysis. Displacement waveforms (top panels) and Fourier components (bottom 4 panels), in both the x direction (left column) and y direction (right column), are determined for a sequence of 8 images. In this case, the largest displacements are in the y direction. The phase axis in the top panels indicates the phase of the displacement with respect to a full period of motion. The harmonic numbers indicate frequency components of 1, 2, 3, and 4 times the fundamental frequency.

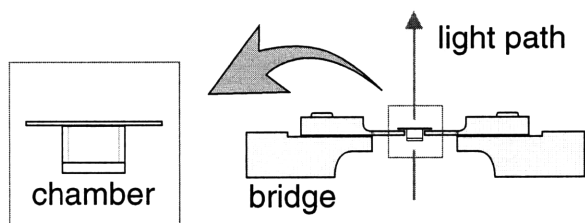


Figure 2-17: The TM chamber and bridge support. The left illustration shows, in cross-section, the cylindrical glass chamber used to isolate the TM. The chamber has an outer diameter of 5 mm. The top ring is made from Delrin and is used to support the chamber on the bridges shown in the illustration on the right. The bridges position the chamber between the magnets and in the light path of the microscope.

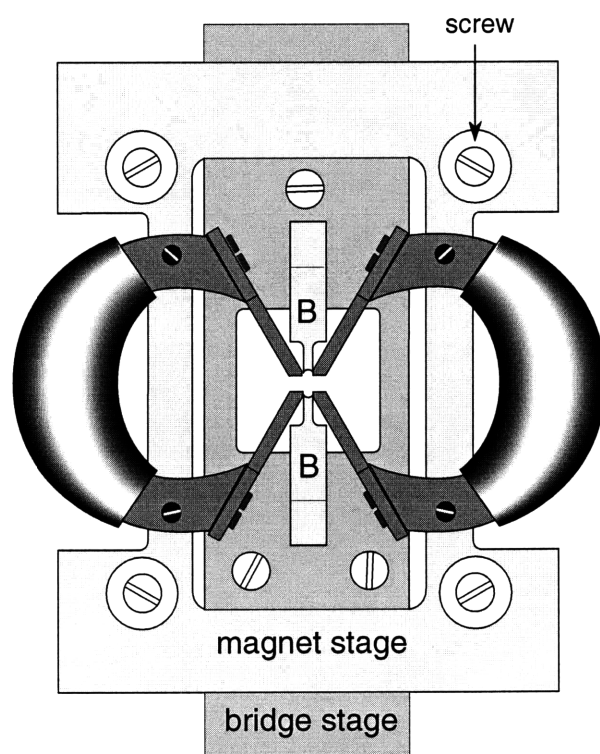


Figure 2-18: Top view of hardware for positioning chamber and magnets. The ring magnets are mounted on an aluminum stage (magnet stage) which can be positioned independent of other hardware. The TM chamber is positioned on the bridges as in Figure 2-17. The bridges are mounted to the bridge stage which can also be positioned independently. The positions of the magnet stage and bridge stage can be locked into place using screws.

Chapter 3

Calibration and Performance of Magnetic Bead Method

The displacements and stiffnesses of hair bundles suggest that interactions between the TM and hair bundles may involve forces, on the order of piconewtons ($0.001 \mu\text{N}$), and displacements, ranging from picometers to micrometers, that occur at frequencies from 10 Hz to 20 kHz. Determining whether the magnetic bead method can perform at these levels is critical. The performance of the magnetic bead method will be characterized by the range of forces that can be produced with the magnetizable beads and the range of motions that can be measured using the computer vision algorithms. This chapter discusses the measurements conducted to determine these characteristics.

3.1 Magnetic bead method: Range of forces

Two methods were developed to determine the forces on a bead: one method is based on measuring the velocity of a bead in a fluid and the other method looks at deflections of a bead attached to a cantilever.

3.1.1 Force calibration using Stokes' Law

Method. When a force is applied to a sphere or bead in a fluid, the resulting motion of the bead generates forces of fluid origin which act to resist the bead's motion. When the bead is traveling at a constant velocity, the fluid forces are in balance with the applied force. Thus, if the fluid force can be determined, the applied force can be calibrated.

For a bead moving in a Newtonian fluid of infinite extent, the fluid forces have been well characterized. In general, the solution contains contributions to the fluid force from both the viscosity and the inertia of the fluid (Yih, 1979). The Reynold's number defined as

$$Re = \frac{\rho U r}{\mu}$$

compares the relative importance of contributions from viscosity and inertia, where ρ is fluid density, μ is the fluid viscosity, U is the bead velocity, and r is the bead radius. When the Reynold's number is much less than 1, which would be the case for small beads, low velocity, and high viscosity, the fluid force can be written as

$$F = 6\pi\mu rU. \tag{3.1}$$

Equation 3.1 is known as Stokes' Law and can be utilized to calibrate applied magnetic forces on a magnetizable bead. Using a fluid with known viscosity and density, a measurement of a bead's velocity provides an estimate of the applied force.

A force calibration using Stoke's Law involves placing a single magnetizable bead in a small cylindrical, glass chamber filled with a fluid. The fluid is a silicon oil with a viscosity of 90.1×10^3 (mPa · s) and a density of 0.9 g/ml (#S30000, Cannon Instrument Co., State College, PA). The bead is 6% SiFe with a typical radius of 10 μm . The ring magnets are positioned relative to the microscope objective so that objects centered in the field of view are necessarily centered between the magnets. The calibration chamber containing the fluid and bead is placed on the bridge between the magnets and the bead is positioned so that it is centered in the field of view. A

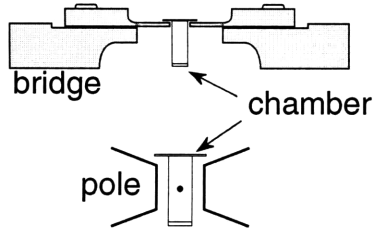


Figure 3-1: Chamber and bead position used for fluid calibration. The cylindrical glass chamber has an outer diameter of 5 mm and a length of approximately 6 mm. The chamber is held between the magnets with the aluminum bridge (top illustration). The bead (small dot in lower illustration, magnified) is positioned in the vertical center of the magnet poles.

glass cover slip is placed on the top of the chamber to allow viewing of the bead using a dry objective (Zeiss Axioplan 10x objective, total magnification at the CCD camera, 100x). The position of the chamber relative to the magnet poles is shown in Figure 3-1. The chamber extends vertically approximately 6 mm (about 3 times the length of the TM chamber) which allows the bead to be placed in the vertical center of the magnets.

During each calibration measurement, a DC current is applied to one ring magnet. The current is ramped from zero to the desired level so that the bead reaches a constant velocity smoothly. Several strobe illuminated images of the bead's motion are acquired. The images are evenly spaced in time. The bead is returned to the initial position by applying forces with the opposite magnet. After each measurement, gradient based, computer vision algorithms are used to estimate the displacement from the images which when combined with the temporal spacing between images, provides an estimate of the bead velocity. Stokes' Law is used to estimate the applied force using the velocity estimate. The calibration is repeated for a range of DC current levels to establish a relationship between the applied current and the resulting magnetic force.

Results. The results for a $10 \mu\text{m}$ radius bead are shown in Figure 3-2. The form of Equation 2.7 suggests that the force on the magnetizable bead should be proportional to the square of the magnet coil current. The plot in Figure 3-2 shows that for current levels up to about 2.7 amps, the applied force is indeed proportional to the square of the current. However, as seen in Figure 2-8, above 2.7 amps, the iron cores of the magnet saturate. This is consistent with the slope change in Figure 3-1. The magnitude of the magnet force near saturation is on the order of $0.08 \mu\text{N}$.

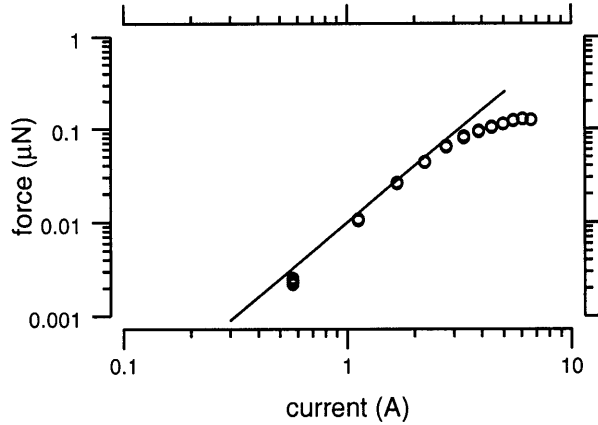


Figure 3-2: Fluid force calibration. The force estimate calculated using Stokes' Law is plotted versus the applied DC coil current. Each symbol represents an independent force estimate based on a velocity calculated from two successive images. There are 4 to 6 force estimates plotted at each current. The solid line indicates a slope of 2.

Discussion. Situations in which it is appropriate to use Stokes' Law for force calibration depend on the Reynold's number and the influence of the nearby chamber walls. For the 10 μm bead moving in silicon oil, the Reynold's number is on the order of 10^{-10} which is well within the regime of motions dominated by viscous forces.

Because the dimensions of the chamber are finite, a moving bead will be affected by its proximity to nearby structures. Near the chamber wall a bead will experience a greater drag force than when moving in an infinite fluid. The effect of the wall can be approximated by a correction to Stokes' Law of the form (Happel and Brenner, 1973)

$$F_s = 6\pi\mu rU\lambda \quad (3.2)$$

where λ is a correction coefficient that depends on the radius of the bead r and its distance from the chamber wall h . The largest values of λ occur for a bead traveling perpendicular to a plane wall. In this case, λ can be written as

$$\lambda = \frac{1}{1 - (9/8)(a/h) + 1/2(a/h)^3}. \quad (3.3)$$

The chambers used in the calibrations have an inner diameter on the order of 3 mm and the beads typically have radii which range from 6 to 18 μm .

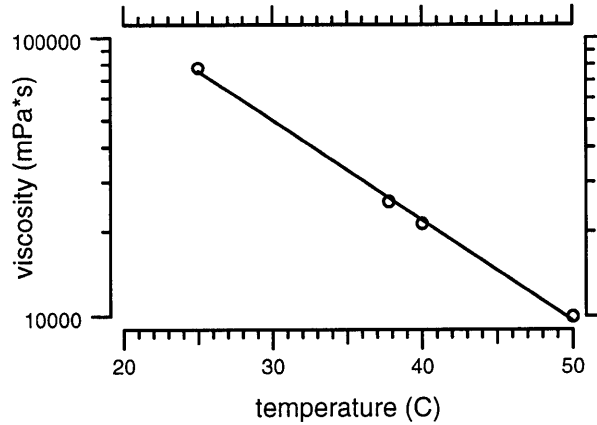


Figure 3-3: Viscosity of silicon oil as a function of temperature. Each symbol represents a viscosity measurement at a specific temperature according to data supplied by the manufacturer of the silicon oil. The line represents a least squares fit through the data.

r/h	λ
1/50	1.023
1/20	1.06
1/10	1.13

The results for several ratios r/h are summarized in the table. Considerable effort is made to center the bead in the chamber which corresponds to a ratio $r/h = 6.7 \times 10^{-3}$ or less than a 1% increase in the drag force of Stokes' Law. Thus, wall effects are not significant. It turns out, Stokes's Law is more sensitive in this case to changes in the viscosity of the oil resulting from changes in temperature.

The viscosity of the silicon oil is a strong function of temperature. The plot in Figure 3-3 shows the measured viscosity plotted versus temperature (data supplied by manufacturer). The line represents a least squares fit to the data and provides an equation

$$\log \mu = -0.0357T + 5.77$$

which relates the viscosity μ (mPa · s) to the temperature T (C). A variation of $\pm 1^\circ$ C can change the viscosity, and therefore the estimated force, by about 10%. During the calibrations, the room temperature was within one degree of 22° C.

Conclusion. Although the fluid force estimates provide accurate estimates of magnetic force, the fluid calibration is inconvenient for several reasons. The magnetic bead method is intended to produce oscillatory motions. Unfortunately, stable oscillations are not possible in the fluid because the force increases monotonically toward the gap. Consider a bead which is perfectly centered between two ring magnets (A and B). At this location, magnet A and magnet B will pull on the bead with equal force. However, during the first half period of an oscillation the bead moves away from the center by a distance, say ϵ , and closer to magnet A. This increases the force on the bead from magnet A. During the second half period, magnet B pulls the bead but a distance less than ϵ . Thus, at the end of a complete period the bead is closer to magnet A. This process repeats as oscillations continue and the bead ends up closer and closer to magnet A. In addition, gravity pulls the bead to the chamber bottom and tends to make vertical positioning troublesome. As a result, repeated measurements with a single bead at a single location or at specific vertical positions are difficult. Furthermore, calibration of an individual bead for use in a TM experiment is not possible because the silicon oil is not soluble in any commonly available liquid. In order to address some of these issues, a second calibration method was developed.

3.1.2 Force calibration using a micro-fabricated cantilever

Method. The magnetic force on a bead was calibrated using a micro-fabricated silicon cantilever (Park Scientific Instruments, single crystal silicon, Sunnyvale, CA) similar to those used in atomic force microscopy (AFM). The cantilever is a single crystal silicon beam with rectangular cross-section having a width of $30\ \mu\text{m}$, a length of $397\ \mu\text{m}$, and a thickness of $2\ \mu\text{m}$.

When using the cantilever for calibration of the magnetic bead method, a magnetizable bead is attached to the tip of the cantilever using an instant adhesive (Loc-tite #403). A very small amount of glue is used because large amounts may affect the cantilever stiffness. The bead and adhesive can be easily removed, with no residue, using a debonding agent (cyanoacrylic debonder, Saf-T-Lok Chemical Corp., Lom-

bard, IL). The glue and debonding procedure allows easy, repeatable measurements with any bead. In addition, a bead can be calibrated and subsequently used in a TM experiment.

When a force f is applied to the cantilever tip, the tip is deflected or displaced a distance d . Using an estimate of the cantilever stiffness k , the magnitude of the force can be determined from Hooke's Law

$$F = kd$$

provided the deflection is not too large, and the force can be expressed as a linear function of the deflection.

Determining cantilever stiffness. The stiffness of the cantilever is determined prior to force calibration with a magnetizable bead. Because the cantilever is single crystal, its composition is very homogeneous, its mechanical properties are well known, and its stiffness can be estimated from a constitutive equation (Tortonesi and Kirk, 1997; Tortonesi, 1997). The stiffness of rectangular cantilever can be expressed as

$$k = Et^3w/4l^3 \tag{3.4}$$

where E is the modulus of elasticity of crystalline silicon and is 3.15×10^3 Pa, t is the thickness, w is the width, and l is the length of cantilever (Tortonesi and Kirk, 1997). The stiffness can be checked by measuring the resonant frequency of the cantilever. A continuous beam has multiple resonances associated with multiple modes of vibration. However, the stiffness can be written in terms of the first resonant frequency as

$$k = 1.543\sqrt{\rho E}wl^3 F_r^3 \tag{3.5}$$

where ρ is the density equal to 2.3×10^3 kg/m³ and F_r is the resonant frequency. Equations 3.4 and 3.5 predict a resonant frequency at 17.67 kHz in vacuum (Tortonesi and Kirk, 1997). Oscillations in air change the resonant frequency slightly due to

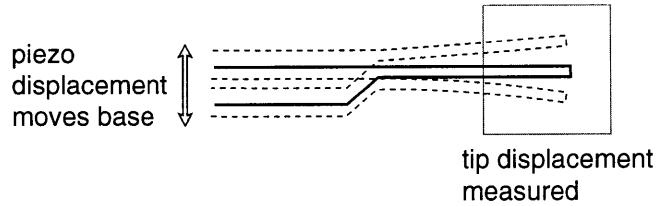


Figure 3-4: Calibration of the cantilever stiffness. The cantilever stiffness is estimated by determining the frequency of the first resonant mode of vibration. The base of the cantilever is sinusoidally displaced using a piezo stack and the displacement of the tip is observed using strobe illumination. The box represents the region analyzed by computer vision algorithms.

damping.

In order to empirically determine the resonant frequency, the base of the cantilever was mounted to the end of a piezoelectric stack (Thorlabs Inc., #50512). A sinusoidal voltage stimulus was applied to the piezo stack producing a sinusoidal displacement of the cantilever base and tip as shown in Figure 3-4. The first resonant frequency was determined visually by observing motion of the cantilever tip through the microscope. The amplitude of the tip motion could be viewed using stroboscopic illumination to slow the apparent motion. Tip displacements were measured at several frequencies nearby the estimated resonance. The plot in Figure 3-5 shows the measured displacement amplitude versus frequency. The first resonant peak occurs near 17.8 kHz which compares well to the resonant frequency estimated from constitutive relations. According to Equation 3.5, the measured resonant frequency corresponds to a cantilever stiffness of 0.157 N/m.

Results: Amplitude dependence of magnetic force on a 18 μm radius bead.

A large, 18 μm radius, 6% SiFe bead was fixed to the tip of the cantilever. The cantilever was positioned relative to the magnets using a 3 axis micromanipulator. The displacements of the cantilever tip and bead were measured, as shown in Figure 3-6. Based on the displacements, an estimate of the applied force was obtained using Hooke's Law. Displacements associated with a range of DC currents and AC current amplitudes (at 10 Hz) were measured. In addition, bead displacement waveforms for current stimulus frequencies up to 1000 Hz and peak amplitude of 1.4 amps were

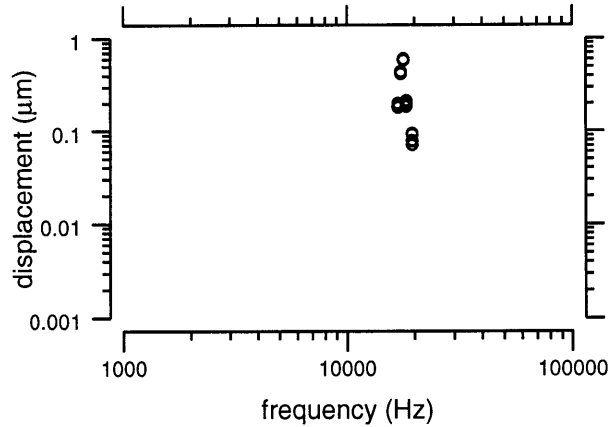


Figure 3-5: Resonant frequency of a silicon cantilever. The displacement of the cantilever tip is plotted for a range of frequencies around the observed resonance, from 15 Hz to 20 kHz. Each symbol is an independent displacement measurement based on 8 images taken at specific phases in the voltage stimulus applied across the piezostack. The resonant peak for the first mode of vibration is near 17.8 kHz.

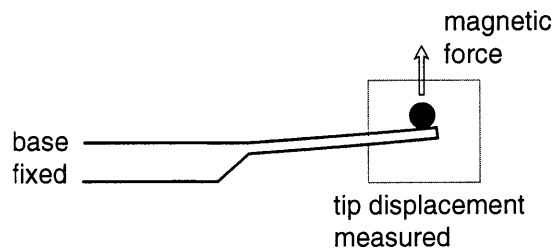


Figure 3-6: Calibration of the magnetic force using cantilever. The applied magnetic force is estimated by determining the displacement of the bead and cantilever tip for a range of AC and DC current stimuli applied to the magnet coil. The box represents the region analyzed by computer vision algorithms. DC deflections were always in the direction depicted by the arrow. The displacement of the bead and tip is observed using strobe illumination.

analyzed. Bead displacements for DC currents were estimated using two strobe illuminated images: one image with current and one image without current. For AC currents, a sequence of strobe illuminated images were used to reconstruct the displacement waveform.

The plot in Figure 3-7 shows the measured force for a range of DC current magnitudes and AC peak magnitudes. The solid lines show the distinct slope difference for low and high currents consistent with saturation of the iron core. As in Figure 2-8, the saturation occurs near 2.7 amps. For currents up to 2.7 amps, the force is proportional to the square of the current. Estimated forces for AC current stimuli at 10Hz are consistent with the corresponding DC measurements at similar current

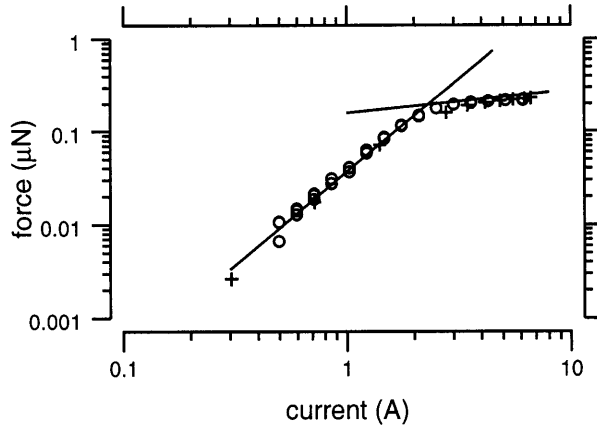


Figure 3-7: Measured force as a function of coil current. Displacements of a $18 \mu\text{m}$ radius 6%SiFe bead, glued to the tip of the silicon cantilever, were measured for a range of AC and DC currents. The circles represent the DC force measurements and the + symbols represent the peak magnitude of the fundamental AC frequency.

levels. The force for a $18 \mu\text{m}$ bead near core saturation is on the order of $0.1 \mu\text{N}$.

A consequence of core saturation can be seen in measured displacement waveforms. Fourier analysis of displacements associated with current stimuli having peak amplitudes above (saturated) and below (not saturated) 2.7 amps are compared in Figure 3-8. The saturated waveform shows distinct distortion. As a result, the magnitude of the third and fourth harmonics are much larger relative to the fundamental frequency than in the case where the waveform is not saturated. The THD is more than an order of magnitude larger for the saturated waveform. The THD values for a range of peak current amplitudes are plotted in Figure 3-9. For amplitudes above 1.4 amps, the THD in this case increases steadily from 0.003 to 0.07.

Results: Frequency dependence of magnetic force on an $18 \mu\text{m}$ radius bead.

In addition to measurements characterizing the amplitude dependence of magnetic forces, a 1.4 amp peak current was applied to the coil at frequencies from 10 to 1000 Hz using the controlled current mode. The resulting peak bead displacements were estimated from measured displacement waveforms and are shown in Figure 3-10. The magnitude of the force changes by 20% from 10 to 100 Hz. Above 300 Hz, the amplitude falls off rapidly.

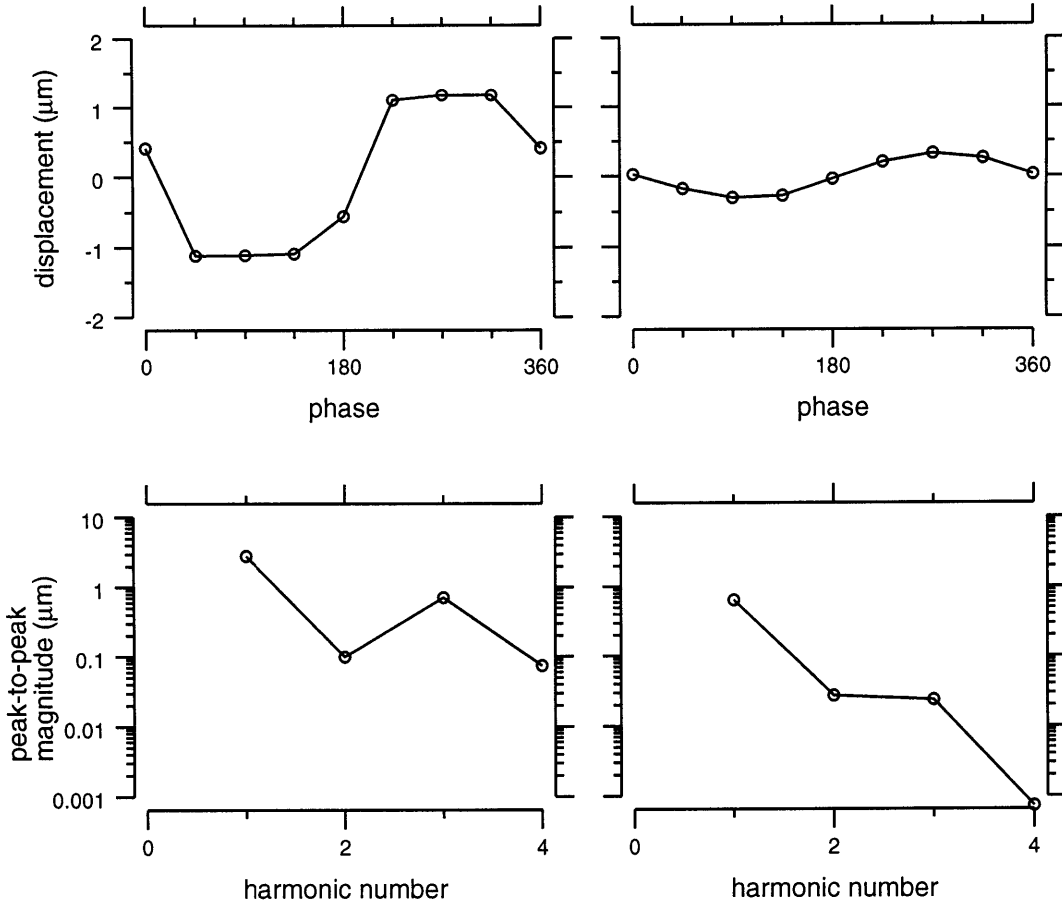


Figure 3-8: Cantilever displacement waveforms and harmonics. The displacement waveform for a 6 amp, 10Hz coil current is shown on the top left. This waveform has considerable distortion. A waveform with much less distortion is shown on the right for a 1.4 amp, 10Hz coil current. The peak to peak amplitudes of the component frequencies are plotted in the lower two panels. The harmonic number indicates frequencies of 1, 2, 3, and 4 times the fundamental frequency.

Results: Spatial dependence of magnetic force on an 18 μm radius bead.

The spatial variation of the \mathbf{B} field was measured with a hall effect probe having a spatial resolution on the order of 1 mm. However, the bead and tectorial membrane have characteristic dimensions on the order of micrometers. Spatial variations in the force over dimensions of several microns could be important. For this reason, the cantilever and bead were used to directly probe the force in the fringe field. The bead was positioned in the fringe field with a micromanipulator. A micromanipulator was used to position the bead in the fringe field. Measurements were taken in 50 μm steps along the three orthogonal directions x , y , and z centered at the location typically

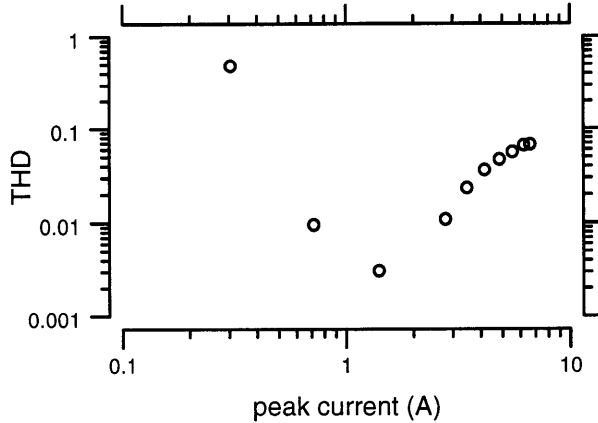


Figure 3-9: Total harmonic distortion (THD) as a function of current amplitude. Displacement waveforms for current amplitudes from 0.3 to 6.6 amps were used to calculate the THD. Each symbol represents an independent THD measurement for displacements of a $18 \mu\text{m}$ bead attached to a silicon cantilever. In this case, the waveform with the minimum distortion occurs at a current amplitude of 1.4 amps. Displacements associated with the large THD at 0.3 A were too small to resolve reliably.

occupied by the TM chamber. The force was measured for a range of DC currents from 0.4 to 6.6 amps. The plots in Figure 3-11 show the force for a 2 amp current measured along the x, y , and z axes. Consistent with the Karlquist analysis, the force increases near the magnet and falls off as the distance from the magnet increases. According to Figure 3-11, the force varied by approximately 10% over a distance of $100 \mu\text{m}$.

Discussion. The results of measurements of magnetic force as a function of current stimulus amplitude, stimulus frequency, and bead location provide important information.

The cantilever measurements depend on Hooke's law to provide a force estimate. The measurements in Figure 3-7 show that the estimated force on the bead is proportional to the square of the current for current stimuli below 2.7 amps. The result is consistent with and proportional to the fluid calibration in Figure 3-2. Since the force is a linear function of fluid viscosity, this implies that the force is also a linear function of the cantilever stiffness. This suggests that the measured displacements are within the linear range of the cantilever. The largest measured tip deflections are on the order of $1 \mu\text{m}$, which is about half the thickness of the $397 \mu\text{m}$ long cantilever.

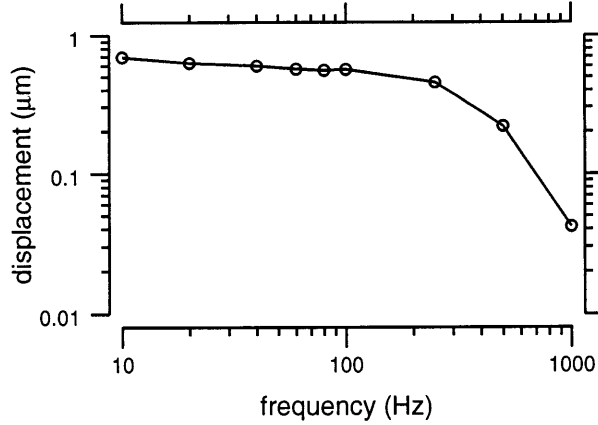


Figure 3-10: Frequency dependence of measured peak cantilever displacement. Peak displacements of a 18 μm radius 6%SiFe bead, glued to the tip of the silicon cantilever, were measured for a 1.4 amp peak current amplitude at several frequencies from 10 to 100 Hz. The circles represent 8 independent measurements at each frequency.

As a result of the frequency measurements, only frequencies up to 100 Hz are used in TM experiments. However, the plot in Figure 3-7 indicates that the peak amplitude at 10 Hz can be increased from 0.05 μN at 1.4 amps to about 0.1 μN before saturation at 2.7 amps. This implies that current amplitudes at frequencies larger than 100 Hz could be increased to maintain a constant force amplitude across frequencies. Thus, there is the possibility of compensating for the attenuation shown in Figure 3-10 and thereby increasing the usable range of frequencies. The frequency range over which the amplitude can be compensated depends on the lowest current amplitude which will produce measurable motions in a particular experiment.

The TM and bead can be positioned between the magnets to within several bead diameters or about 50 to 100 μm in any direction. The spatial variation in the force is small over a region of this size. Thus, differences in TM and bead position are not likely to contribute to measurement variations in TM experiments.

3.1.3 General calibration relation

Apart from determining the variation of magnetic forces with stimulus conditions and position, the cantilever calibration procedure was used to evaluate the affect of bead size on the production of force. The 6% SiFe beads are graded in size by

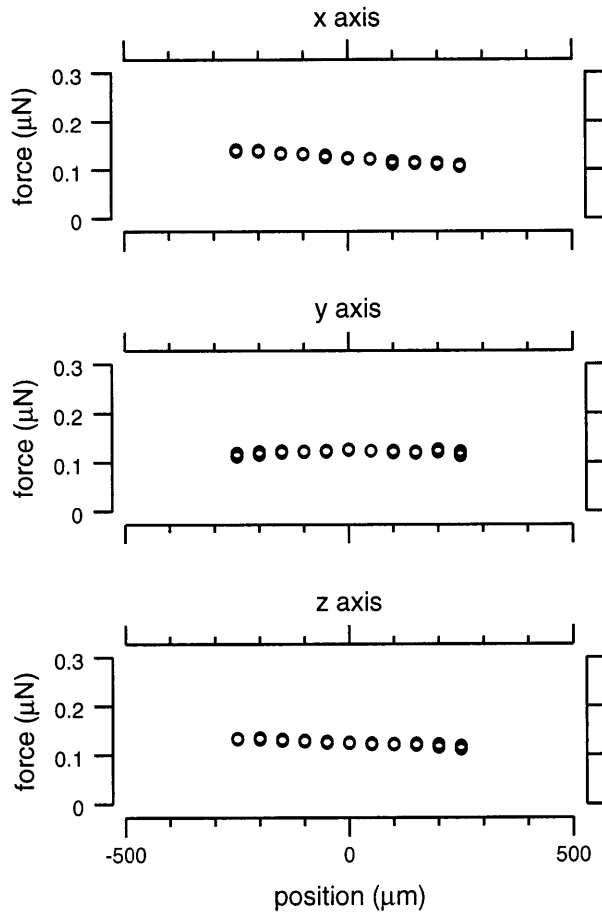


Figure 3-11: The variation of measured cantilever displacement with position. The cantilever displacement measured at locations along the x , y , and z axes is shown in the top, middle and bottom plots respectively. The origin of the axis is at the location typically occupied by the TM chamber. Each symbol represents an independent displacement estimate.

the manufacturer but in general can have radii that vary by a factor of 2 or more. Equation 2.7 suggests the force is proportional to the volume (r^3) of bead material. Thus, each bead will produce a different range of force amplitudes.

To account for the variation in force, an individual bead can be calibrated prior to a TM experiment in which it is used. Alternatively, a general calibration relation can be determined. In this case, a single relation between bead size, coil current, and magnetic force is determined. For each TM experiment, the bead size is measured from video images, the coil current is monitored, and the general calibration provides an estimate of the generated magnetic force.

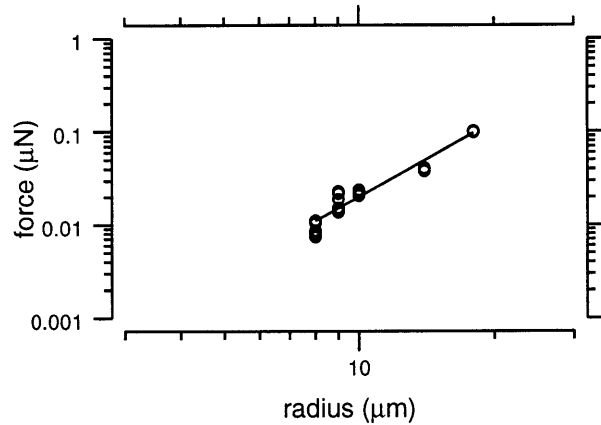


Figure 3-12: Variation of force with bead size. The measured force for a 2 amp DC current was measured. The solid line is a least squares fit through the data and has a slope of 2.8. Each symbol represents an independent force estimate based on two images. There are 8 to 10 estimates for each bead size.

Method. Forces associated with six 6%SiFe beads with radii from 6 to 18 μm were measured. A bead was glued to the cantilever tip and bead displacements for DC currents from 0.5 amps to 6.6 amps were measured. The bead was debonded and the cantilever stiffness was checked to insure the glue or possible glue residue didn't affect the measurements. The process was repeated with each of the six beads. Each bead was positioned in the same location relative to the magnets.

Results. The measured force for a 2 amp DC coil current is plotted in Figure 3-12 versus bead radius. The solid line is a least squares fit to the data with a slope of 2.8. This indicates the force is proportional to $r^{2.8}$ where r is bead radius. It is important to note that the plotted forces correspond to a current below core saturation. The plots in Figure 3-13 compare the measured displacements for an 18 μm and 15 μm (big beads) and two 10 μm beads (little beads) over the range of DC currents from 0.5 to 6.6 amps. Each plot was made by pairing the displacements of two beads at the same DC current level. The solid line represents a slope of 1. Two beads which produce a range of displacements that have identical shapes (but may be scaled versions of one another) should produce a slope of 1 when paired together. When a big bead is plotted versus a big bead (left plot) or a little bead is plotted versus a little bead (middle plot) the paired displacements fall along a slope of 1. However, when a big

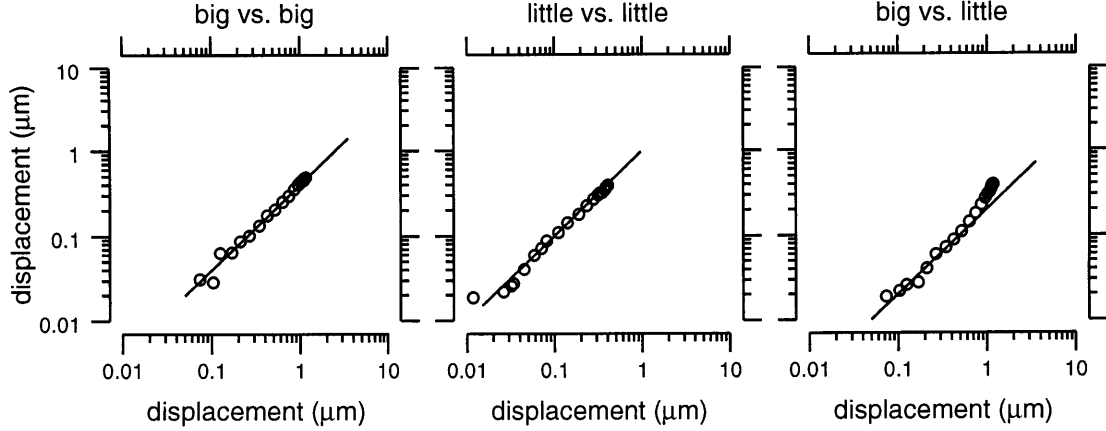


Figure 3-13: Comparison of measured displacements for big and little beads. The displacements for a 18 μm and 15 μm bead are paired at each DC current level and plotted on the left. Similarly, displacements for two 10 μm beads are presented in the middle plot. The plot on the right pairs displacements from an 18 μm bead and a 10 μm bead. The solid line in each plot has a slope of 1. The displacements paired from a big and little bead (right plot) deviate considerably from a slope of 1.

bead is paired with a little bead, the result deviates considerably from a slope of 1, particularly for high current levels. There appears to be a distinct difference between the behavior of the little beads ($\leq 10 \mu\text{m}$ radius) and big beads ($> 10 \mu\text{m}$ radius) at current levels above saturation.

Discussion. A general calibration relation defines a basic relation between the magnetic force f and the coil current I which is scaled by the bead radius r to provide a force estimate for a specific bead. Due to the saturation of the magnet core there is a distinct low current (< 2.7 amps) and high current (> 2.7 amps) regime.

For each bead, a line was fit to the low current data and a second line was fit to the high current data. The average slope, across all beads, for low currents was 1.97 which again is consistent with Equation 2.7. For high currents, the average slope was 0.22. These slopes were combined to generate a general calibration relation in each regime. The magnetic force for low and high currents can be estimated from

$$f = C_l I^{1.98} r^{2.8} \quad (3.6)$$

and

$$f = C_h I^{0.22} r^{2.8} \quad (3.7)$$

respectively. The coefficients C_l equal to 1.75×10^{-5} and C_h equal to 8.8×10^{-5} are constants determined from the fits. The predicted forces from Equations 3.6 and 3.7 are plotted (gray curves) in Figure 3-14 with the forces measured using the cantilever. The calibration relations do not seem to characterize the 8 μm and 14 μm bead well. The origin of the differences between little and big beads is not known. It is possible that the beads are not homogeneous but contain voids which reduce the measured force. The calibration expression in Equation 3.6 was used in TM experiments.

3.2 Magnetic bead method: Range of measurable motions

The performance of the system was measured by a method shown in the left illustration of Figure 3-15. A microscopic target (titanium dioxide sphere 0.3 μm) was mounted to a glass slide. The slide was attached to a piezostack which produced translations of the slide parallel to the focal plane. The translation measurements were obtained using a fiber optic probe (also used in Figure 2-6) and were compared to estimates using computer vision algorithms. Measurements were done by Davis (1997) which showed that the gradient based motion measurement algorithms can resolve motions of 0.01 pixels (about 5 nm at 100x magnification).

There are a number of factors which reduce the resolution of the motion measurements. In particular, mechanical vibrations produce unintended but measurable motions of the specimen. The laboratory environment has many sources of vibrations, ventilation and air conditioning systems, human activity, motor vehicles nearby, etc. In an attempt to reduce the influence of vibrations, the microscope is placed on a passive air vibration isolation table. The isolation table reduces the standard deviation of measurements by 10 dB (Davis, 1997). However, the table is not effective at reducing vibrations whose source is on the table or worse, on the microscope stage.

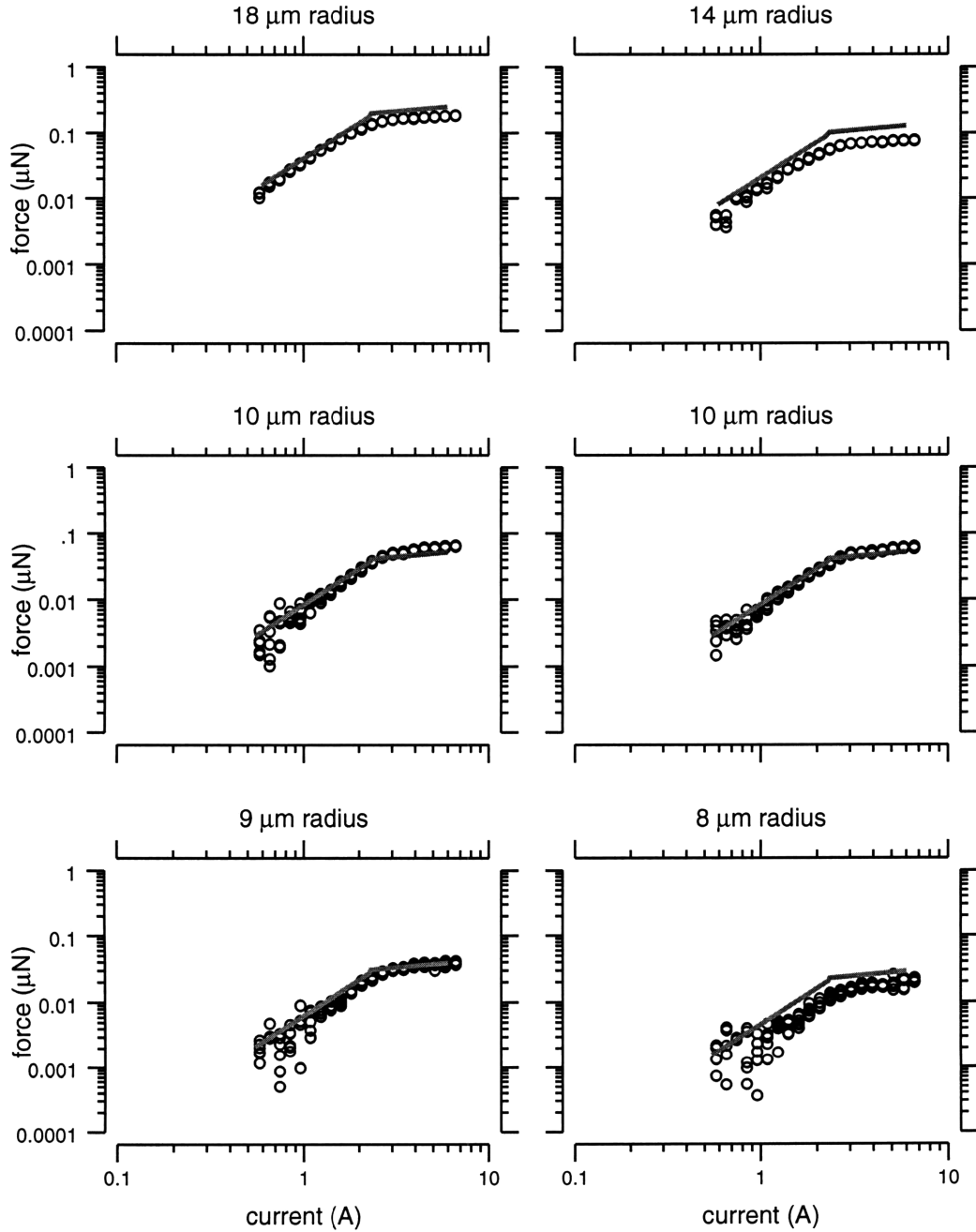


Figure 3-14: General calibration curve. A calibration curve (gray line) was fit for currents above and below core saturation. Forces predicted by the calibration are plotted with measured forces for six beads. The symbols represent force estimates associated with DC currents applied to the coil. There are 6 to 10 independent measurements at each current level for each bead. The largest discrepancy between the calibration curve and measured forces occurs for the 8 μm and the 14 μm radius beads.

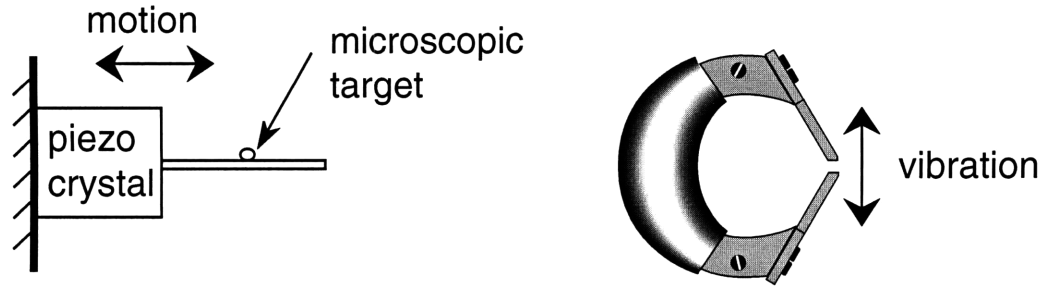


Figure 3-15: Smallest measurable motions. Using a piezo driven target, the motion measurement system was able to resolve motions on the order of 0.01 pixels (about 5 nm at 100x magnification). Vibrations of the ring magnet pole tips produced unintended motions on the order of 20 nm.

At high coil current amplitudes, the magnet pole tips pull toward one another which produces oscillations of the tips as depicted in the right illustration Figure 3-15. The bridge is intended to support the TM chamber without touching the magnet poles. Nevertheless, some mechanical vibrations will reach the chamber through other supporting structures. In addition, magnet vibration can produce relative motion between the stage and the objective which results in apparent motion in the images.

The effect of magnet vibration was measured. Current was applied to the magnets with a peak amplitude of 6 amps over several frequencies from 10Hz to 100Hz. Two vibration measurements were conducted. First, images of the magnet poles were acquired and analyzed to estimate displacements. The pole tips were found to undergo displacements on the order of $1\ \mu\text{m}$ (along both the x and y axes). Second, a glass chamber was prepared which had a number of $10\ \mu\text{m}$ radius, non-magnetic, polystyrene beads fixed to the bottom. The chamber was placed on the bridge between the magnets. As current stimuli were sent to the magnets, images of the polystyrene beads were acquired. The maximum displacement amplitudes of the beads and chamber were on the order of 20 nm in both the x and y directions. As a result, it is expected that bead and TM displacements which are on the order of 20 nm will be near the noise floor of the system and out of the range of measurable motions.

3.3 Conclusions

Calibration methods have shown the magnetic force to have little spatial variation over distances of many bead diameters. In addition, a relationship between currents below 2.7 amps and bead radius was found which allows prediction of the force produced by a bead. Measurements of the magnetic bead method's performance have defined the operating range available for TM experiments. The forces and measurable motions are within the range of forces and displacements which may occur between the TM and hair bundles in vivo. The magnetic bead method is able to produce forces from $0.001 \mu\text{N}$ to $0.1 \mu\text{N}$ at frequencies from 10 Hz to at least 100 Hz. Motions resulting from the applied forces as small as 20 nm can be measured.

Chapter 4

Preparation of the Tectorial Membrane

4.1 Isolating the TM

The tectorial membrane's used in the measurements are taken from white, male mice (strain: ICR, vendor: Taconic) typically 6-12 weeks old and weighing approximately 35 to 50 grams. The mouse is euthanized using CO₂ asphyxiation and decapitated. Under a dissecting microscope, the cochlea is dissected from the mouse and placed in a petri dish with artificial endolymph solution (AE) (Shah et al., 1995). The cochlea is very sensitive to the ionic environment and can undergo significant dimensional changes with changes in the composition of the bathing solution (Freeman et al., 1994; Shah et al., 1995; Kronester-Frei, 1978). Thus, the AE is intended to provide an ionic environment similar to the fluids in the scala media which bath the TM in vivo. Excess tissue and debris are removed from the cochlea. Using fine tweezers (#5, stainless steel, Dumont), the stapes and the stapedial artery are removed to provide access to the oval window. The membranes of the oval and round windows are removed. Several milliliters of AE are injected into the oval window with a syringe to flush out the fluid in the scala vestibuli and scala tympani and minimize exposure of the TM and the high sodium concentration in the perilymph. To remove the TM, the apical portion of the boney casing is gently chipped away with the tip of a scalpel

blade. Enough of the casing is removed so that the apical one and a half turns of the organ of Corti is visible but remains attached at the limbal edge. The organ is removed by grasping it at the most basal exposed point and slowly peeling it away from its attachment. At this point the TM can be seen using dark field illumination under the dissecting microscope. An eyelash glued to the tip of glass pipette is used to gently peel the TM away from the organ. This surgery provides a TM sample approximately 1 mm in length. The sample is gently cut into two or three sections.

The TM chamber is prepared about an hour before the surgery. The chamber is cleaned and 1.5 to 2 μ l of Cell-tak (Cellular Biomedical Inc., Waltham, MA), a tissue adhesive, is placed on the bottom of the chamber and allowed to dry in a location free of dust. After the TM sample has been removed from the organ of Corti, the chamber is filled with AE and placed in a modified petri dish which has a rectangle of plastic (holder) attached to the bottom with epoxy. The rectangle has a hole (7 mm diameter) drilled in the center. The chamber is placed in the hole which keeps it still during subsequent manipulations of the TM and the placement of the magnetizable bead. The petri dish is filled with AE to a depth which completely covers the chamber.

The TM is transferred to the chamber using a transparent glass pipette with a 1.5 mm inner diameter. The dissecting microscope allows the TM sample to be viewed when it is sucked up into the pipette during the transfer. The TM is expelled into the modified petri dish, near the chamber. Using an eyelash, the TM sample is gently floated into the chamber and down onto the Cell-tak. No attempt is made to control whether the covering net side of the TM face-up or face-down. The adhesion of the TM is checked by squirting AE into the chamber with a syringe. A firmly stuck TM will not move or fold at the edges when subjected to the stream of AE.

4.2 Preparing and placing magnetizable bead

Prior to surgery, a number of 6% SiFe beads are suspended in approximately 10 ml of ethanol. The bead suspension is forced through a nylon mesh which has square pores 12 μ m by 12 μ m. Thus, beads with diameters greater than 12 μ m are collected

on the nylon mesh. When the mesh and beads dry, several dozen beads can be scraped off the mesh with a fine tipped glass pipette onto a small strip of glass. Several 2 μl drops of Cell-tak are placed on top of the beads and the beads are stirred around in the adhesive using the tip of a fine pipette. The stirring helps to coat the beads and separates clusters of beads. The Cell-tak is allowed to dry during the surgery. In addition, a glass pipette is modified to produce an instrument for placing a bead on the TM surface. The pipette is pulled to produce a fine tip (1 μm diameter). Using a white hot platinum wire, the tip is bent at an angle (Hudspeth and Corey, 1978). The bend in the tip allows the placement of the bead as shown in Figure 4-1.

When the TM sample has been firmly attached to the chamber bottom, the coated beads are placed next to the chamber. A pipette mounted to a micromanipulator is used to select a single coated bead and place it on the TM. When the pipette tip touches a bead it sticks slightly and can be moved near the TM. Using the fine vertical control of the micromanipulator, the bead is gently lowered and pressed onto the surface of the TM sample. The attachment of the bead is checked using a stream of AE as was used to check TM attachment. At this point, a concentration of 2 μm diameter polystyrene beads can be injected into the chamber and allowed to settle onto the surface of the TM. The beads act as markers which help determine the orientation of the TM during measurements and can be used to track surface deformations of the tissue. The chamber is removed from the holder and placed on the bridge between the ring magnets.

4.3 TM deformation measurements

With the chamber, TM, and magnetizable bead positioned between the magnets, the orientation of the TM with respect to the magnets is adjusted so that the force applied by the bead is either parallel (radially directed) or orthogonal (longitudinally directed) with respect to the visible fibrillar structure.

Prior to measuring a TM force response, several pictures of the bead position and

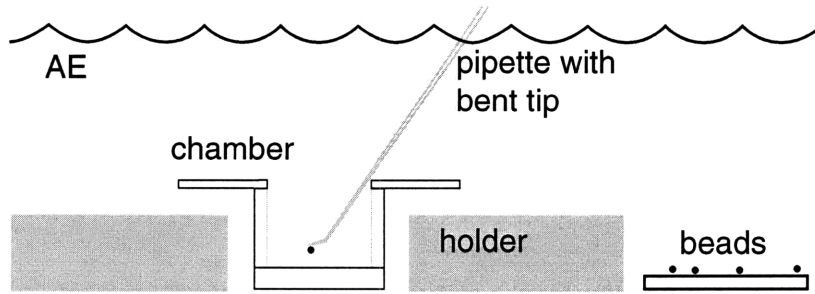


Figure 4-1: Placement of magnetizable bead on TM surface. A single magnetizable bead is manipulated using a glass pipette with a $1 \mu\text{m}$ diameter tip bent at an angle. The bead is selected from several adhesive coated beads placed near the chamber. Using a micromanipulator, the bead is positioned over the TM and then lowered onto the surface. The bead is pressed lightly into the surface to improve the adhesion. All manipulations are done submerged in artificial endolymph (AE) solution.

TM geometry are taken. Beginning at the surface of the chamber bottom, pictures are taken at 1 or $2 \mu\text{m}$ intervals spanning the entire thickness of the TM. This volume image allows accurate measurement of the TM thickness at the location of the magnetizable bead and allows us to determine which side of the TM (i.e. covering net side or opposite side) has been attached to the glass. Similar measurements are taken periodically during an experiment to track any morphological changes in the TM. In addition, several pictures are taken of the bead motion at 10 Hz as a visual check to see how the bead is attached and if the motion looks sinusoidal.

A typical experiment proceeds by taking measurements at various force magnitudes and frequencies then rotating the TM chamber relative to the magnetic force by 90° . A similar set of measurements over a range of magnitudes and frequencies are taken at the new position. The chamber is rotated back to the original position and the measurements are repeated. This process of taking radial and longitudinal measurements is done several times over the course of an experiment.

A TM deformation measurement begins by opening the shutter of the CCD camera. The mechanical shutter generates vibrations of the specimen. Therefore, the vibrations are allowed to settle and the camera remains open throughout the measurement. When the vibrations have died out, a sinusoidal force is generated on the magnetizable bead. The current applied to the magnet coils is ramped up to a desired amplitude using a Hanning window over the span of 0.5 seconds which is intended

to minimize unwanted transients generated by step changes in the force. When the amplitude has reached the desired level, a series of eight strobe illuminated pictures are taken at specific phases of the force stimulus. As shown in Figure 2-14, the image taken at each phase is generated from several strobe pulses. The multiple strobe pulses are necessary to generate a suitable level of brightness and contrast in the image for the computer vision algorithms. Each image is written to the hard disk and another measurement begins.

Chapter 5

Response of the Isolated Mouse Tectorial Membrane to Applied Forces

The magnetic bead method was used to apply forces to isolated TM preparations and to measure the resulting motions of the magnetizable bead and the surrounding tissue. This chapter summarizes results for 12 preparations, each from the apical portion of the TM of a mouse.

5.1 Tectorial membranes

In each experiment, one magnetizable bead and many non-magnetic polystyrene beads (1 to 2 μm radius) were typically attached to the middle zone of the TM. The middle zone was approximately 150 μm in width and is 43 μm thick on average. Several other TM features are shown in Figure 5-1. The fibrillar structure of the TM appears as dark and light striations running vertically in the image. The slight slant of the fibers, which was discussed in Figure 1-7 is also evident in Figure 5-1. Near the bottom edge of the middle zone is the marginal zone of the TM which appears as a thick ridge. The thin limbal zone of the TM extends vertically beyond the upper boundary of the image. Extending out of the image to the left and right, the longitudinal dimension

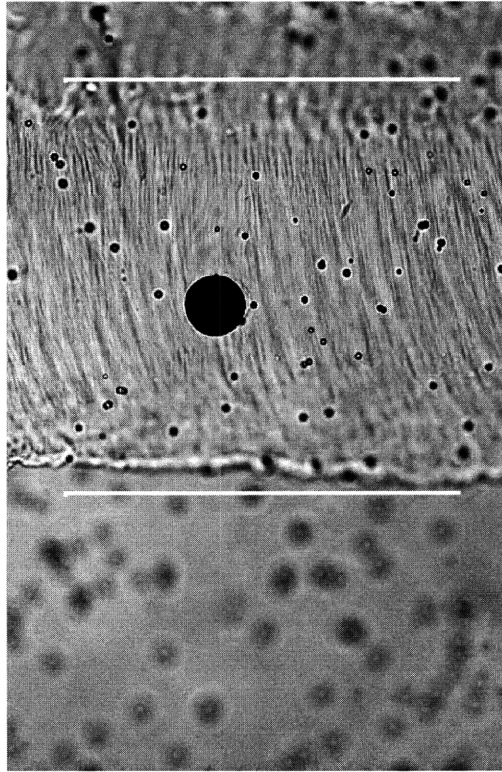


Figure 5-1: Isolated TM with magnetizable bead and polystyrene marker beads. The image shows a $25\ \mu\text{m}$ diameter magnetizable bead (large black circle) attached to the free surface of a TM. Non-magnetic polystyrene beads ($2\ \mu\text{m}$ diameter, small black circles) are scattered on the surface of the tissue. The white lines highlight the middle zone of the TM which is approximately $150\ \mu\text{m}$ wide. Blurred spots in the lower part of the image are polystyrene beads attached to the bottom of the chamber and are out of focus.

of the TM sample is typically $500\ \mu\text{m}$. Visual confirmation of structural landmarks like those seen in Figure 5-1 is important for orienting the TM relative to the magnets and for interpreting the mechanical response of the tissue to applied forces.

Magnified images of 12 isolated tectorial membranes discussed in this chapter are shown in Figure 5-2. Each image shows a 6% SiFe bead and the surrounding tissue of the TM middle zone. The images show the various sizes of the beads used in the experiments, ranging from a $6.5\ \mu\text{m}$ radius bead in experiment #5, to a $13\ \mu\text{m}$ radius bead in experiment #12. In addition to the bead location and size, several other characteristics of the experiments are summarized in Table 5.1. In experiments #4, #5, #9, and #11, the bead is attached to the covering net side of the TM. The time from CO_2 asphyxiation to the first motion measurement and the thickness of the TM are recorded. These factors may affect TM mechanical properties.

experiment	radius(μm)	covering net	thickness (μm)	time (min)
1	9	down	40	120
2	9	down	48	105
3	10	down	50	345
4	8.5	up	42	90
5	6.5	up	44	120
6	9	down	40	300
7	9	down	42	1740
8	7.5	down	40	180
9	8.5	up	47	540
10	12.5	down	40	75
11	9	up	39	110
12	13	down	46	160

Table 5.1: Some characteristics of TM experiments. A number of factors can affect the response of the TM to applied forces. The size of the bead, the orientation of the covering net, the TM thickness at the location of the bead, and the time from asphyxiation to the first measurement are recorded in the table.

5.2 Amplitude dependence of bead displacements

5.2.1 Linearity

Results were obtained from each of the isolated TM sections shown in Figure 5-2. Displacement measurements were made of the magnetizable bead resulting from different current stimulus amplitudes from 0.3 to 6.6 amps at 10 Hz. Displacements associated with forces applied in both the radial and longitudinal directions were measured.

The results from a typical experiment are shown in Figure 5-3. The magnitude and phase of the fundamental frequency of the bead's displacement waveform are plotted versus current amplitude. In this example, the radius of the bead is 9 μm . The measured displacement magnitudes¹ and phases for all 12 experiments are compiled in Appendix A. Figure 5-3 highlights several points which are common across all experiments.

At low current amplitudes, there is considerable scatter in the measured displace-

¹Displacement magnitudes, unless otherwise stated, refer to the peak magnitude.

ment magnitude and the corresponding phase angle. The displacements at these current levels are near the noise floor of the motion measurements (on the order of 20 nm). At high current amplitudes, there is a flattening in the slope of the displacement magnitude which is indicative of magnet core saturation, while the phase angle approaches -45 degrees. The maximum displacements are on the order of $1 \mu\text{m}$.

There are two particularly important trends in the left plot of Figure 5-3. First, the measured displacements for longitudinally applied forces are consistently larger than the corresponding displacements for radially applied forces. Second, over a range of currents (middle range), the displacements are nearly proportional to the square of the current, marked by the solid line with a slope of 2. Recall, according to theory and supported by calibrations the force on a bead is proportional to the square of the current. Thus, displacements which fall along the solid line are linearly proportional to the applied force. In order to look more closely at the linearity of displacements, data for middle current levels were analyzed across all experiments.

The vertical dotted lines in Figure 5-3 mark the middle current region (greater than 0.5 A, less than 2.7 A) where data are typically above the scatter associated with the low current levels and below the saturation behavior of the high current levels. In each experiment, a line was fit to the data in the middle current region using a least squares method. When a linear least squares fit is determined for set of data (x_i, y_i) , the linear correlation coefficient r , defined as

$$r = \frac{\sum_i (x_i - \bar{x})(y_i - \bar{y})}{\sqrt{\sum_i (x_i - \bar{x})^2} \sqrt{\sum_i (y_i - \bar{y})^2}}, \quad (5.1)$$

is a measure of the strength of the correlation (Press et al., 1988). A fit with a negative r value indicates a negative slope and analogously, a positive r value indicates a positive slope. The closer the r value is to ± 1 , the stronger the correlation. The slope of the least squares fit and the r value were computed for each experiment and plotted in Figure 5-4. Displacements for both longitudinally (left plots) and radially (right plots) applied forces show strong correlations with the applied current amplitude. Although, the fits for radial forces are somewhat less strong. The experiments which

produce low r values for radial forces did not necessarily produce lower r values for longitudinal forces. The low r values are typically associated with experiments having the most scatter at low current amplitudes (see Appendix A, experiments #4 and #5). In the bottom plots of Figure 5-4, the slopes corresponding to large r values approach 2. For radial and longitudinal forces, the mean slopes for $r > 0.95$ are 1.7 and 1.8 respectively. Thus, there is evidence that, over a range of currents, bead displacements approximate proportionality to force.

The phase angles of bead displacements in the middle current region are plotted in Figure 5-5 for each experiment. The values were compiled from the phase plots in Appendix A. Compared to longitudinal forces, phase angles associated with radial forces show a larger range of values and consequently more scatter in each experiment. The displacements consistently lag the current stimulus by 45 to 50 degrees for both longitudinal and radial forces.

5.2.2 Point stiffness

The relation between force and displacement provides information about the stiffness of an isolated TM. The middle current levels, which are below core saturation, can be converted to a force using Equation 3.6. The forces in the middle region of Figure 5-3 range from approximately 0.005 to 0.05 μN . Using estimates of the applied force magnitude f and the measured displacement of the bead d , a point stiffness associated with the TM region attached to the bead can be calculated using the ratio f/d . The point stiffnesses for the middle currents of Figure 5-3 are plotted in Figure 5-6 (left plot). The median stiffnesses vary slightly with the magnitude of the force. In contrast, an idealized spring which obeys Hooke's Law ($f = kd$) has a constant stiffness k for all force magnitudes. Point stiffnesses calculated in each experiment are summarized in Figure 5-6 (right plot). Measured stiffnesses when forces are applied in the radial direction are consistently larger than the corresponding stiffnesses for longitudinal forces. The median radial stiffness is approximately 3 times larger than the median longitudinal stiffness.

5.3 Frequency dependence

The data described thus far were all obtained at a frequency of 10 Hz. By fixing the current amplitude, and varying the frequency of the stimulus, frequency dependent properties of the TM were investigated. Displacement of the magnetizable bead were measured at 6 frequencies from 10 to 100 Hz with a current amplitude of 2.7 amps at each frequency. Measurements were obtained in experiments #6, #7, #8, #10, #11, and #12. The other 6 experiments either did not include frequencies other than 10 Hz or were conducted using the constant voltage mode of the current amplifier in which case motions above 40 Hz were attenuated below the noise floor of measurable motions. Measurements using the controlled current mode were adjusted to compensate for the small attenuation in Figure 3-10 at frequencies near 100 Hz.

The plots in Figure 5-7 show measured displacement magnitudes and phases as a function of frequency for a typical experiment. The bead in this example was $9\ \mu\text{m}$ in radius. Several trends are notable in Figure 5-7. Displacement magnitudes associated with both longitudinal and radial forces show a distinct decrease in magnitude with frequency. The lines through the data are least squares fits with slopes of -0.34 and -0.38 for longitudinal and radial forces respectively. Similar to the trend in Figure 5-3, the magnitude of the displacements for longitudinal forces are larger than the corresponding displacements for radial forces. The phase angle for displacements associated with both force directions are near -45 degrees across frequencies.

The displacement magnitude and phase trends for each experiment were very similar (see Appendix B). Consequently, the results were pooled and plotted in Figure 5-8. The plots in Figure 5-8 summarize the results for all frequency measurements and emphasize the frequency dependence of bead displacements. The displacement magnitudes in each experiment were normalized using the maximum displacement for that experiment at 10Hz. A least squares fit was determined for pooled displacement data longitudinal (top left plot) and radial (top right plot) applied forces. The fits are characterized by slopes of -0.465 (10 dB/decade) and -0.386 (8 dB/decade) for longitudinal and radial forces respectively. In addition, the phase estimates were

pooled and confirm the results of Figure 5-7. The phase of the displacement lags the stimulus by nearly -45 degrees across frequencies.

As a comparison, the responses of a pure, viscous damper and a simple, elastic spring are plotted along with the measured responses of the bead. The damper is assumed to have a velocity linearly proportional to the applied force, while the spring has a displacement linearly proportional to the applied force. As result, the damper's response is characterized by displacement decreasing at a rate of 20 dB/decade and having a phase lag of 90 degrees. The corresponding characteristics of the spring are constant displacement across frequencies and an phase angle of 0 degrees. The response of the TM falls between these two elements.

5.4 Longitudinal and radial stiffness

There is a general trend which spans all the measurements. The measured displacement magnitudes for longitudinally applied forces are consistently larger than displacements for radially applied forces under similar conditions. Thus, the measured response of the isolated mouse TM is anisotropic.

The evidence of the anisotropy is presented in Figure 5-9. Each radial measurement is paired with a longitudinal measurement from the same experiment and with the same stimulus conditions. The data pairings for every stimulus condition across all experiments are plotted in Figure 5-9 along with a solid black line having a slope of 1. Displacement pairings above this line indicate larger radial displacements and pairings for which this occurs in Figure 5-9 are generally confined to small magnitude (less than $0.1 \mu\text{m}$) displacements. However, 95% of the data fall below this line which is consistent with the results shown in Figure 5-6, suggesting that the isolated TM is less stiff in the longitudinal direction.

5.5 TM deformations

5.5.1 Relation between tissue motion and marker bead motion

Apart from producing motions of the magnetizable bead, applied forces produce deformations of the tissue surrounding the bead. The spatial extent of the deformations around the bead can give information about mechanical coupling between neighboring regions of the TM. In order to measure displacements, the computer vision algorithms rely on contrast or intensity variations in the images. The TM, which is nearly transparent provides a difficult target. For this reason, two techniques were used to track the deformations of the tissue.

Non-magnetic, polystyrene spheres, which can be seen in Figure 5-2 were allowed to settle onto the surface of the tissue. Motions of the polystyrene spheres are assumed to represent the motion of the tissue location where they rest. The spheres provide sufficient contrast for the computer vision algorithms. However, the location of each sphere cannot be controlled and often regions exist with no spheres in them. This can be seen in Figure 5-1. Increasing the concentration of spheres, increases the surface coverage, but tends to produce large groups of beads which stick together and are not adequately attached to the TM surface. The bead groups drift and confound motion estimates.

Alternatively, the algorithm can rely on contrast provided by the fibrillar structure of the TM to track tissue deformation. There are several advantages to this method. The fibrils are ubiquitous and therefore do not limit the locations which can be measured. The measured displacements of the fibrils are direct measurements of the tissue displacement.

These two motion tracking methods are compared in Figure 5-10. The image in Figure 5-10 highlights several regions used by the computer vision algorithm to estimate motions. Regions extending in both the longitudinal and radial directions, were selected to track a polystyrene bead or were placed without regard to the position of

polystyrene beads and were intended to track fibrillar structure. The force in these results was applied in the longitudinal direction and longitudinal displacements were measured in each selected region. The plots in Figure 5-10 show the longitudinal displacement estimates for each highlighted region versus the distance of the region from the center of the magnetizable bead. The results using the fibrillar structure are consistent with those obtained using the polystyrene beads. Thus, the location of displacement estimates is not restricted to regions containing high contrast polystyrene marker beads.

5.5.2 Spatial extent of deformation: Space constant

A space constant λ is a quantitative measure of the spatial extent of the deformation into the surrounding tissue. The space constant is defined as the distance to the location where the displacement magnitude has decreased by a factor of $1/e$. This distance is estimated by fitting an exponential function ($e^{-\frac{x}{\lambda}}$) to the data which is a straight line in semi-logarithmic coordinates. The slope of the line is used to estimate the space constant. When estimating space constants for the magnetic bead method, the component of the displacement parallel to the applied force is chosen for each region. In Figure 5-10, the slope of the exponential fit to the longitudinal displacements for regions in the longitudinal direction is -0.02 and for regions in the radial direction is -0.03 . Thus, in this case, the space constant is $13 \mu\text{m}$ in the longitudinal direction and $15 \mu\text{m}$ in the radial direction.

Space constants were measured for a range of stimulus conditions. Possible variations in space constants with changes in force amplitude and frequency were investigated. Ten 30 pixel by 30 pixel regions in the surrounding tissue were selected for each experiment. In general, five regions were selected in the radial direction and in the longitudinal direction for both radially and longitudinally applied forces. All regions were selected without regard to the presence of a polystyrene marker bead. The image in Figure 5-10 shows the typical orientation of the regions used to measure tissue displacements. The region encompassing the magnetizable bead was selected for each measurement so that the bead was centered and the dimensions of the re-

gion were slightly larger than the largest displacement of the bead. The radial and longitudinal regions were then positioned relative to this region. The displacement data for longitudinal and radial regions were fit with an exponential function as in Figure 5-10. The quality of the fit was evaluated using a linear correlation coefficient r .

The correlation coefficients for 12 experiments using current amplitudes of 1.4, 2.7, and 5.5 amps at 10 Hz are shown in Figure 5-11. In general, the largest $|r|$ values correspond to longitudinally applied forces at large current amplitudes. In most cases, the r values for longitudinal forces are negative and indicate the measured displacement magnitudes decay away from the point of the applied force. This decrease in displacement was confirmed visually using images from the experiments. These results are in marked contrast to r values for radially applied forces. The correlation coefficients for radial forces show considerable scatter and are not consistently positive or negative, indicating both increasing or decreasing displacements with distance. The difference between results for longitudinal and radial forces is summarized in the whisker plots of Figure 5-11. When pooled across experiments, the r values for radially applied forces show larger range (more scatter) and the median r values are small in magnitude (poor correlation) and both positive and negative (inconsistent).

In addition to changes in current amplitude, the frequency of the current stimulus was varied. The correlation coefficients for 6 experiments (#6, #7, #8, #10, #11, and #12) are plotted in Figure 5-12. The amplitude of the current stimulus was 2.7 amps across frequencies. The $|r|$ values for longitudinally applied forces are characteristically larger, show less scatter, and are more consistently negative than the corresponding values for radially applied forces. These characteristics are summarized in the whisker plots which pool the data across experiments.

Figure 5-11 and Figure 5-12 indicate that the best correlations (large, negative r values) occur when displacement magnitudes are large, which was typical for longitudinal forces. The results do not indicate a systematic difference between least squares fits to data for different current amplitudes and frequencies.

We expect that space constants associated with large $|r|$ give a more accurate

representation of the spatial extent of tissue deformation. The slope of the least squares fit is plotted versus the corresponding r value in Figure 5-13 and Figure 5-14. For radially applied forces, the correlation coefficients are small. Thus, the deformation measurements are not able to convincingly resolve space constants for radially applied forces. However, for longitudinally applied forces, the average slope for r values below -0.8 is -0.026 and -0.024 for the longitudinal and radial directions respectively. In this case, the space constants are approximately $12 \mu\text{m}$ and $11 \mu\text{m}$ in the longitudinal and radial directions respectively.

5.5.3 Propagation of deformations

The phase of the displacement magnitude for regions surrounding the magnetizable bead also provides information about how the tissue deforms. A continuous change in the phase with distance can indicate a propagating displacement in the TM. The phase of tissue displacements was estimated for regions in the longitudinal and radial directions for both longitudinal and radial directed forces. The spatial variation of the phase of tissue displacements was investigated for different amplitudes and frequencies of the force stimulus spanning the range of excitations used in the magnetic bead method.

Phase estimates for 12 TM's associated with 3 force amplitudes (1.4 A, 2.7 A, and 5.5 A) were pooled and are plotted in Figure 5-15 as a function of distance from the center of the magnetizable bead. There is considerable scatter. Lines fit through the data using a least squares method, indicate a consistent phase lag, but the slopes do not indicate a consistent trend in phase as a function of distance.

Similarly, phase angles for 6 TM's were estimated for forces at 3 frequencies. Figure 5-16 shows results pooled over experiments #6, #7, #8, #10, #11, and #12 at frequencies of 20, 40, and 100 Hz. As was the case for Figure 5-15, lines fit to the data indicate a phase lag but do not show a systematic variation with distance.

The results of Figure 5-15 and Figure 5-16 suggest the displacements of the surrounding tissue are approximately in phase with the motion of the bead over the range of excitations used in the magnetic bead method. There is no measurable

propagation of tissue displacement in the isolated TM preparation for the amplitude and frequency range used in the bead method.

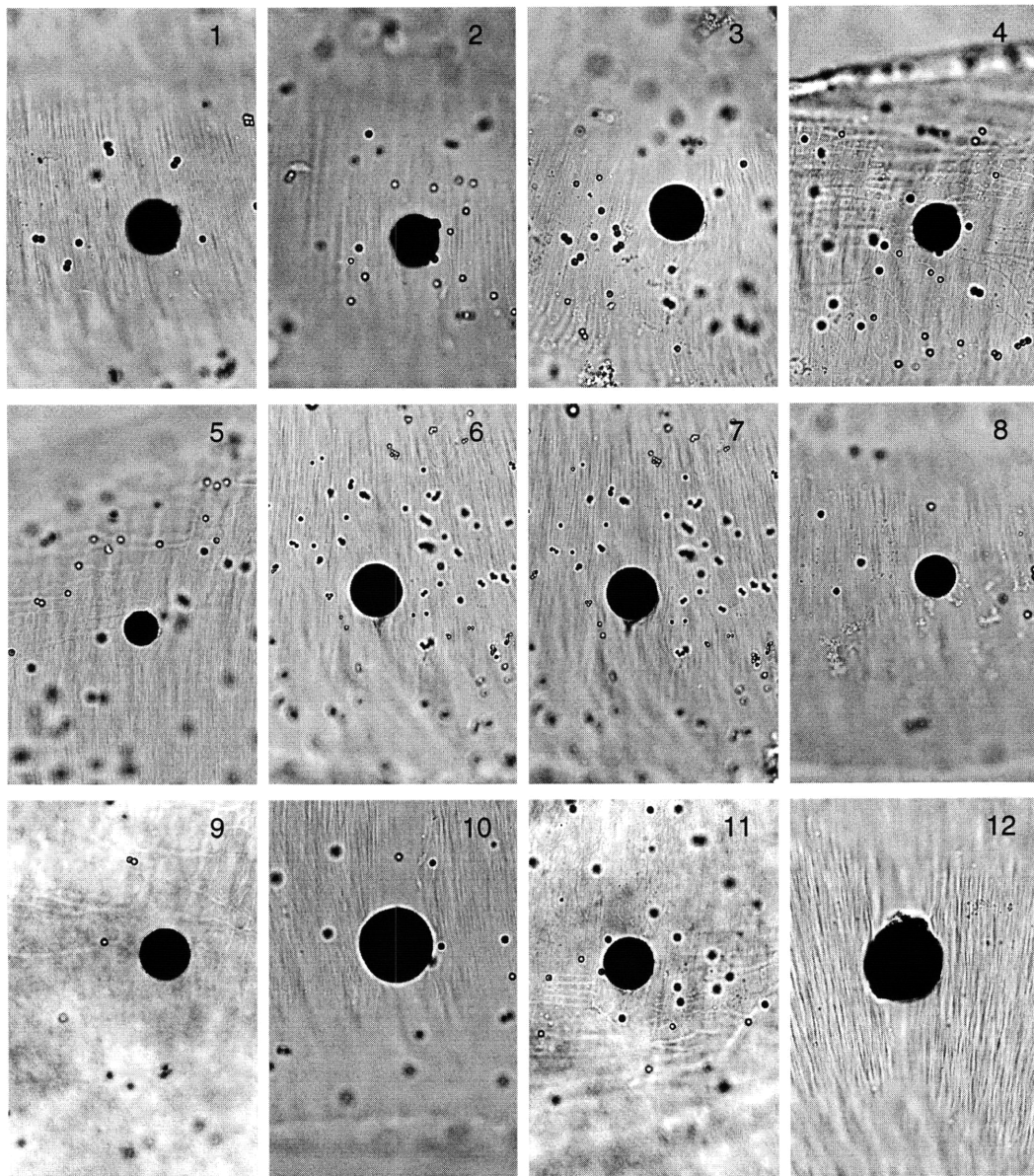


Figure 5-2: The magnetizable beads and TM sections from 12 experiments. The large black circle in each image is a magnetizable bead. The smaller dark circles in each image (except experiment 12) are non-magnetic polystyrene beads which have been allowed to settle onto the surface of the tissue. No polystyrene beads were used in experiment 12. The images were taken using light microscopy and the contrast was enhanced independently for each image.

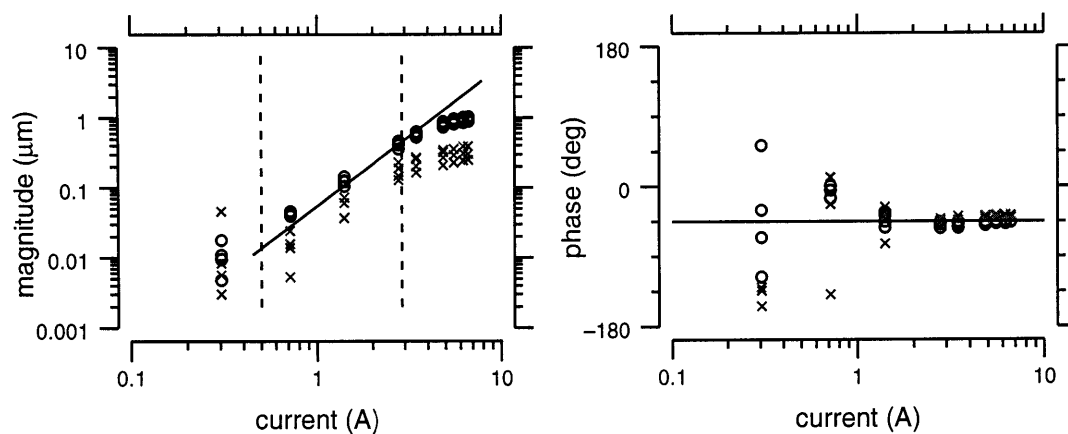


Figure 5-3: Bead displacement magnitude and phase versus amplitude of applied current for a typical experiment. The magnitude of the fundamental frequency of the displacement waveform is plotted versus current amplitude (left plot) at a frequency of 10 Hz. The solid line has a slope of 2. The vertical dotted lines mark the region used for analysis of TM linear response. The phase of fundamental frequency with respect to the current stimulus is plotted versus current amplitude (right plot). The horizontal solid line represents -45 degrees. The black circles and gray x's are measurements associated with longitudinally and radially applied forces respectively.

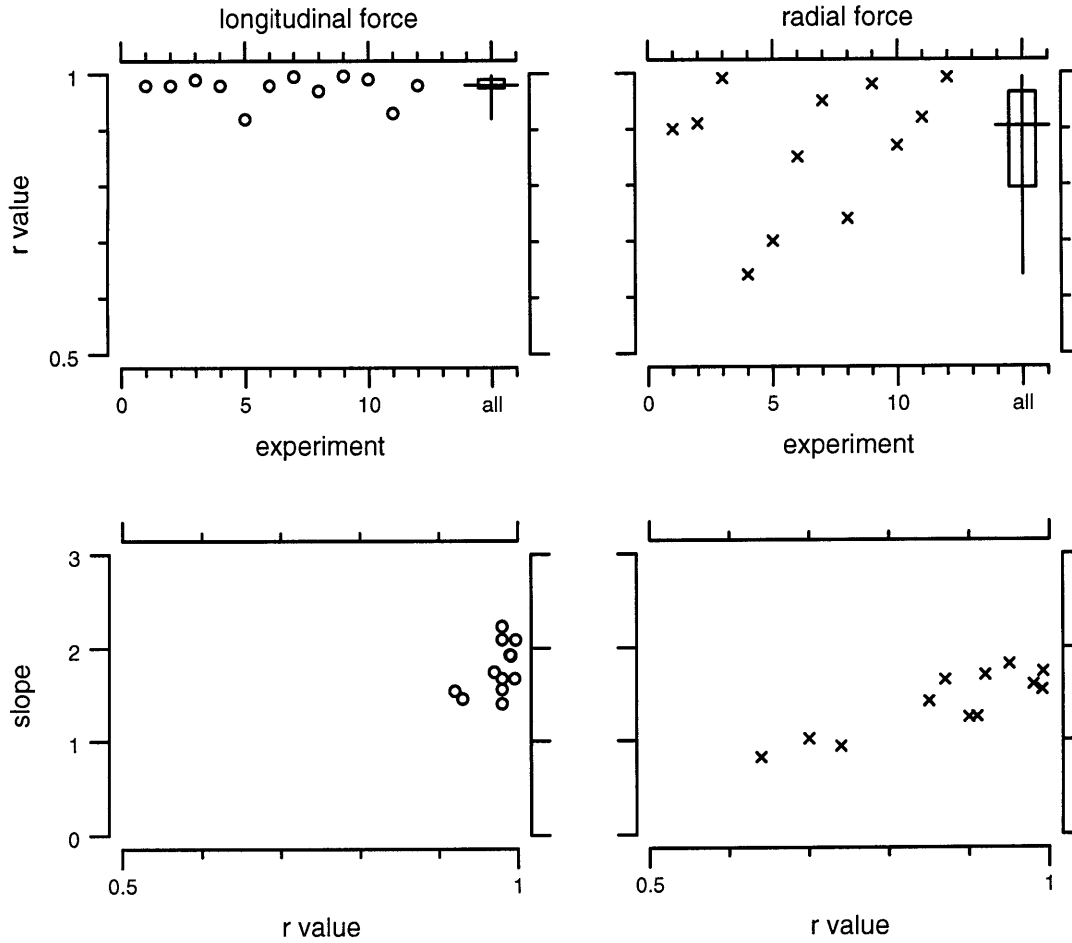


Figure 5-4: Correlation coefficients and slopes for lines fit to bead displacement data at middle range current amplitudes and 10 Hz. Lines were fit to measured displacements using a least squares method. The top two plots show the correlation coefficient calculated for each experiment. All fits for longitudinal forces have r values near 1. There is considerably more scatter in the r values for radial forces. In the last column of both plots, a whisker plot summarizes the r values across all experiments. The vertical line indicates the range of values, the horizontal line marks the median value, and the box encompasses the interquartile range of the values. The slopes of the fits are plotted versus the r values for each experiment in the bottom two plots. For r values near 1, the slopes are clustered near a value of 2.

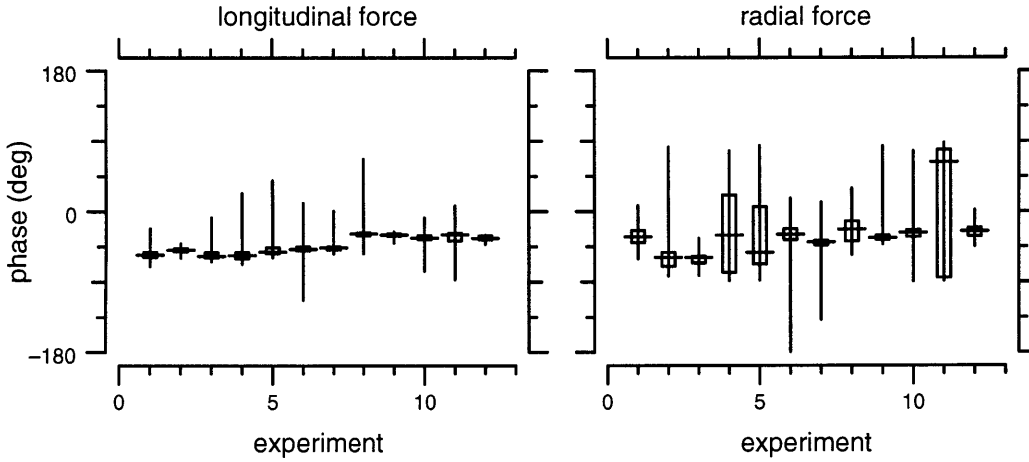


Figure 5-5: Phase of bead displacement with respect to current stimulus across all experiments. The phase of the bead displacement waveform was calculated for all current amplitudes at 10 Hz and pooled for each experiment. Data for both longitudinally applied forces (left plot) and radially applied forces (right plot) were pooled. The pooled phase data are represented by whisker plots which are described in Figure 5-4. The displacements lag the stimulus by nearly 45 degrees across all experiments.

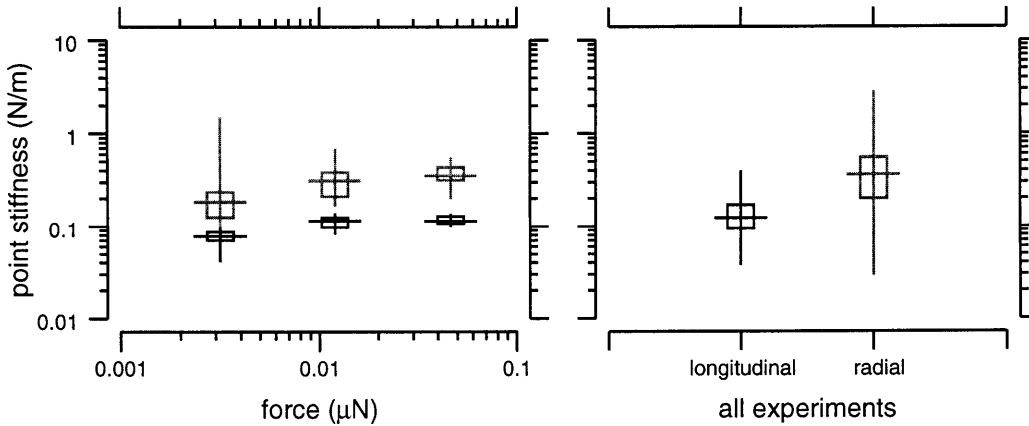


Figure 5-6: Point stiffness versus applied force for middle range current amplitudes. The applied force was calculated using Equation 3.6 and was divided by the magnitude of the bead displacement to calculate a point stiffness associated with the bead location. The plot on the left shows point stiffness for radial (gray whisker plots) and longitudinal (black whisker plots) applied forces from a typical experiment. A whisker plot summarizes the data at each force level. Whisker plots are described in Figure 5-4

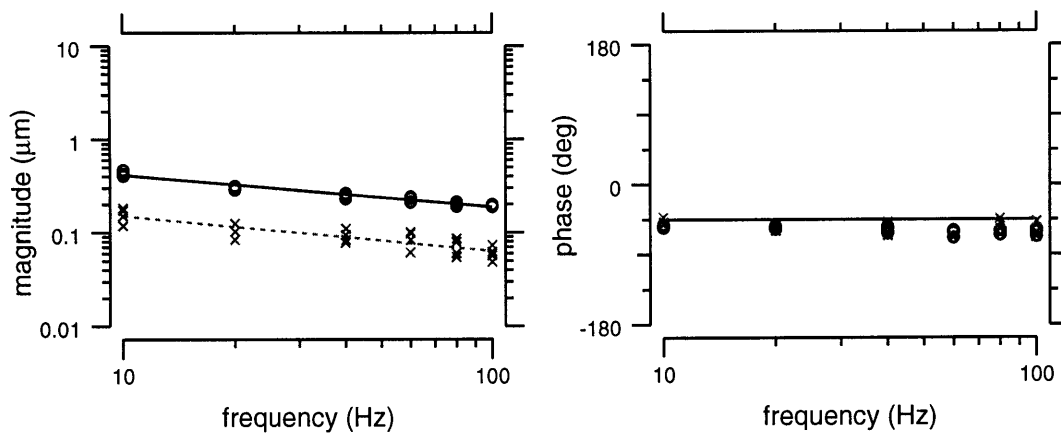


Figure 5-7: Bead displacement magnitude and phase versus frequency of applied current for a typical experiment. The magnitude of the fundamental frequency of the displacement waveform is plotted versus current frequency (left plot) for a current amplitude of 2.7 amps. The solid line and dotted line (left plot) are least squares fits through the data for longitudinally and radially applied forces respectively. The phase of the fundamental frequency with respect to the current stimulus is plotted versus current amplitude (right plot). The horizontal solid line represents a phase lag of -45 degrees. The black circles and gray x's, both plots, are measurements associated with longitudinally and radially applied forces respectively.

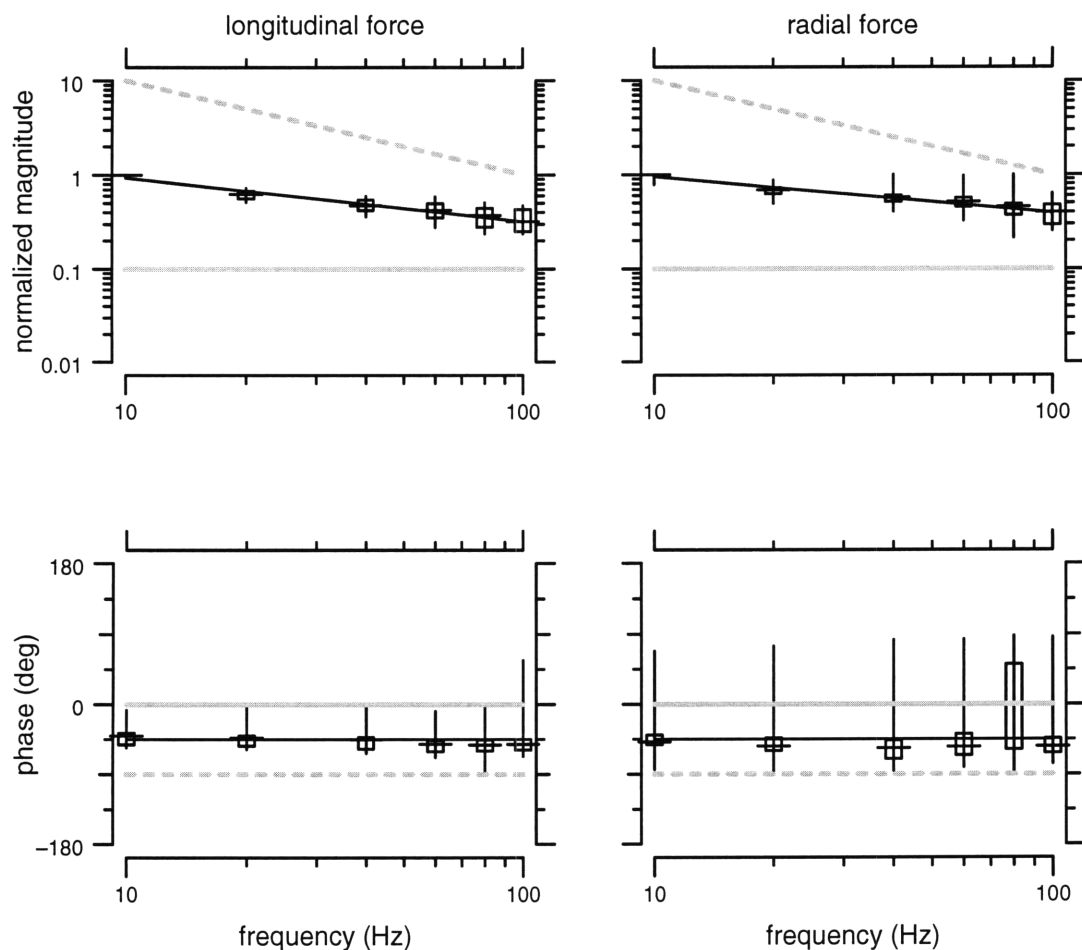


Figure 5-8: Measured bead displacements as a function of frequency pooled across experiments. Bead displacement magnitudes were normalized with respect to displacements at 10 Hz and pooled across frequencies. A whisker plot (see Figure 5-4) summarizes the data at each frequency. The top two plots show bead displacements for longitudinally (left plot) and radially (right plot) applied forces. The solid black lines are least squares fits to the data. The slope of the fit for longitudinally and radially applied forces is -0.465 and -0.386 respectively. The gray lines have slopes of -1 (dotted gray) and 0 (solid gray) corresponding to the response of a pure viscous damper and simple, linear elastic spring respectively. The bottom two plots show the phase of the bead displacement with respect to the current stimulus plotted versus stimulus frequency and pooled across experiments. The solid black line marks -45 degrees and the gray lines mark 0 degrees (elastic spring) and -90 degrees (viscous damper).

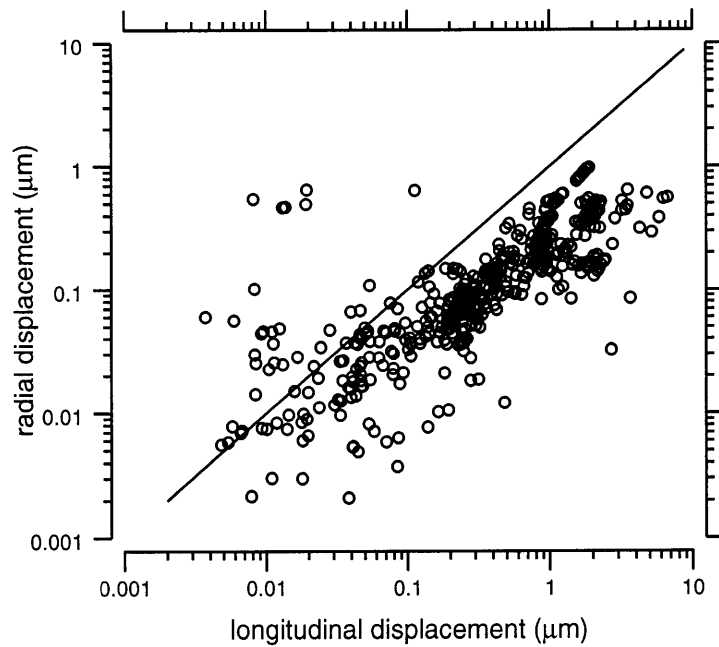


Figure 5-9: Paired displacement estimates for radially applied forces and longitudinally applied forces. Each data point is plotted using a radial displacement estimate and a longitudinal displacement estimate from the same experiment under identical conditions. Data from all current amplitudes and frequencies were used. Thus, each symbol represents two independent measurements. There are a total of 586 data points representing 1172 independent measurements.

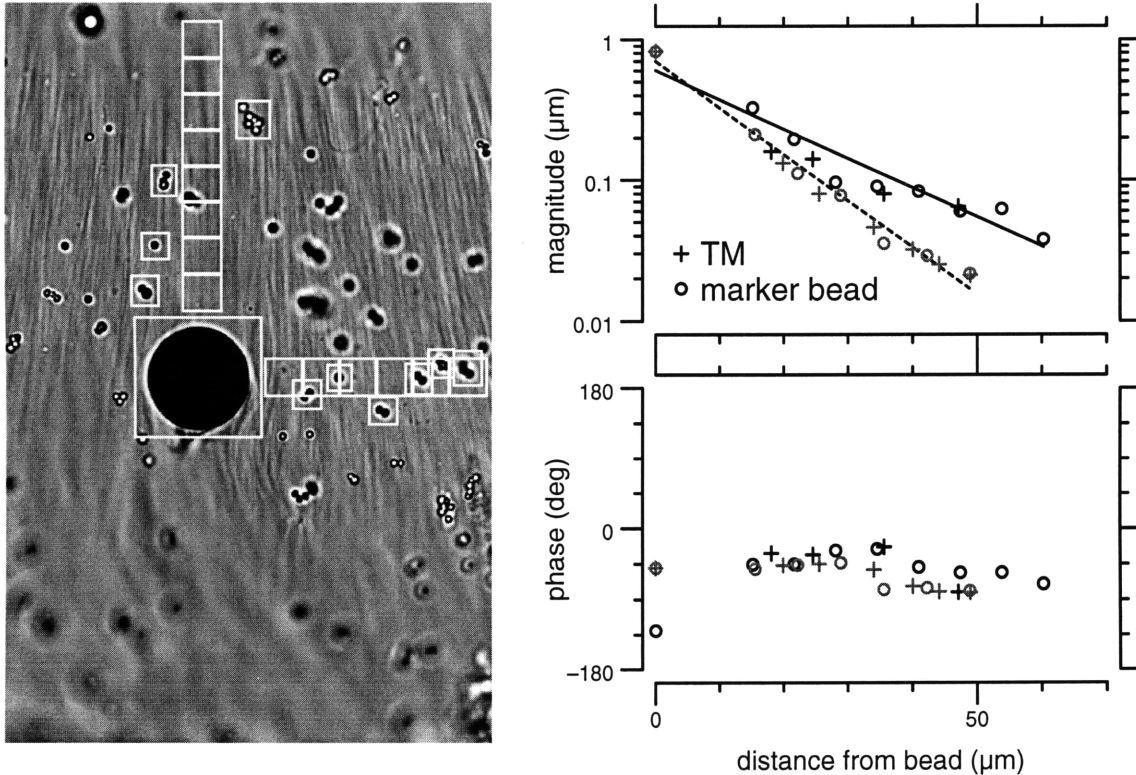


Figure 5-10: Comparison of measured marker bead and tissue displacement. The displacements of the highlighted regions in the TM image (left) are plotted versus the distance from the magnetizable bead. The image shows a $9\ \mu\text{m}$ radius 6%SiFe bead (large black circle) fixed to the surface of a section of TM. In this case, the magnetic force is applied in the longitudinal (horizontal) direction. The amplitude of the current stimulus was 2.7 amps ($0.04\ \mu\text{N}$) at a frequency of 10Hz. The regular square regions are 30 pixels by 30 pixels and are intended to track the tissue. These regions extend to the right, in the longitudinal direction, and towards the top of the image, in the radial direction, in a straight row and column respectively. The regions containing the polystyrene beads also extend longitudinally and radially but are irregularly spaced. In the plots (right panel), the black symbols correspond to regions extending in the radial direction and the gray symbols correspond to longitudinal regions. The results in Figure 5-10 are from a single set of 8 strobe illuminated images.

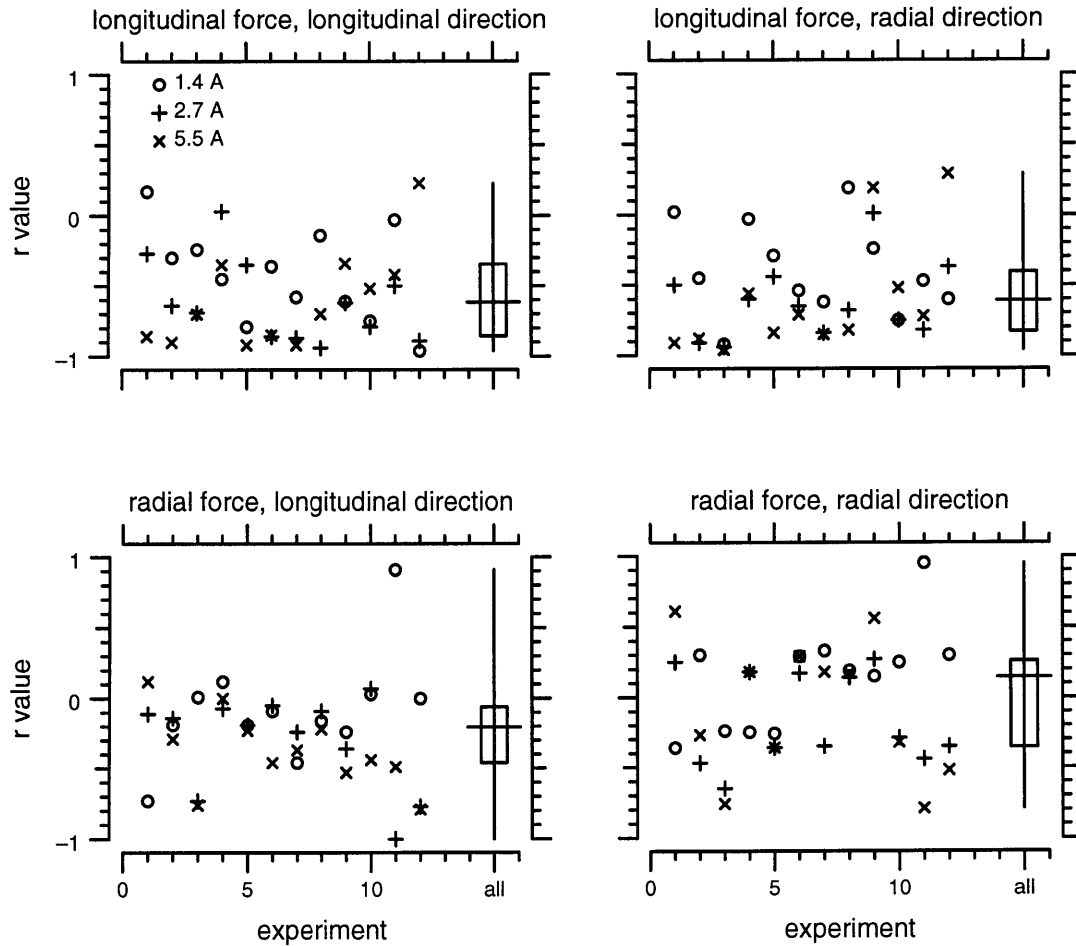


Figure 5-11: Variation of correlation coefficients with current amplitude. Lines were fit to the deformation data using a least squares method. The correlation coefficients associated with the fit are plotted for each of 12 experiments. The top panels show the correlation coefficients for deformations in the longitudinal direction (left) and the radial direction (right) associated with forces applied in the longitudinal direction. Analogously, the bottom panels show the correlation coefficients for deformations in the longitudinal direction (left) and the radial direction (right) associated with radially applied forces. Results from three current levels (1.4 A, 2.7 A, 5.5 A) are plotted. The stimulus frequency in all cases is 10 Hz. In, the last column a whisker plot represents the pooled results across experiments. Whisker plots are explained in Figure 5-4.

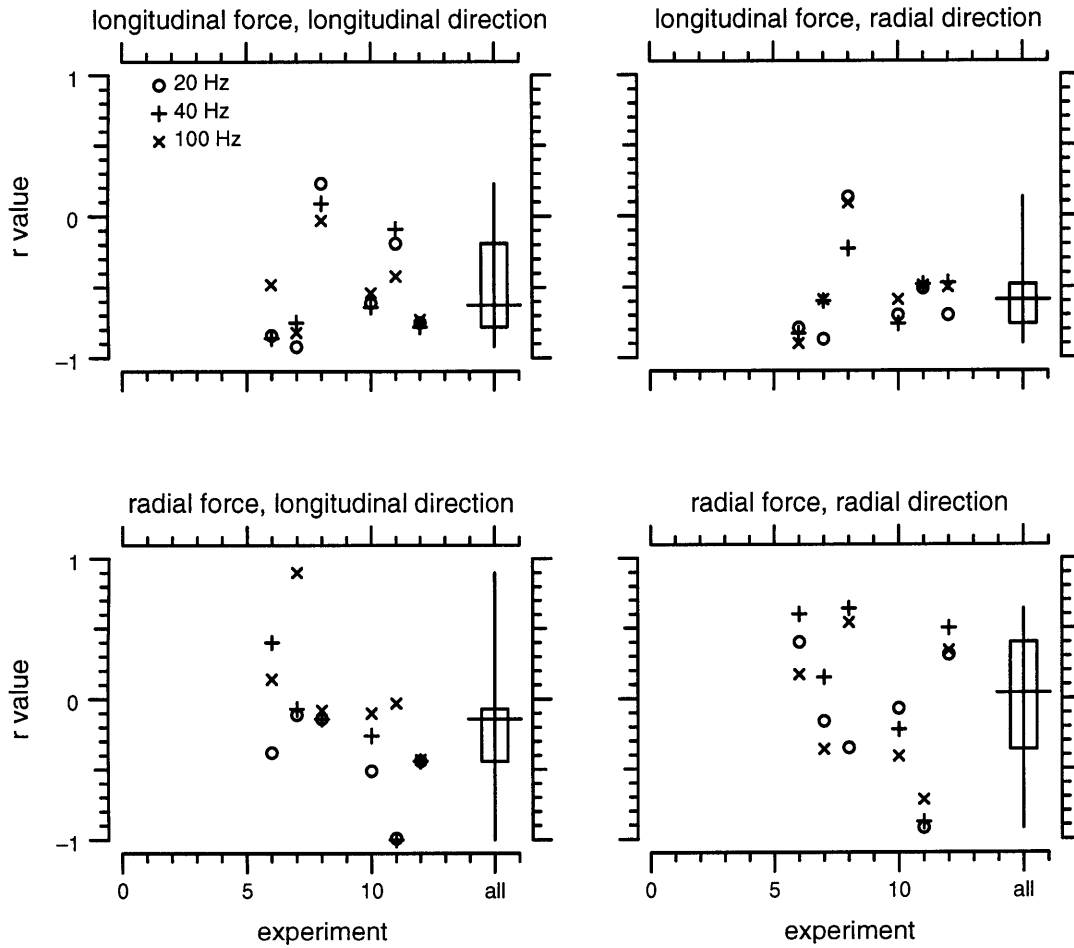


Figure 5-12: Variation of correlation coefficients with current frequency. Lines were fit to the deformation data using a least squares method. The correlation coefficients associated with the fit are plotted for each of 6 experiments (#6, #7, #8, #10, #11, and #12). Results from three frequencies (20 Hz, 40 Hz, 100 Hz) are plotted. Other aspects of this figure are explained in Figure 5-11.

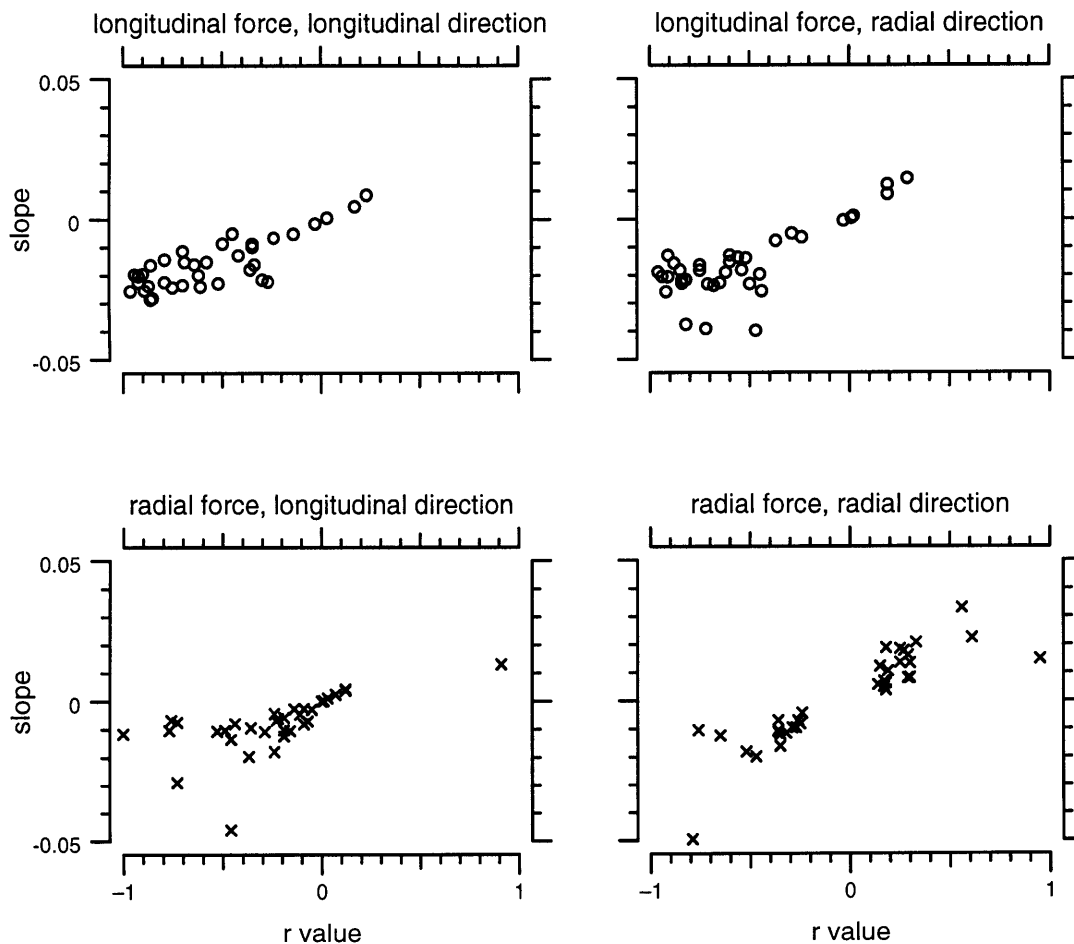


Figure 5-13: Correlation coefficients and slopes for TM displacements near the magnetizable bead at different current amplitudes. Lines were fit to the measured TM displacements using a least squares method. The slope is plotted versus the correlation coefficient for 12 experiments at 3 current amplitudes (1.4 A, 2.7 A, 5.5 A). The stimulus frequency was 10 Hz. The slopes for longitudinal forces with r values below -0.8 are near -0.025 in both directions.

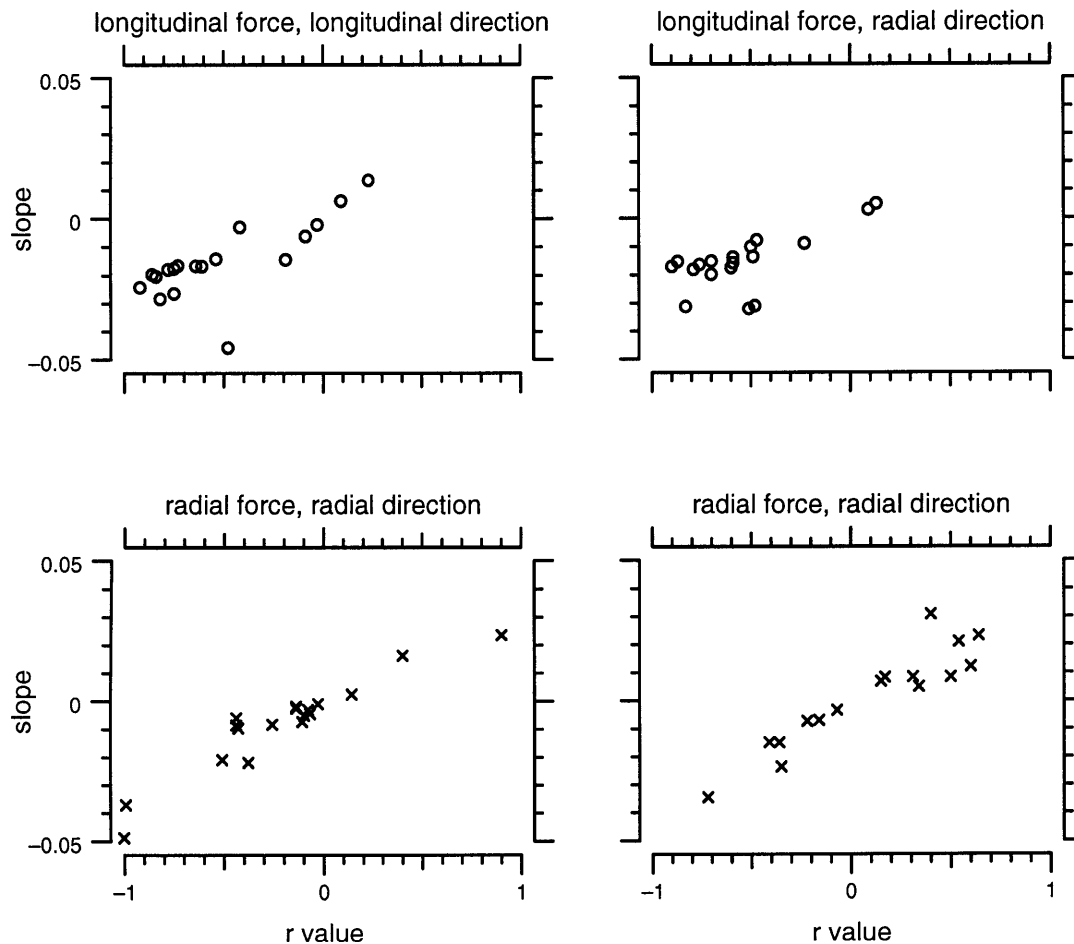


Figure 5-14: Correlation coefficients and slopes for TM displacements near the magnetizable bead at different current frequencies. Lines were fit to the deformation data using a least squares method. The slope is plotted versus the correlation coefficient for 6 experiments (#7, #8, #9, #10, #11, and #12) at 3 stimulus frequencies (20 Hz, 40 Hz, 100 Hz). The stimulus current was 2.7 amps. Slopes for longitudinal forces with r values below -0.8 are near -0.02 in both directions.

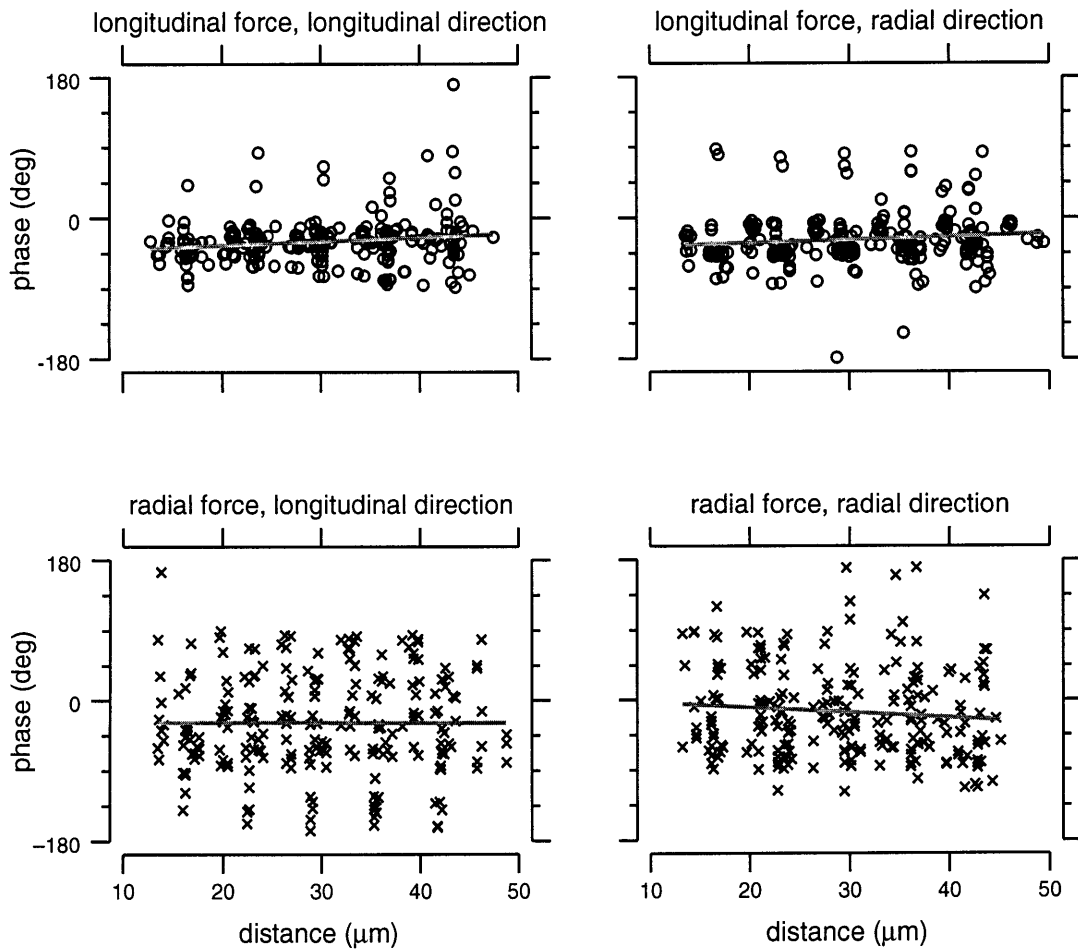


Figure 5-15: Pooled results showing the spatial dependence of the phase of measured displacement magnitudes at 3 current stimulus amplitudes. Results for experiments 1 through 12 are shown. The phase of the tissue displacement relative to the current stimulus was estimated at locations extending radially and longitudinally from the magnetizable bead. The plots show the phase for radial and longitudinal locations associated with forces applied in the radial and longitudinal direction. Results for peak current amplitudes of 1.4 A, 2.7 A, and 5.5 A were pooled. Each symbol represents an independent phase estimate based on the displacement waveform determined from a sequence of 8 images. The solid gray lines in each plot are the result of least squares fits to the data.

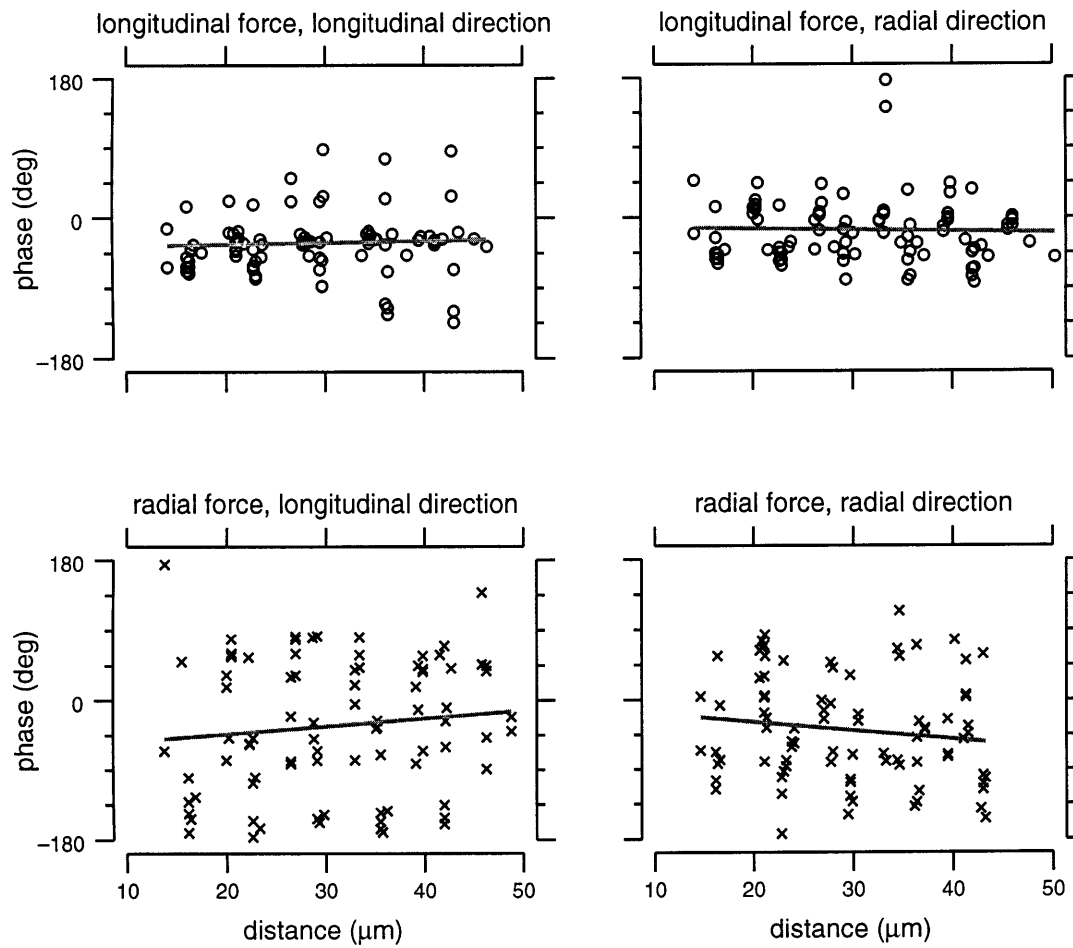


Figure 5-16: Pooled results showing the spatial dependence of the phase of the measured displacement at 3 current stimulus frequencies. Results for experiments #6, #7, #8, #10, #11 and #12 are shown. Results for current frequencies of 20 Hz, 40 Hz, and 100 Hz were pooled. Other aspects of this figure are explained in Figure 5-15.

Chapter 6

A Discussion of the Magnetic Bead Method and TM Measurements

The measurements of the preceding chapter are the first quantitative, measurements of dynamic mechanical properties of the tectorial membrane. This chapter describes a number of issues involving both the magnetic bead method and the isolated TM preparation that are important to consider when interpreting the measurements. The chapter concludes with a brief summary of the major results.

6.1 Magnetic bead method

6.1.1 Effect of bead size

The size of the magnetizable bead is found to influence TM measurements in several ways.

Magnitude of force. When a force is applied to a magnetizable bead attached to a TM, the stiffness of the TM acts to resist motion of the bead. If the force is not large enough to generate motions that are significantly larger than the measurement noise floor (near 20 nm), then motion measurement noise adds scatter to the TM measurements. For example, the motions for forces applied in the stiffer radial direction

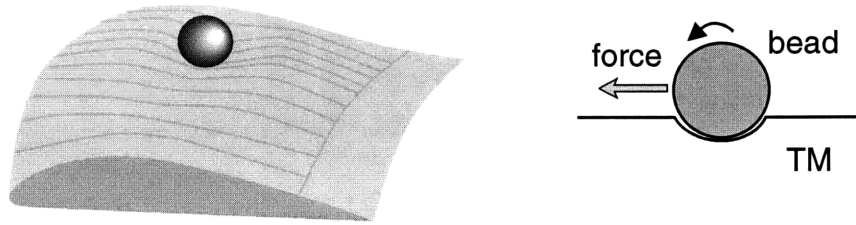


Figure 6-1: Unintended motions of magnetizable bead. The attachment of the bead to the TM (left panel) determines how forces on the bead produce motions of the bead and tissue. In general, the TM makes contact with only a small portion of the surface of the bead. As a result, a force applied to the bead can cause the bead to roll (right illustration) rather than simply translate.

tend to show more scatter. It has been shown in Equation 2.7 and in the calibration results of Figure 3-12 that larger beads and larger current amplitudes produce larger forces. In the TM measurements, bead radii greater than or equal to $9 \mu\text{m}$ typically produced measurable motions (at current levels above 0.05 A). However, the use of big beads ($> 9 \mu\text{m}$) brings with it other issues regarding how the bead is attached to the TM.

Rolling and non-sinusoidal motion. A bead is coated with adhesive and attached to the TM by gently pressing it into the surface of the tissue. The resulting attachment is not always uniform. Furthermore, as the size of the bead increases, the contact between the bead and TM increasingly supports a rocking mode of motion (Figure 6-1) rather than a simple translation. In extreme cases, a bead can rock without any deformation of nearby tissue. In other cases, the bead may not be uniformly attached and the resulting motion of the bead is not a symmetric sine wave. An example of this is shown in Figure 6-2, where positive displacements of the bead show considerable distortion. The distortion is evident in both the displacement waveform and the magnitudes of the harmonics. Observing the motion through the microscope or watching the acquired image sequence after a measurement often reveals irregularities in the motion. Problems with attachment were found to occur more frequently with big beads ($> 9 \mu\text{m}$) than with little beads.

Thus, there is a trade-off between big and little beads in the magnetic bead method. Big beads are capable of producing large, measurable deformations of the

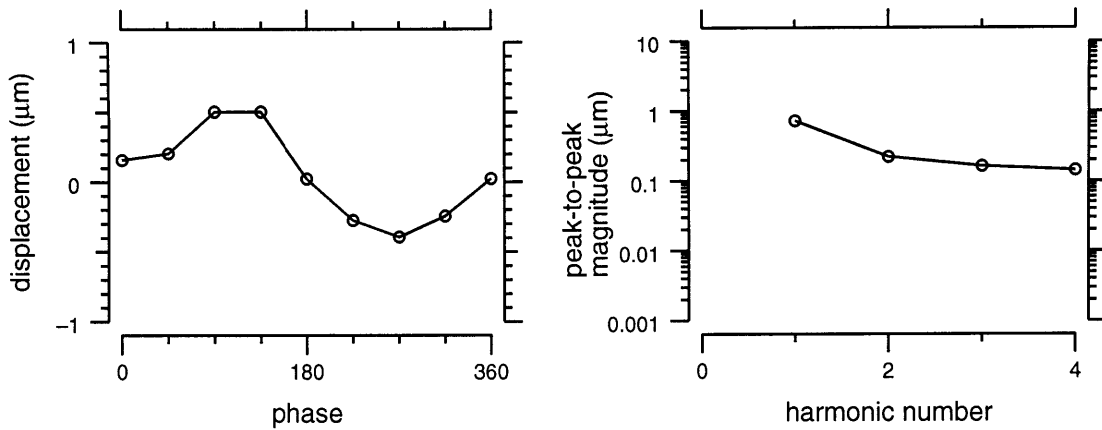


Figure 6-2: Non-sinusoidal displacement waveform. Uneven attachment of the bead to the TM as well as surface variations in the tissue can produce distortions in the displacement waveforms. A displacement waveform (left plot) is shown for a 2 amp current at 10 Hz. Distortions are visible in the waveform and are reflected in the large magnitudes (relative to the fundamental) of the harmonics (right plot).

tissue, but the attachment of big beads can be problematic. Little beads can be attached more firmly, over more of the bead's surface area, but the tissue motions are smaller.

6.1.2 Point stiffness

The relation between the point stiffness measured with a magnetizable bead and bead size is complex. Force increases with the volume of the bead, and the resulting displacements with big beads tend to be larger. However, contact area between the bead and TM also increases with bead size. Thus, the amount of material that moves increases with bead size. This tends to reduce the displacement observed with big beads. To understand this tradeoff, a simple model was investigated.

Simple model. The deformations of a semi-infinite, linear elastic solid (sometimes called an elastic half-space) under the action of static forces distributed over the bounding surface was first considered by Boussinesq in 1885 (Timoshenko and Goodier, 1970). The deformations caused by a static force tangent to the bounding surface Figure 6-3 can be expressed in closed form,

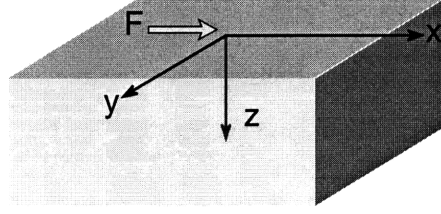


Figure 6-3: An elastic solid with a tangential point force applied to its surface. The material geometry is a half space which extends to $\pm\infty$ in the x and y directions and to $+\infty$ in the z direction. The plane $z = 0$ defines the surface bounding the material. A point force F is applied to the surface, at the origin, in the positive x direction at the origin. Thus, the x axis is defined as the parallel direction relative to the force, and the y axis is defined as the orthogonal direction.

$$u = \frac{F}{4\pi G} \left[\frac{1}{R} + \frac{x^2}{R^3} + (1 - 2\nu) \left(\frac{1}{R+z} - \frac{x^2}{R(R+z)^2} \right) \right] \quad (6.1)$$

$$v = \frac{Fxy}{4\pi G} \left[\frac{1}{R^3} - (1 - 2\nu) \frac{1}{R(R+z)^2} \right] \quad (6.2)$$

$$w = \frac{F}{4\pi G} \left[\frac{xz}{R^3} - (1 - 2\nu) \frac{x}{R(R+z)} \right] \quad (6.3)$$

where u , v , and w represent displacements in the x , y , and z direction, $R = \sqrt{x^2 + y^2 + z^2}$, G is the shear modulus, and ν is Poisson's ratio (Lure, 1964).

Equations 6.1, 6.2, and 6.3 can be used to determine the relationship between the region over which the load is applied and the resulting displacement of the region. The region attached to the bead is assumed to have constant displacement. The distribution of shear stresses required to generate a constant displacement over a circular region is

$$t = \frac{t_o}{\sqrt{L}} \quad (6.4)$$

where $L = 1 - x^2/a^2 - y^2/a^2$ in which (x, y) is the position of a location on the bounding surface $z = 0$ and a is the radius of the circular region (Lure, 1964). The corresponding displacement of the region can be written as

$$u = \frac{f}{4Ga} \left(\frac{2}{\pi} C \right) \quad (6.5)$$

where f is the resultant shear force from Equation 6.4 and C is a constant, which for a circular region is 1.5708. According to Equation 6.5, the stiffness, defined as f/u ,

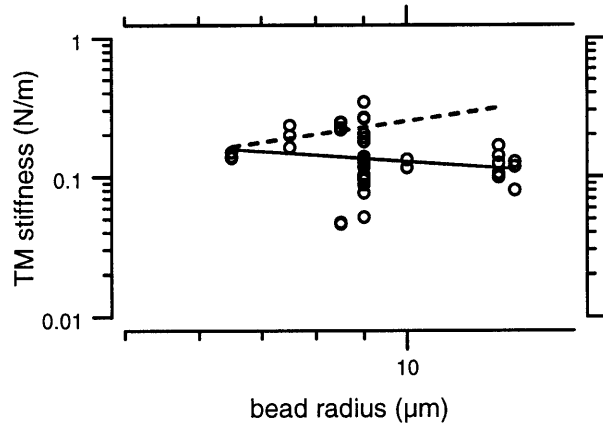


Figure 6-4: Relation between the measured TM stiffness and bead radius. Each symbol is a stiffness calculated from the ratio of the applied force and measured displacement. The data are from measurements made for longitudinally applied forces at 10 Hz with current amplitudes in the middle range. The solid black line indicates a least squares fit to the data and has a slope of -0.4. The fit is rather poor having a correlation coefficient of 0.3. The dotted line has a slope of 1 representing the relation predicted using Equation 6.5.

is proportional to the radius a of the area over which f is applied. If the radius of the applied force region is on the order of the bead radius (i.e. $a \approx r$), then TM stiffness measurements should increase with increasing bead radius.

For each of 12 TM's, longitudinal displacements associated with a longitudinal force of $0.01 \mu\text{N}$ (a force level in the middle current range for all beads used in the experiments) were used to calculate TM stiffnesses. In Figure 6-4, stiffness is plotted against bead radius for all TM experiments. The data in Figure 6-4 show stiffnesses which are generally near 0.1 N/m regardless of bead size. These stiffnesses do not fit with the assumption $a \approx r$.

The assumption that $a \approx r$ implies that about a quarter of the bead's surface area (total surface area $4\pi r^2$) is attached to the TM. However, images of the beads and TM indicate that, particularly for big beads (experiment #12), the area of attachment may be smaller ($a < r$). This may explain at least in part why the relation between measured stiffness and bead radius has a slope less than 1.

6.1.3 Conclusions

The size of the magnetizable bead has important consequences for both the magnitude of the applied force and how those forces are transmitted to the TM. In order to produce motions consistently above the noise floor, beads with at least a $9\ \mu\text{m}$ radius should be used. However, big beads more often produce unintended modes of motion, such as rolling.

Interpretation of point stiffness depends on contact area. Ideally, the contact area should be estimated in each experiment. However, direct determination of the contact area optically is not easy.

6.2 Isolated TM preparation

The magnetic bead method is applied to an isolated TM. However, the process of isolating the TM removes it from the natural environment of the cochlea. The attachment of the tissue to the chamber and the bathing solution are not natural and can affect the mechanical properties of the tissue. Even so, there are a number of advantages to using the isolated preparation. Foremost among these is that by removing the TM from the cochlea, measurements of the TM's response to applied forces are not confounded by interactions with other cochlear structures such as the hair cells. Although, the attachment to the glass chamber is not natural, it provides an unambiguous and reproducible attachment. In addition, removal from the cochlea allows access to the TM surface in contact with hair bundles. Mechanical properties of this surface have never been investigated before. Although, longitudinal and radial forces were applied to the TM middle zone, in principle, forces can be applied at any location and in any direction. The isolated preparation offers an unobstructed view of deformations resulting from the applied forces. This advantage allowed investigation of both TM point stiffness and the spatial extent of deformations associated with controlled, dynamic forces.

6.3 Application of the magnetic bead method to the isolated TM

6.3.1 Variation among TM preparations

To characterize variability of the results obtained, estimates of point stiffnesses were made in each experiment for the same magnetic stimulus (current amplitude 1.4 A, at 10 Hz). Much of the variability across experiments resulted from variability intrinsic to the measurement (as discussed above). However, some of the variability results from experiment conditions (Figure 6-5). There were significant differences between the longitudinal stiffness when the covering net was up or down (interquartile ranges do not overlap). There were no significant differences in radial stiffnesses measured with different covering net orientations. Variation in TM thickness may account for as much as a factor of 2 change in the measured stiffness across experiments, with thick tectorial membranes being less stiff than thin. Similarly, the simple passage of time may reduce stiffness by as much as a factor of 2 over the time period of a day.

6.3.2 Influence of the surrounding fluid

The isolated TM preparation was developed so that mechanical properties of the TM could be measured without interactions with nearby cochlear structures. However, the hydrodynamic forces due to the AE solution which bathes the TM could, at least in principle, affect the measured mechanical responses. As a result, it is necessary to address the possibility that the fluid provides a significant contribution to the force resisting the bead's motion. To examine this possibility, two simple geometries are investigated.

The motion of a sphere oscillating in a fluid is resisted by fluid forces. The relationship between the magnitude of the fluid force and the displacement of a sphere can be written as

$$F = 6\pi\mu r(j2\pi fX) \quad (6.6)$$

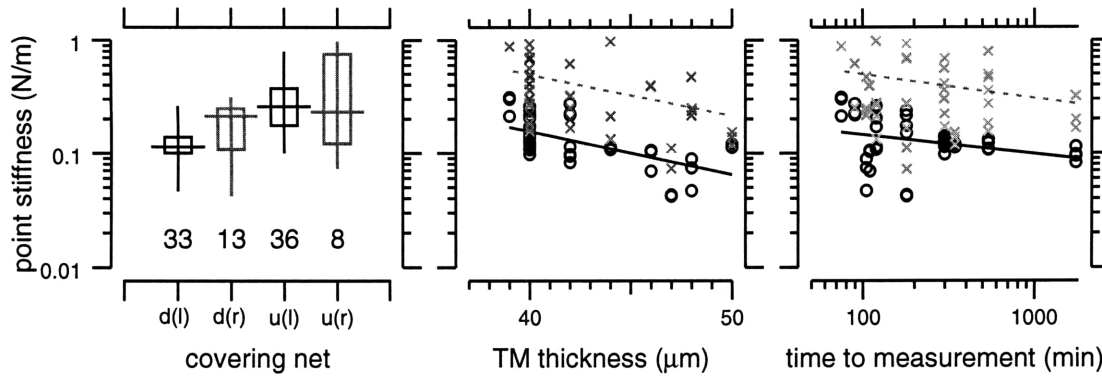


Figure 6-5: The effect of several characteristics of the TM preparations on measured point stiffness. The data from Table 5.1 are plotted versus the estimated point stiffness at a current amplitude of 1.4 amps and a frequency of 10 Hz. The results for both radial (gray x's and gray whisker plots) and longitudinal (black circles and black whisker plots) forces are shown. Stiffness measurements with the covering net down (longitudinal force d(l), radial force d(l)) and up (longitudinal force u(l), radial force u(r)) are summarized with whisker plots (left). The numbers below the whisker plots indicate the total number of measurements made for the given stimulus level and frequency. Stiffness measurements are plotted as a function of TM thickness (middle) and the time from asphyxiation to the first measurement (right). The solid and dotted lines are least squares fits through the data associated with longitudinal and radial forces respectively.

where μ is the viscosity of the surrounding fluid, r is the sphere's radius, f is the frequency of oscillation, j is $\sqrt{-1}$, and X is the amplitude of the displacement. The relationship between the fluid force magnitude and the frequency of oscillation of the sphere is plotted in Figure 6-7 for a $20 \mu\text{m}$ diameter sphere oscillating with a peak displacement of $1 \mu\text{m}$. Due to the motion and proximity of the nearby tissue, the fluid forces on the bead will not be identical to those in Figure 6-7 but will be on the

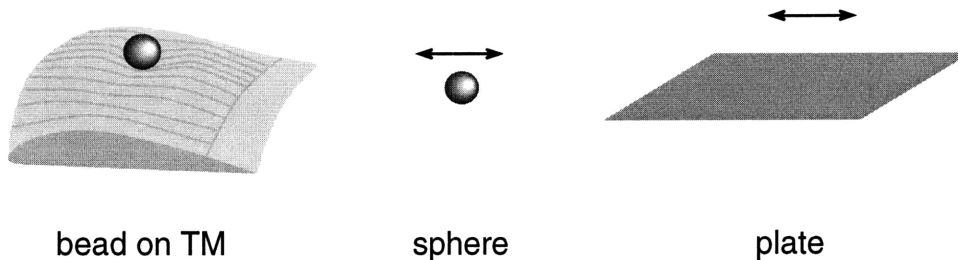


Figure 6-6: The surrounding fluid generates a resistive force on the bead and the deforming surface of the TM. The illustration depicts a simple interpretation of TM and bead motion. The bead attached to the TM is shown on the left which is decomposed into an oscillating sphere, representing the bead, and a plate, representing the deformations of the tissue near the bead.

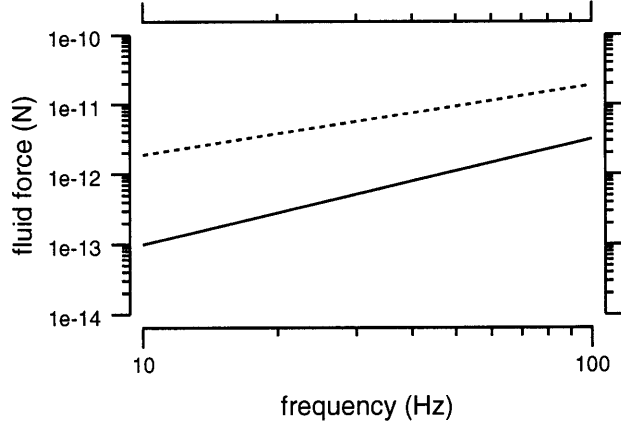


Figure 6-7: Peak forces required to oscillate a sphere and a plate at an amplitude of $1 \mu\text{m}$ over frequencies from 10Hz to 100Hz. The solid line represents the force required to oscillate a plate with an area of 1.6×10^3 square microns and the dotted line represents the required force to move a $20 \mu\text{m}$ diameter sphere. The surrounding fluid is assumed to be water.

same order. The magnitude of the force resisting the motion is on the order of 10^{-12} to 10^{-11}N over the frequency range from 10Hz to 100Hz. The fluid forces are 4 orders of magnitude smaller than the force applied to the bead in a TM experiment.

The deformation of the TM produces additional mechanical coupling to the surrounding fluid. As a first approximation, the region of deformation acts like an oscillating plate. The fluid force density F_d acting on a oscillating plate is a combination of viscous and inertial forces and is expressed as

$$F_d = \mu\sqrt{\pi f/\nu}(1 + j)(j2\pi fX) \quad (6.7)$$

where ν is the kinematic viscosity of the fluid (Freeman and Weiss, 1986). The magnitude of the fluid forces acting on a $40 \mu\text{m}$ square oscillating with a peak displacement of $1 \mu\text{m}$ is plotted in Figure 6-7 versus frequency. The fluid forces on the plate are 5 orders of magnitude smaller than those applied to a magnetizable bead.

Thus, the combined effect of fluid forces acting on a sphere and plate is much smaller than the applied magnetic forces and as a result contributes little to the measured response of the TM.

6.3.3 Frequency dependent displacements

Measured displacements of a magnetizable bead attached to the tectorial membrane depend on frequency. The magnitude of the displacement tends to decrease with increasing frequency at 10 dB/decade for longitudinal forces and 8 dB/decade for radial forces. The phase of displacement tends to lag that of the stimulus by 45 degrees. The evidence in Figure 6-7 indicate that the measured frequency dependence is not an artifact from interactions with the surrounding fluid. Because the frequency dependence of the bead's displacement is demonstrated to fall between the response of the a spring (elastic) and damper (viscous) this suggests that both elastic and viscous effects are important in governing the TM's mechanical response. This is consistent with the response of other polyelectrolyte gels such as cartilage (Hayes and Bodine, 1941) and biological fluids (King and Macklem, 1977; James and Marriott, 1982; Tran-Son-Tay et al., 1988).

6.3.4 Anisotropy

A fundamental characteristic of the isolated TM preparation is the attachment of the TM to the bottom of a glass chamber. This attachment (boundary condition) differs from the in situ boundary conditions of the TM. As a result, the measured response of the isolated TM to applied forces will be different from the in situ case. It is likely that the glass attachment constrains TM displacements much more than in situ attachments. Thus, the TM will appear stiffer when displacements are measured for the isolated preparation.

The results in Figure 5-9 indicate that the TM is less stiff (i.e. undergoes larger displacements) in the longitudinal direction than in the radial direction. This result could represent anisotropic material properties. Alternatively, it could result from the the effects of geometry and boundary conditions. The geometry of the TM samples in this study possess a radial dimension typically 2 times the thickness and 4 to 5 times shorter than the longitudinal dimension.

The response of a structure to a point force depends on the geometry of the

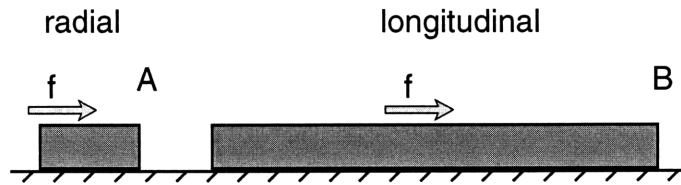


Figure 6-8: Forces applied to bodies with different geometries. The shaded rectangles represent samples of an isotropic, homogeneous material. In each case, one side of the rectangle is fixed and a force f is applied tangential to the opposite side. The geometries of body A and B are analogs of the TM cross-section in the radial and longitudinal directions respectively.

structure and its attachment to other structures. Figure 6-8 illustrates a narrow (A) and a wide (B) elastic body that are attached to a rigid boundary. If these bodies were made of identical materials, B is expected to have a greater stiffness than A.

The geometry of the isolated TM suggests that its longitudinal stiffness should exceed its radial stiffness. However, the measured stiffnesses show the opposite trend. This suggests that the material properties of the TM are anisotropic. The measured mechanical anisotropy in the TM is consistent with the structural anisotropy represented by radially oriented collagen fibrils. Collagen fibrils exist in many biological tissues and have been shown to provide specific mechanical properties (Zhu et al., 1996; Kempson et al., 1973). In particular, collagen is known to provide tensile and shear stiffening of tissues such as tendon and articular cartilage. In the TM, the fibrillar structure illustrated in Figure 1-7 coincides with the direction of maximum sensitivity of the hair bundles. Thus, stiffening in the radial direction may be important for the deflection of hair bundles.

6.4 Summary

An instrument for applying time-varying forces to microscopic tissue samples was developed and used to measure mechanical properties of the isolated mouse tectorial membrane (TM). The TM is believed to play an important mechanical role in the

inner ear of vertebrates. However, the mechanical properties of the TM are unknown.

Forces are applied to the TM with a magnetizable, silicon-iron bead (typically 10 micrometers in radius) attached to the surface of the tissue. A computer-controlled current source powers electromagnets which generate a time-varying magnetic field. The field produces a force on the bead, which exerts a tangential force on the surface of the TM. Resulting motions of the bead and adjacent tissue are measured using a video microscopy system with a resolution of 20 nanometers.

Measurements have been obtained for TMs from 12 mice. The magnitude of the magnetic bead's displacement at 10 Hz was nearly proportional to the magnitude of the applied force for forces from 0.0001 to 0.1 micronewton. However, displacements were smaller for forces applied in the radial direction than for forces in the longitudinal direction. The magnitude of the bead displacement decreased as the frequency of the applied force increased from 10 to 100 Hz — at 10 dB/decade for longitudinal forces and 8 dB/decade for radial forces. The phase of the displacement lagged that of the stimulus current by approximately 45 degrees across frequencies. Displacement of the adjacent tissue decreased as the distance from the magnetic bead increased, typically decreasing by $1/e$ over distances on the order of 12 micrometers.

These results suggest that mechanical properties of the TM are anisotropic: stiffness in the radial direction is greater than stiffness in the longitudinal direction. This mechanical anisotropy correlates with anatomical anisotropies, especially the radially oriented micro-structure of the TM.

Appendix A

Amplitude dependence for 12 TM experiments

The purpose of this appendix is to present displacement magnitude and phase data for each of 12 TM experiments. Current amplitudes from 0.03 amps to 6.6 amps at 10Hz were applied to the ring magnets. Resulting displacements of the magnetizable bead were measured for both radial and longitudinal forces. As described in Figure 5-3, the displacement data in each experiment is marked by scatter at low current levels and reveals core saturation above 2.7 amps. For middle current levels, displacement magnitudes are related to the square of the applied current. Furthermore, each experiment supports the trend that, at a given current level, the longitudinal displacements are larger than the radial displacements.

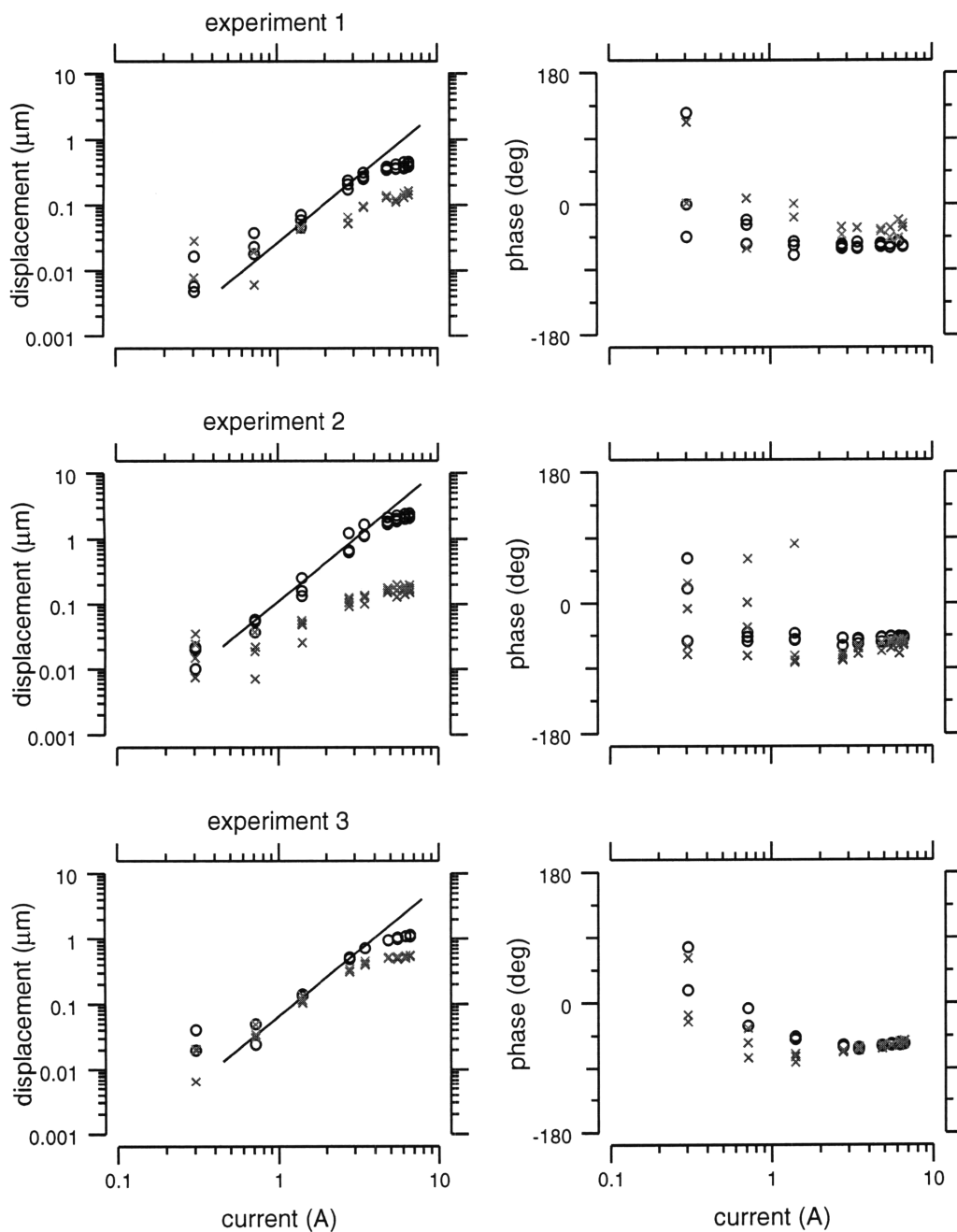


Figure A-1: Dependence of magnetizable bead displacement on current amplitude for experiments 1-3. The peak amplitude of the current stimulus used to induce a sinusoidal force at 10 Hz was adjusted from 0.3 to 6.6 amps (abscissa). Images at 8 phases of the stimulus were analyzed to determine the magnitude of the displacement of the magnetizable bead. Circles represent longitudinal displacements when the TM was oriented so that the magnetic force was in the longitudinal direction. The x symbols represent radial displacements for radial forces. The solid line has a slope of 2 and passes through the mean longitudinal displacement at 2.7 amps.

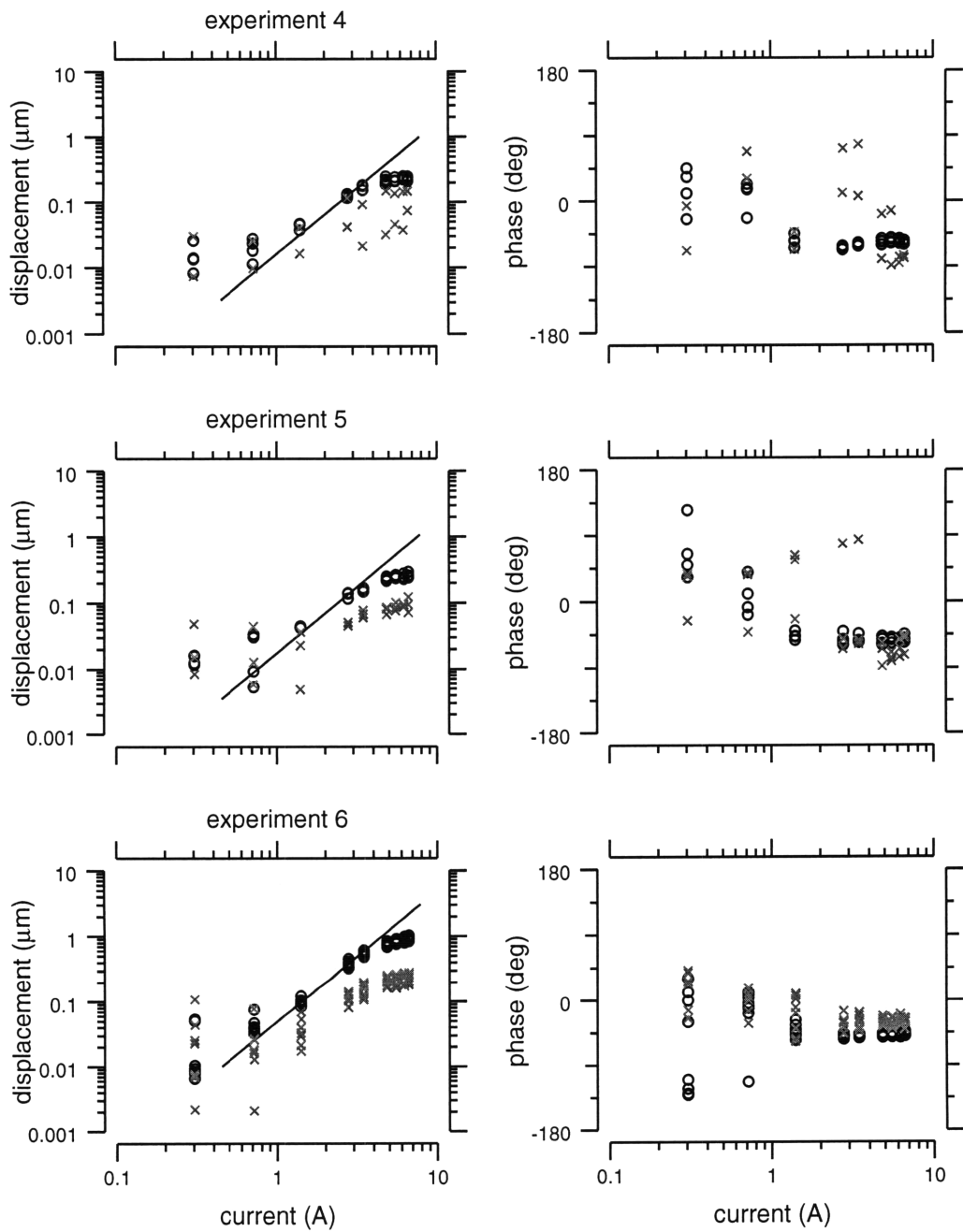


Figure A-2: Dependence of magnetizable bead displacement on current amplitude for experiments 4-6. Other aspects of this figure are described in Figure A-1.

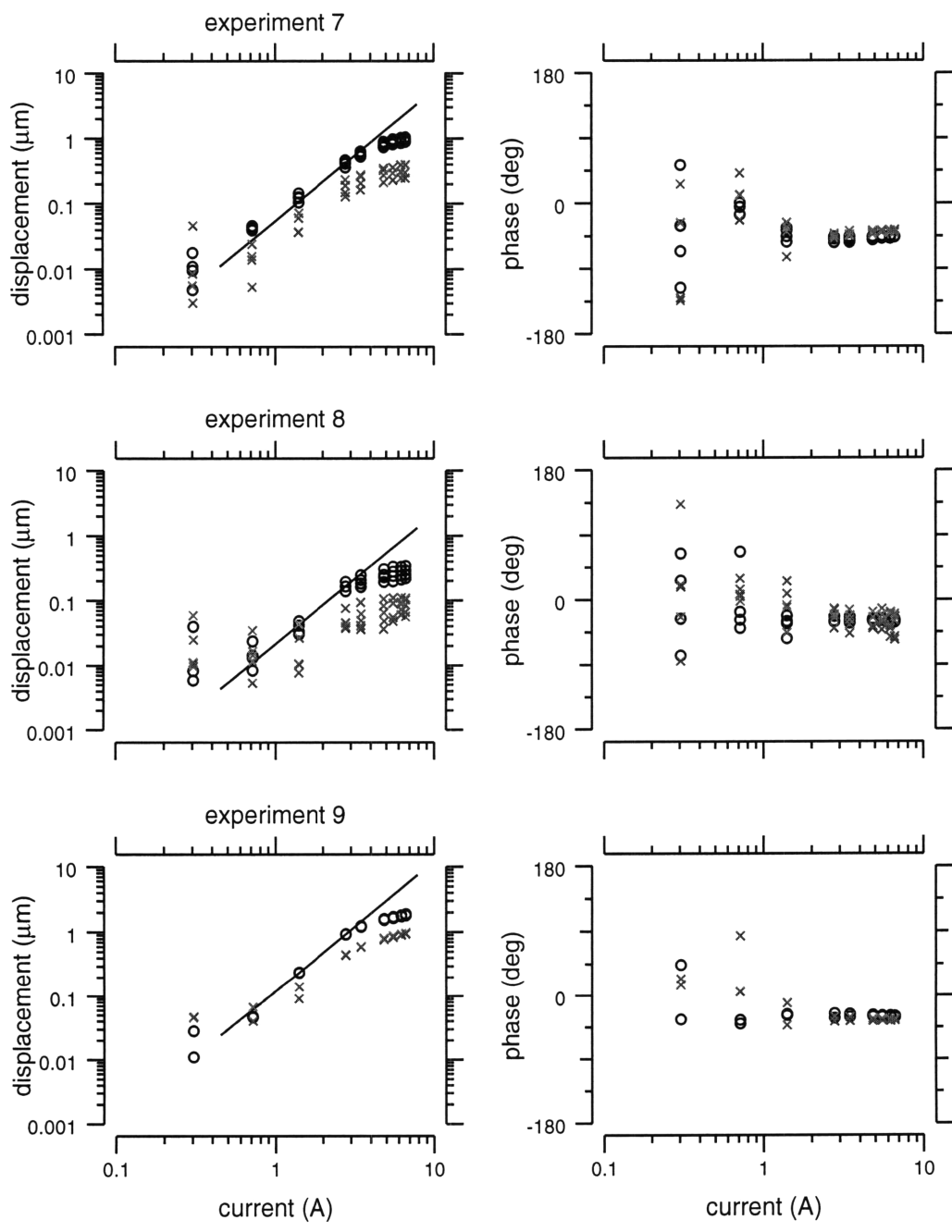


Figure A-3: Dependence of magnetizable bead displacement on current amplitude for experiments 7-9. Other aspects of this figure are described in Figure A-1.

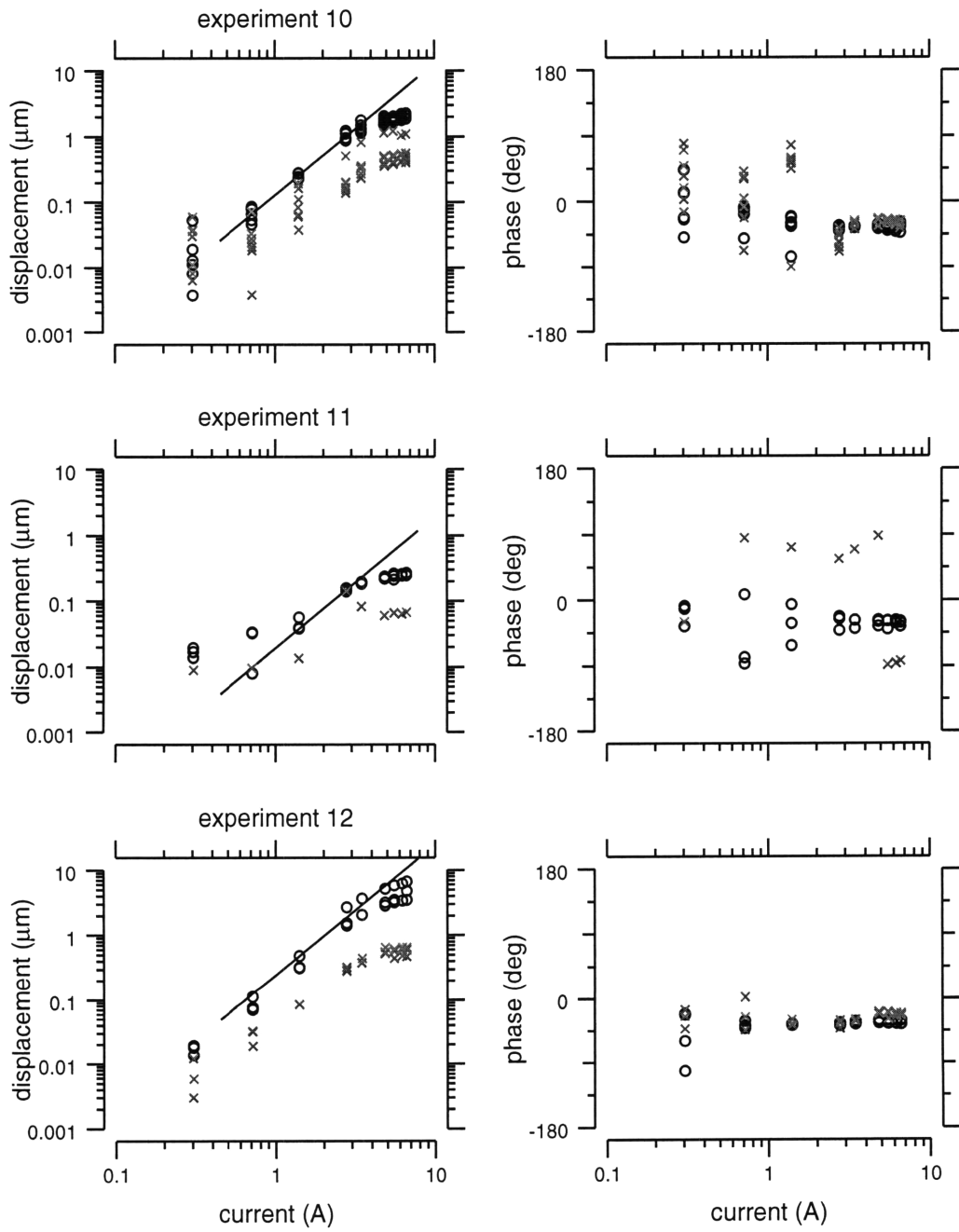


Figure A-4: Dependence of magnetizable bead displacement on current amplitude for experiments 10-12. Other aspects of this figure are described in Figure A-1.

Appendix B

Frequency dependence for 6 TM experiments

The purpose of this appendix is to present displacement magnitude and phase data for experiments #6, #7, #8, #10, #11, and #12. Current stimuli with an amplitude of 2.7 amps were applied to the ring magnets at frequencies of 10, 20, 40, 60, 80, and 100 Hz. In each experiment, forces were applied to the TM in both radial and longitudinal directions. Lines were fit through the displacement magnitudes using a least squares method. Each experiment emphasizes the features described in Figure 5-7. Displacements magnitudes decrease with increasing frequency. Furthermore, in every case, the displacements for longitudinal forces are larger than those for radial forces.

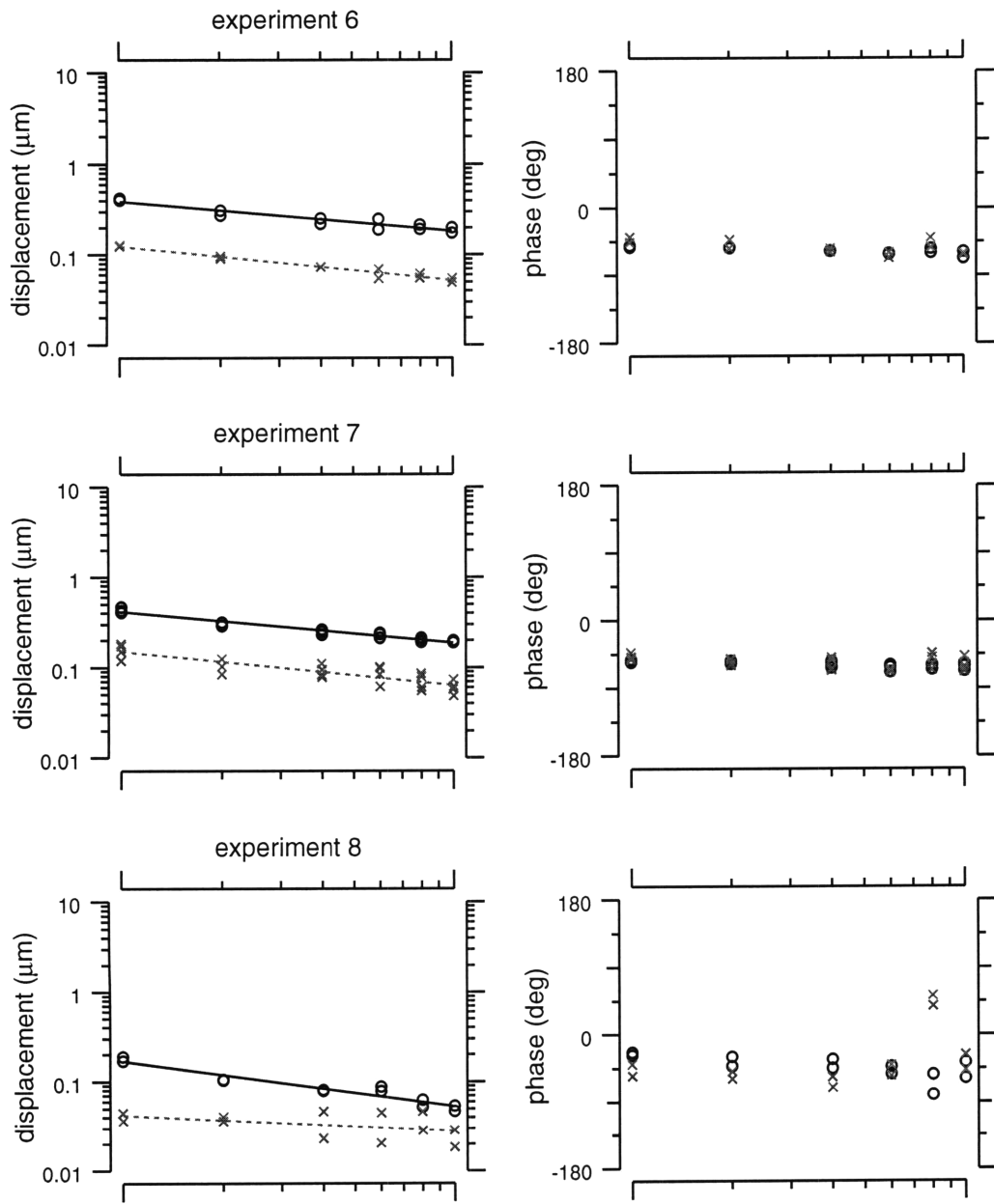


Figure B-1: The measured displacement of the magnetizable bead is plotted versus the frequency of the current stimulus for experiments #6, #7, and #8. In each experiment, a single current amplitude of 2.7 amps was applied to the magnets at frequencies of 10Hz, 20Hz, 40Hz, 60Hz, 80Hz, and 100Hz. The displacements associated with longitudinally applied forces are shown as black symbols and the solid line is a best fit through the data. Similarly, displacements associated with radial forces are shown as gray symbols with a dotted line fit through the data. Each symbol represents an independent displacement estimate based on 8 strobe illuminated images.

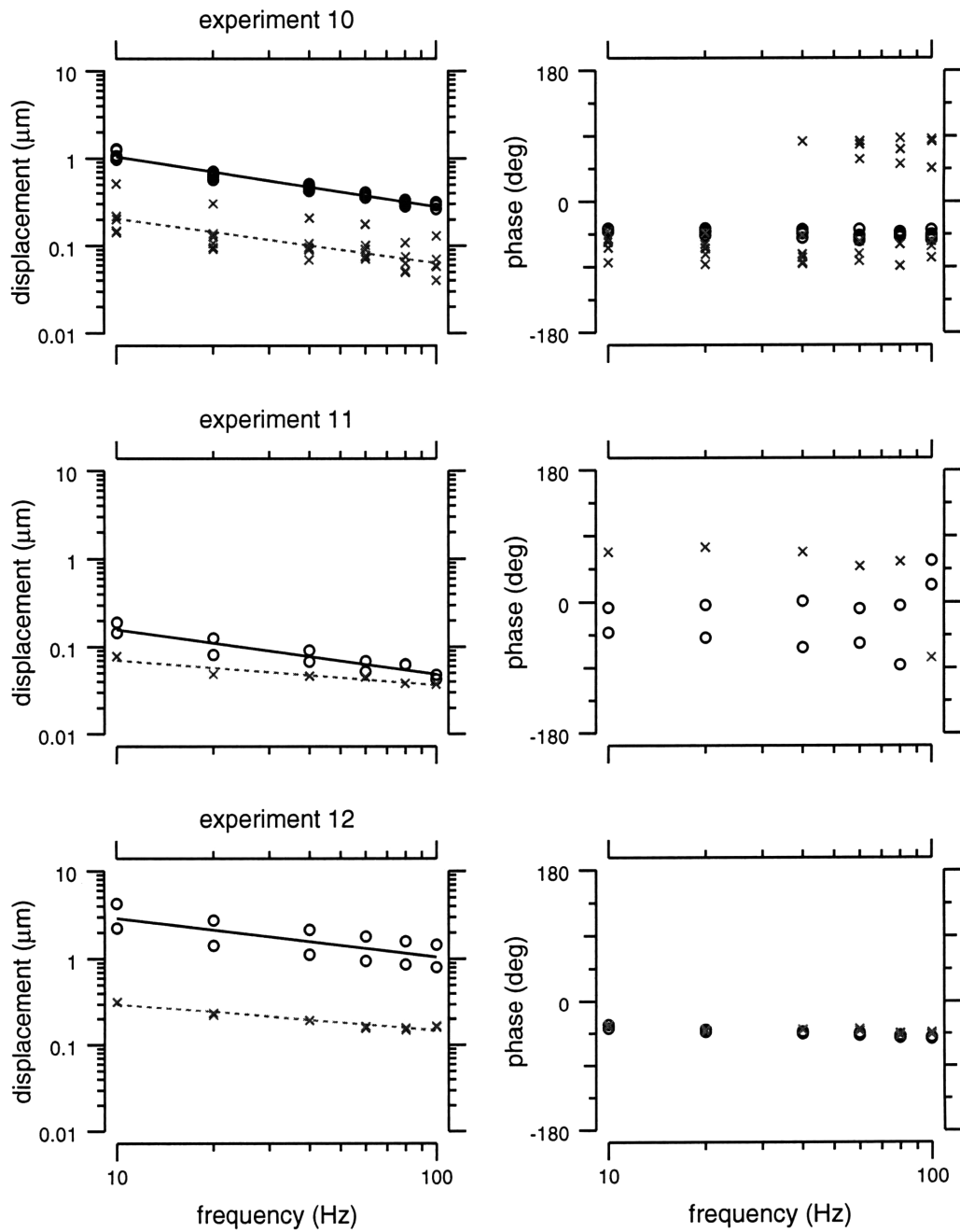


Figure B-2: The estimated phase of the magnetizable bead's displacement is plotted versus the frequency of the current stimulus for experiments #10, #11, and #12. Other aspects of this figure are described in Figure B-1.

Bibliography

- Allen, J. (1980). Cochlear micromechanics - a physical model of transduction, *Journal of the Acoustical Society of America* **68**(6): 1660–1670.
- Amblard, F., Yurke, B., Pargellis, A. and Leibler, S. (1996). A magnetic manipulator for studying local rheology and micromechanical properties of biological systems, *Review of Scientific Instruments* **67**: 818–827.
- Bekesy, G. v. (1953). Description of some mechanical properties of the organ of Corti., *Journal of the Acoustic Society of America* **25**: 770–785.
- Bekesy, G. v. (1960). *Experiments in hearing*, McGraw-Hill.
- Ciureanu, P. and Gavrilă, H. (eds) (1990). *Magnetic Heads for Digital Recording*, number 39 in *Studies in Electrical and Electronic Engineering*, Elsevier.
- Crick, F. and Hughes, A. (1950). The physical properties of cytoplasm: A study by means of the magnetic particle method, *Experimental Cell Research* **1**: 37–80.
- dallos, P. (1996). Overview: Cochlear neurobiology, in P. Dallos, A. Popper and R. Fay (eds), *The Cochlea*, Springer-Verlag.
- Dallos, P., Popper, A. and Fay, R. (eds) (1996). *The Cochlea*, Springer-Verlag.
- Davis, C. (1991). *Estimation of sub-micrometer translations of a rigid body using light microscopy*, Master's thesis, Massachusetts Institute of Technology.
- Davis, C. (1997). *Measuring Nanometer, Three-Dimensional Motions with Light Microscopy*, PhD thesis, Massachusetts Institute of Technology.

- Davis, H. (1958). A mechano-electrical theory of cochlear action, *Annals of Otolology, Rhinology, and Laryngology* **67**: 789–793.
- de Boer, E. (1996). Mechanics of the cochlea: Modeling efforts, in P. Dallos, A. Popper and R. Fay (eds), *The Cochlea*, Springer-Verlag.
- Ferry, J. (1970). *Viscoelastic Properties of Polymers*, John Wiley and Sons, Inc.
- Freeman, D., Cotanche, D., Ehsani, F. and Weiss, T. (1994). The osmotic response of the isolated tectorial membrane of the chick to isosmotic solutions: effect of Na^+ , K^+ , and Ca^{2+} , *Hearing Research* **79**: 197–215.
- Freeman, D. and Weiss, T. (1986). On the role of fluid inertia and viscosity in stereociliary tuft motion: Analysis of isolated bodies of regular geometry, in J. Allen, J. Hall, A. Hubbard, S. Neely and A. Tubis (eds), *Peripheral Auditory Mechanisms*, Springer-Verlag, pp. 147–154.
- Happel, J. and Brenner, H. (1973). *Low Reynolds number hydrodynamics*, Noordhoff International Publishing.
- Hasko, J. A. and Richardson, G. P. (1988). The ultrastructural organization and properties of the mouse tectorial membrane matrix, *Hearing Research* **35**: 21–38.
- Hayes, W. and Bodine, A. (1941). Flow-independent viscoelastic properties of articular cartilage matrix, *Journal of Biomechanics* **11**: 407–419.
- Hiramoto, Y. (1969). Mechanical properties of the protoplasm of the sea urchin egg: Unfertilized egg, *Experimental Cell Research* **56**: 201–208.
- Hudspeth, A. and Corey, D. (1978). Controlled bending of high-resistance glass microelectrodes, *American Journal of Physiology* **234**: C56–C57.
- James, S. and Marriott, C. (1982). A modified oscillating sphere magnetic microrheometer for use with biological secretions, *Journal of Physics E: Scientific Instruments* **15**: 179–181.

- Kempson, G., Muir, H., Pollard, C. and Tuke, M. (1973). The tensile properties of the cartilage of human femoral condyles related to the content of collagen and glycosaminoglycans, *Biochimica et Biophysica Acta* **297**: 456–472.
- Kimura, R. (1966). Hairs of the cochlear sensory cells and their attachment to the tectorial membrane, *Acta Otolaryngologica* **61**: 55–72.
- King, M. and Macklem, P. T. (1977). Rheological properties of microliter quantities of normal mucus, *Journal of Applied Physiology: Respirat. Environ. Exercise Physiol.* **42**: 797–802.
- Kronester-Frei, A. (1978). Ultrastructure of the different zones of the tectorial membrane, *Cell Tissue Research* **193**: 11–23.
- Lide, D. R. (ed.) (1997). *CRC Handbook of Chemistry and Physics, 77th edition*, CRC Press.
- Lighthill, S. J. (1991). Biomechanics of hearing sensitivity, *Journal of Vibration and Acoustics* **113**: 1–13.
- Lim, D. (1972). Fine morphology of the tectorial membrane, *Arch Otolaryng* **68**: 1660–1670.
- Lim, D. (1980). Cochlear anatomy related to cochlear micromechanics. A review, *Journal of the Acoustical Society of America* **67**(5): 1686–1695.
- Lure, A. (ed.) (1964). *3-D Problems of the Theory of Elasticity*, John Wiley and Sons.
- Lutz, R., Litt, M. and Chakrin, L. (1973). Physical-chemical factors in mucus rheology, in H. Gabelnick and M. Litt (eds), *Rheology of biological systems*, Thomas.
- Mammano, F. and Nobili, R. (1993). Biophysics of the cochlea: Linear approximation, *Journal of the Acoustical Society of America* **93**: 3320–3332.
- Patuzzi, R. (1996). Cochlear micromechanics and macromechanics, in P. Dallos, A. Popper and R. Fay (eds), *The Cochlea*, Springer-Verlag.

- Pickles, J. (1988). *An Introduction to the Physiology of Hearing*, Harcourt Brace Javonovich.
- Press, W., Flannery, B., Teukolsky, S. and Vetterling, W. (1988). *Numerical Recipes in C: The Art of Scientific Computing*, Cambridge University Press.
- Seifriz, W. (1924). An elastic value of protoplasm, with further observations on the viscosity of protoplasm, *British Journal of Experimental Biology* **2**: 1–11.
- Shah, D., Freeman, D. and Weiss, T. (1995). The osmotic response of the isolated, unfixed mouse tectorial membrane to isosmotic solutions, *Hearing Research* **87**: 187–207.
- Slepecky, N. (1996). Cochlear structure, in P. Dallos, A. Popper and R. Fay (eds), *The Cochlea*, Springer-Verlag.
- Steel, K. P. (1983a). Donnan equilibrium in the tectorial membrane, *Hearing Research* **12**: 265–272.
- Steel, K. P. (1983b). The tectorial membrane of mammals, *Hearing Research* **9**: 327–359.
- Thalmann, I. (1993). Collagen of accessory structures of organ of corti, *Connective Tissue Research* **29**: 191–201.
- Thalmann, I., Machiki, K., Calabro, A., Hascall, V. C. and Thalmann, R. (1987). Composition and supramolecular organization of the tectorial membrane, *Laryngoscope* **97**: 357–367.
- Thalmann, I., Thallinger, G., Comegys, T., Crouch, E., Barrett, N. and Thalmann, R. (1993). Uronic acid-containing glycosaminoglycans and keratan sulfate are present in the tectorial membrane of the inner ear: functional implications, *Archives of Biochemistry and Biophysics* **307**: 391–396.
- Timoshenko, S. and Goodier, J. (1970). *Theory of Elasticity*, McGraw-Hill.

- Tortonese, M. (1997). Cantilevers and tips for atomic force microscopy, *IEEE Engineering in Medicine and Biology* pp. 28–33.
- Tortonese, M. and Kirk, M. (1997). Characterization of application specific probes for SPMs, *SPIE* **3009**: 53–60.
- Tran-Son-Tay, R., Beaty, B., Acker, D. and Hochmuth, R. (1988). Magnetically driven, acoustically tracked, translating-ball rheometer for small, opaque samples, *Review of Scientific Instruments* **59**: 1399–1404.
- Tsuprun, V. and Santi, P. (1996). Crystalline arrays of proteoglycan and collagen in the tectorial membrane, *Matrix Biology* **15**: 31–38.
- Valberg, P. A. and Albertini, D. F. (1985). Cytoplasmic motions, rheology, and structure probed by a novel magnetic particle method, *Journal of Cell Biology* **101**: 130–140.
- Wang, N., Butler, J. P. and Ingber, D. E. (1993). Mechanotransduction across the cell surface and through the cytoskeleton, *Science* **260**: 1124–1126.
- Yih, C.-S. (1979). *Fluid Mechanics*, West River Press.
- Zahn, M. (1979). *Electromagnetic field theory: a problem solving approach*, John Wiley and Sons, Inc.
- Zhu, W., Iatridis, J., Hlibezuk, V., Ratcliffe, A. and Mow, V. (1996). Determination of collagen-proteoglycan interactions in vitro, *Journal of Biomechanics* **29**(6): 773–783.
- Zwislocki, J. and Cefaratti, L. (1988). Tectorial membrane II: Stiffness measurements in vivo, *Hearing Research* **42**: 211–227.
- Zwislocki, J. and Kletsky, K. (1979). Tectorial membrane: a possible effect on frequency analysis in the cochlea, *Science* **204**(11): 639–641.